Characteristics of Tungsten Silicide and its Application for Single X-ray Photon Detection

Dissertation
zur
Erlangung der naturwissenschaftlichen Doktorwürde
(Dr. sc. nat.)
vorgelegt der
Mathematisch-naturwissenschaftlichen Fakultät
der
Universität Zürich
von

Xiaofu Zhang

aus der
V. R. China

Promotionskommission
Prof. Dr. Andreas Schilling (Vorsitz und Leitung)

PD. Dr. Christof Aegerter

Dr. Qiang Wang

Zürich, 2018

Contents

Abstract

The first direct single infrared photon detection via superconducting electronic devices was realized by superconducting nanowire single photon detectors (SNSPDs) in 2001. Within nearly twenty years of development, the system detection efficiency of SNSPDs has reached as high as 93%. SNSPDs outperform other types of single photon detection technologies in terms of high detection efficiency, negligible dark count or false signal response, low timing jitter, and high count rate (CR), which render them the most suitable detectors for single photon counting experiments in the visible and near infrared range.

The detection mechanism of SNSPDs has become a hot topic already soon after its invention. The most widely considered detection mechanism is the hotspot scenario based on a bias current redistribution model. The absorbed photon within the nanowire creates a hotspot, which compels the bias current into the sidewalk around the hotspot. If the bias current is large enough, the current density in the sidewalks of the nanowire will exceed the critical current density, which in turn transfers the whole nanowire cross section into the normal state. As a result, the bias current is shunt into the readout circuit and a detection signal is created. A detailed analysis of the photon energy and energy conversion efficiency suggests that the hotspot size is much larger than that expected from the hard core model, in which a photon induced nonequilibrium area should be a belt instead of a spot. However, this model still fails to give a perfect description of the detection process. A more comprehensive model is based on vortex crossing, in which the vortex entry barrier is lowered by the photon induced hotspot. Among these different detection models, the photon induced hotspot or nonequilibrium area plays a dominating role, and the hotspot dynamics and its size represents one of the most important problems for understanding SNSPDs.

In order to give a quantitative description to the hotspot dynamics, we interpreted this process into a two-stage, diffusion based quasiparticles multiplication model. Firstly, the hot electron which absorbs the incident photon thermalizes within a short time scale and a small hot quasiparticle core is created. Then these hot quasiparticles diffuse further away from the hard core and a much larger hotspot is formed. From this model, the hotspot is defined as the area

when the quasiparticle number reaches its maximum. Our model successfully describes the hotspot dynamics, and the determined hotspot size is quantitatively consistent with that from corresponding quantum detection tomography experiments. Our model particularly explains the much smaller hotspot size in NbN based SNSPDs as compared to other materials. From our definition of the hotspot size, we are also able to give a qualitative description of the temperature dependence and photon energy dependence of the detection efficiency.

Moreover, we measured the transport parameters for WSi materials, which are the most fascinating materials for SNSPD fabrication. Besides the smaller superconducting energy gap (the incident photon can create more quasiparticles), amorphous WSi superconductors have a much larger coherence length as compared with NbN, which makes WSi based SNSPDs more robust against the constrictions introduced by the nano-fabrication. Moreover, the larger magnetic penetration depth in WSi leads to a suppressed vortex entry barrier, which make the WSi based SNSPDs more sensitive to the low energy photons. Finally, the most striking characteristics of WSi is their long lifetime of quasiparticles, which results in a much larger hotspot.

Based on the understanding of WSi materials, we successfully introduced the WSi materials into the continuous single X-ray photon detection. Firstly, the amorphous nature of WSi makes it more robust against the high energy X-ray irradiation when compared with the semiconductor detectors and crystalline superconducting detectors. Secondly, the heavy tungsten element of WSi X-SNSPDs improves the absorption efficiency. Finally, the hotspot created by the X-ray photons must be much larger in WSi than NbN or TaN. The fabricated $W_{0.8}Si_{0.2}$ X-SNSPD has a critical temperature of 4.97 K, and it is able to be operated up to 4.8 K, just below the critical temperature. The detector starts to react to X-ray photons at relatively low bias currents, less than 1% of I_c at T = 1.8 K, and it shows a saturated count rate as a function of bias current at all operating temperatures, indicating that the optimum internal quantum efficiency can always be reached. The dark counts of WSi X-SNSPD are negligible at the highest investigated bias current (99% of I_c) and operating temperature (4.8 K). These remarkable performance renders WSi an excellent suitable material for X-SNSPD applications.

Finally, we also performed magnetic field driven superconductor to insulator transition (SIT) experiments on the $W_{0.75}Si_{0.25}$ bridges. Transport measurements reveal the localization of Cooper pairs at a first critical field B_c^1 (Bose-insulator), with a product of the correlation length and dynamical exponents $z\nu \sim 4/3$ near the quantum critical point (QCP). Beyond B_c^1

superconducting fluctuations still persist. Above a second critical field $B_c^2 > B_c^1$, the Cooper pairs are destroyed and the film becomes a Fermi-insulator. The different phases all merge at a tricritical point with $z\nu = 2/3$. Our results suggest sequential phase transitions (superconductor - Bose insulator - Fermi insulator) in the zero-temperature limit, which differs from the conventional scenario involving a single quantum critical point.

Zusammenfassung

Die erste direkte Einzel-Infrarot-Photonen-Detektion über supraleitende elektronische Bauelemente wurde 2001 durch supraleitende Nanodraht-Einzelphotonen-Detektoren (SNSPDs) realisiert. Innerhalb von etwa 20 Jahren der Entwicklung hat die System-Detektionseffizienz der SNSPDs Werte bis zu 93% erreicht. SNSPDs übertreffen andere Typen von Einzelphotonen-Detektor-Technologien durch hohe Detektionseffizienz, vernachlässigbare Dunkelzählraten oder falsche Signal-Antworten, kurzer Zeit-Jitter und hohe Zählrate, die sie zu den passendsten Detektoren für Einzelphotonen-Zählungs-Experimenten im Sichtbaren und nahinfraroten Bereich machen.

Der Detektionsmechanismus der SNSPDs wurde zu einem heissen Thema nach seiner Entdeckung. Der am meisten betrachtete Detektionsmechanismus ist das Heisspunkt-(“hotspot”) Szenario basierend auf einem Basisstrom-Umverteilungsmodell. Das absorbierte Photon erzeugt innerhalb des Nanodrahtes einen “hotspot”, welcher den Basisstrom an die Seitenwände um den “hotspot” herum zwingt. Falls der Basisstrom gross genug ist, übersteigt die Stromdichte an den Seitenwänden des Nanodrahtes die kritische Stromdichte, welche nun den ganzen Nanodrahtquerschnitt in den Normalzustand überführt. Als Ergebnis wird der Basisstrom in die Auslse-Elektronik abgeleitet und ein Detektionssignal wird erzeugt. Eine detaillierte Analyse der Photonenenergie und der Energiekonversionseffizienz weisen darauf hin, dass die Grösse des “hotspot” viel ausgedehnter ist als durch das Hartkernmodell erwartet wird, in welchem das photoneninduzierte Ungleichgewichtgebiet ein Band ist anstatt eines Punktes. Allerdings scheitert dieses Modell daran, eine perfekte Beschreibung des Detektionsprozesses zu geben. Ein umfassenderes Modell basiert auf Vortexkreuzung, in welchem die Vortexeintrittsbariere durch den photoinduzierten “hotspot” gesenkt wird. Innerhalb dieser verschiedenen Detektionsmodelle spielt der photoinduzierte “hotspot” oder das Nichtgleichgewichtsgebiet eine dominante Rolle, und die “hotspot” dynamik und -grösse stellen eines der wichtigsten Probleme für das Verständnis der SNSPSs dar.

Um eine quantitative Beschreibung dieser Dynamik zu geben, interpretieren wir diesen Prozess als zweistufiges, diffusionsbasiertes Quasiteilchenmultiplikationsmodell. Zuerst thermalisert das heisse Elektron, welches das eintreffende Photon absorbiert, innerhalb einer kurzen Zeitskala, und ein kleiner heisser Quasiteilchenkern wird erzeugt. Diese heissen

Quasiteilchen diffundieren dann weiter vom harten Kern weg und ein viel grösserer “hotspot” entsteht. In diesem Modell wird der “hotspot” definiert als Gebiet in der die Quasiteilchenzahl ihr Maximum erreicht. Unser Modell beschreibt erfolgreich die “hotspot” dynamik, und die erhaltene Grösse des “hotspot” ist quantitativ konsistent mit der von entsprechenden Quantendetektionstomographie-Experimenten. Unser Modell beschreibt insbesondere die viel kleinere Ausdehnung in NbN-basierten SNSPDs verglichen mit anderen Materialien. Durch unsere Definition der “hotspot” sind wir auch in der Lage, eine qualitative Beschreibung der Temperaturabhängigkeit und Photonenenergie-Abhängigkeit der Detektionseffizienz zu geben.

Ferner haben wir die Transport-Parameter für WSi-Materialien gemessen, welche die faszinierendsten Materialien für die SNSPD-Herstellung sind. Neben der kleineren supraleitenden Energielücke (das eintreffende Photon kann mehr Quasiteilchen kreiren), haben WSi-Supraleiter eine viel grössere Kohärenzlänge verglichen mit NbN, welches WSi robuster macht gegenüber den Einschränkungen, die durch die Nanofabrikation eingeführt werden. Des Weiteren führt die grosse magnetische Eindringtiefe in WSi zu einer unterdrückten Vortex-Eintrittsbariere, welche die WSi-basierten SNSPDs sensitiver machen für Photonen niederer Energien. Schlussendlich ist die bestechendste Charakteristik von WSi dessen lange Quasiteilchen-Lebenszeit, welche in viel grösseren “hotspot” resultiert.

Basierend auf dem Verständnis der WSi-Materialien führten wir erfolgreich die WSi-Materialien in die kontinuierliche Einzel-Röntgenphotonen-Detektion ein. Erstens macht die amorphe Natur von WSi es robuster gegen die Hochenergie-Röntgenstrahlen verglichen mit Halbleiterdetektoren und kristallinen supraleitenden Detektoren. Zweitens erhöht das schwere Element Wolfram der WSi-Röntgen-SNSPDs die Absorptionseffizienz. Schlussendlich wird der “hotspot”, welcher durch die Röntgenphotonen erzeugt wird, in WSi viel grösser als in NbN oder TaN. Der fabrizierte $W_{0.8}Si_{0.2}$ Röntgen-SNSPD hat eine kritische Temperatur von 4.97 K und kann bei bis zu 4.8 K betrieben werden, knapp unterhalb der kritischen Temperatur. Der Detektor beginnt bei relativ niedrigen Basisströmen auf Röntgenphotonen zu reagieren, weniger als 1% von I_c bei T = 1.8 K, und zeigt eine gesättigte Zählrate als Funktion des Basisstroms bei allen Betriebstemperaturen, was zeigt, das die optimale interne Quanteneffizienz immer erreicht werden kann. Die Dunkelzählraten von WSi-Röntgen-SNSPDs sind vernachlässigbar beiden höchsten untersuchten Basisströmen (99% von I_c) und Betriebstemperaturen (4.8 K). Diese bemerkenswerte Leistung macht WSi ein exzellent geeignetes Material für Röntgen-SNSPDs.

Schlussendlich führten wir experimente an magnetfeldgetriebene Supraleiter-Isolator-Übergängen an $W_{0.75}Si_{0.25}$ Brücken durch. Transportmessungen offenbaren die Lokalisierung von Cooperpaaren bei einem ersten kritischen Feld B_c^1 (Bose-Isolator), mit einem Produkt der Korrelationslänge und des dynamischen Exponenten $z\nu = 4/3$ nahe des quantenkritischen Punktes. Oberhalb von B_c^1 bestehen immer noch supraleitende Fluktuationen. Oberhalb eines zweiten kritischen Feldes $B_c^2 > B_c^1$ werden die Cooperpaare zerstört und der Film wird zu einem Fermi-Isolator. Die unterschiedlichen Phasen vereinen sich an einem trikritischen Punkt mit $z\nu = 2/3$. Unsere Resultate legen sequenzielle Phasenübergänge (Supraleiter – Bose-Isolator – Fermi-Isolator) im Null-Temperatur-Bereich nahe, was sich vom konventionellen Szenario unterscheidet, welches einen einzelnen quantenkritischen Punkt involviert.

1 Background of SNSPDs

A single photon is an elementary particle, namely the quantum of the electromagnetic energy in electromagnetic radiation [1]. The energy of photons $E = hc/\lambda$ in the visible and near infrared range is around 1 eV, where h is Planck constant, c is the the speed of light in vacuum and λ is the wavelength of the radiation. In order to detect such a low energy quantum, a single-photon detector (SPD) must be an extremely sensitive device capable of sensing the quantized electromagnetic radiation [2]. Conventional SPDs are based on photomultiplier tubes or avalanche photodiodes, which have been used in many photon number sensitive applications [3-15]. In recent years, due to the optical quantum information applications such as quantum cryptography and quantum computing, the interest in photon number-resolving infrared single-photon detectors (SPD) has increased dramatically. These applications have severe requirements to the applied detectors: (a) the SPDs should have a broadband response; (b) the dead time or the recovery time of the SPDs should be low enough, which ensures a high count rate; (c) the dark counts, dark noise or false detection events of SPDs without photon illumination should be negligible; (d) the SPDs should have high time accuracy, namely low time jitter; (e) the SPDs should have high quantum detection efficiency. These rigorous demands have led to considerable improvements in conventional single-photon detectors, but the traditional photon-number-resolving detectors still cannot fulfil all these the demands simultaneously [2].

In 2001, a new type of single photon detector was proposed by Gol’tsman *et al.* [16], which is called superconducting nanowire single photon detector (SNSPD), also referred to superconducting single photon detector (SSPD). SNSPDs offer single-photon sensitivity from visible to mid-infrared wavelengths, low dark counts, short recovery times, low time jitter, and high detection efficiency up tp 93% [17-25], rendering them the most promising single photon detector for quantum information applications [26-32].

1.1 SNSPDs for visible and near infrared photons

1.1.1 Development of SNSPDs for visible and near infrared photons

The first SNSPD was designed and fabricated by Gol’tsman *et al.*, which was based on nominally 0.2 μm wide and 1 mm long microbridges patterned from ultrathin ~ 5 nm thick NbN films deposited on a sapphire substrate [33]. The device was biased just below its experimental critical current I_c. An incident photon induces a supercurrent-assisted hotspot formation leading to a temporary switch from the superconducting state to the hotspot resistive state. As a result, an output voltage is generated along the 50 Ω load line. The single photon resolution was demonstrated by observing a linear dependence of photo detection probability on the number of incident photons. The intrinsic quantum efficiency (QE, the probability of detecting an optical pulse containing an average of one photon incident on the device) of the used NbN microbridge was estimated to be 20% at a bias current of $0.92I_c$ for 0.81 μm photons.

This NbN microbridge, however, had a limited sensitive area. Later, the first meander type SNSPD was designed for timing measurements on complementary metal–oxide–semiconductor integrated circuits by detecting the infrared light emission from switching transistors [17]. As it is shown in Fig. 1.1, a meander type SNSPD consists of a long, 10 nm thick, 200 nm wide NbN serpentine stripe deposited onto a sapphire substrate, which occupies a 10 μm × 10 μm region to increase its active area. Photons are coupled to the detector with a 62.5 μm core-diameter, graded-index, multimode optical fibre. The QE of the 10 μm × 10 μm detectors is typically 0.01%–0.2% with a bias current of $0.98I_c$ to $0.99I_c$. The intrinsic QE of this detector is limited by constrictions in the NbN meander stripes. Though the QE of this detector was limited, this detector had lower jitter (< 40 ps) than any other photon counting detector and low dark count rates (< 50 counts/s) in 2001.

After several years of development, the understanding and operation of SNSPDs have has been greatly improved [34-48]. The detection efficiency, however, has still been limited below 10 percent [45-48]. This is due to the low absorption efficiency (the probability of an incident photon being absorbed by the superconducting material). In order to enhance the photon absorption, researchers considered to embed the SNSPDs within an optical cavity [49, 50]. In Fig. 1.2, we show two similar designs integrated with an optical cavity and anti-reflection coating (ARC) to reduce loss of photons from reflection and transmission by two different research groups.

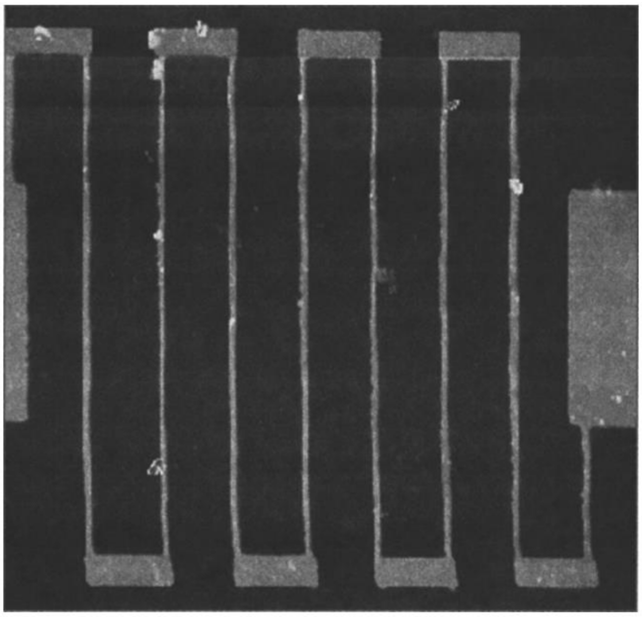

Fig. 1.1: The meander type 15 µm × 15 µm AFM image of a superconducting single-photon counting detector [17].

With the detector shown in Fig. 1.2(a), the device detection efficiency (DDE) for 1550 nm photons have been increased from ~ 20% to ~ 60% after the integration of an optical cavity and ARC [49]. The detector QE of the device shown in Fig. 1.2(b) at the resonant wavelength increased by factor of 3 to 4 as compared to that of a detector without microcavity. After the fibre coupling (with an estimated photon coupling efficiency of 30%), the whole detection system finally showed a system detection efficiency (SDE) of ~1% [50].

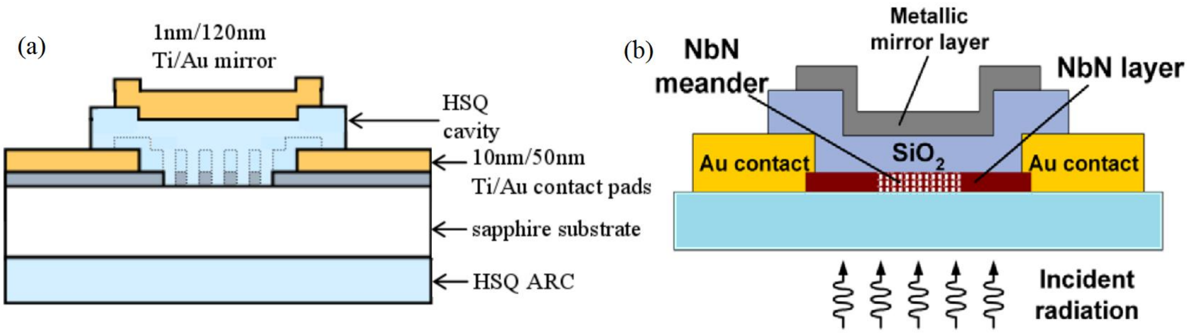

Fig. 1.2: Schematic structure of two similar optical resonant cavities integrated with the SNSPD for enhancing the photon absorption probability. In (a), the negative resist hydrogen silsesquioxane (HSQ) is used for electron beam lithography [49], while poly-methyl methacrylate (PMMA) is adopted in (b) [50].

Besides the improvement of the photon absorption probability, devices with the same geometry still showed huge variations of their detection performance. As it is shown in Fig. 1.3(a), Andrew J. Kerman *et al.* measured more than 100 devices with nominally identical device geometry [51]. From the DDE vs I_b/I_c, the best device began to respond to the incident photons at relatively low current. Moreover, the DDE of the best device was even two orders of magnitude higher than that of the worst devices at the same bias current. Through both electrical and optical measurements, they inferred that these DDE variations arose from "constrictions", i.e., localized regions of the nanowires where the effective cross-sectional area for the superconducting current is reduced. In the remaining uniform nanowire area, the bias current density j_{b} is much lower than the local superconducting depairing current j_c^d, and the DDE is therefore suppressed since it is strongly dependent on j_b/j_c^d. As a result, for a constricted SNSPD, only the constricted areas are active to the incident photons, which in turn limits the DDE to a relatively low value.

This conclusion was examined by a submicrometer photoresponse mapping experiment [52]. Robert H. Hadfield *et al*. used a confocal microscope configuration and solid immersion lens to achieve a light spot size of 320 nm at 470 nm wavelength, which is significantly smaller than the device area (10 μm × 10 μm). The mapped photon response for a good SNSPD and a constricted SNSPD are shown in Fig. 1.4. The device with higher detection efficiency showed a uniform response, while the constricted device was limited by a single defect or constriction [52].

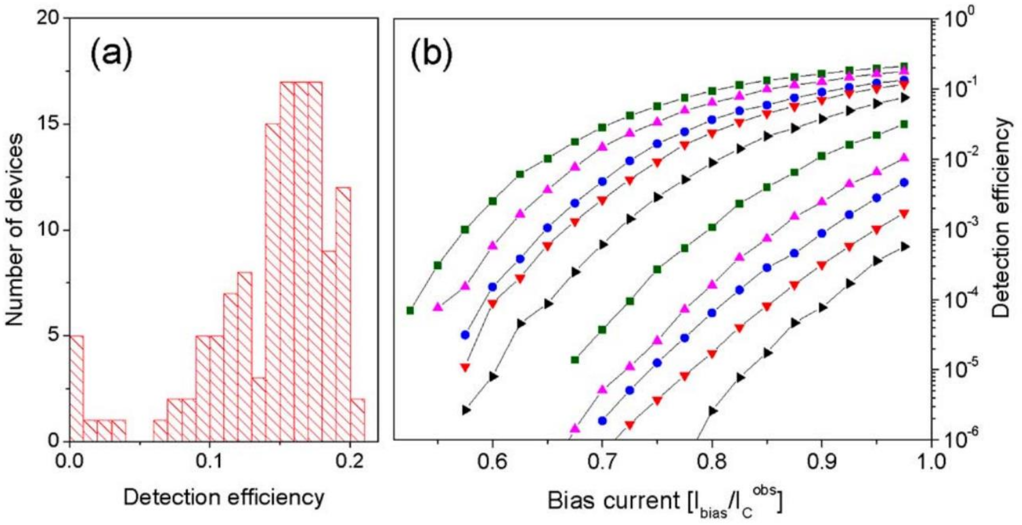

Fig. 1.3: Statistics in SNSPDs detection efficiency [51]. (a) Histogram of the DDEs measured for 132 devices. (b) Measurements of DDE vs normalized bias current for selected devices.

Though different materials and optical cavity structures (the role of materials will be discussed in next subsection) have been adopted in SNSPDs design and fabrication, the SDE of SNSPDs has not been significantly improved in the first 10 years after the invention of SNSPDs [53-103]. A significant improvement of SDE for SNSPDs was not realized until the introduction of tungsten silicide (WSi) into the SNSPDs fabrication [19].

So far the highest SDE at 1550 nm was achieved in an amorphous WSi based SNSPDs [19]. Since the amorphous WSi is homogeneously disordered, WSi superconducting nanowires are more robust with respect to constrictions, local uniformities, and film thickness variations than NbN nanowires, which in turn allows for the fabrication of larger-area devices. Moreover, WSi can be deposited on a variety of substrates, such as glass or photon resist, which lowers the degree of freedom in optimizing the optical coupling and the absorption of the detectors [104]. Finally, WSi SNSPDs based on nanowires as wide as 150 nm have shown saturated SDE versus I_b curves (the corresponding bias current I_s is defined the current beyond which the SDE or DDE no longer increase with I_b; the region $I_s < I_b < I_c$ is therefore called as saturation region) in the near-infrared, because the size of the photon-induced perturbation of the superconducting state (namely the hotspot) is larger in WSi than in NbN [19, 76].

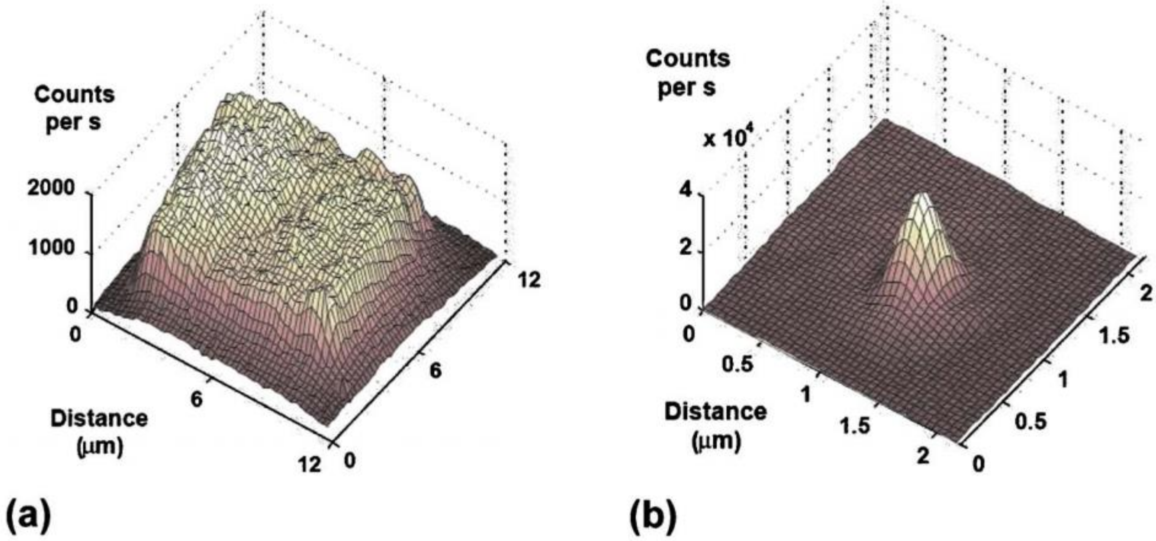

Fig. 1.4: Photoresponse signatures of nanowire SNSPDs for (a) high detection efficiency device and (b) low detection efficiency device [52].

1.1.2 Materials for SNSPDs fabrication

1.1.2.1 Niobium nitride (NbN)

During the early stage of SNSPDs research, NbN was the main choice of materials for the SNSPDs fabrication due to the feasibility of depositing very thin films (4 nm thick) required for SNSPDs. However, the NbN films in the range of several nanometers thickness are always in a granular state. A small granule is in the superconducting state only when the average spacing between the energy levels of electrons $\delta\varepsilon$ inside the granules is less than the superconducting energy gap Δ,

$$\delta\varepsilon = (g_0 b^3)^{-1} < \Delta. \tag{1.1}$$

Here g_0 is the density of states at the Fermi level and b^3 is the average volume of the granules. The minimum size of granules is therefore specified through $\delta\varepsilon \sim \Delta$. Thus the critical size of an isolated granule can be written as

$$b_c = (g_0 \Delta)^{-1/3}. \tag{1.2}$$

When the size of a granule b is smaller than b_c, it cannot be in the superconducting state by itself. For granular superconductors, with sufficiently large granule size, the transition to superconducting state within the granules occurs at the same temperature as that in the bulk materials, but the behavior of the entire thin film as a whole depends on the interaction between the granules [105]. The current flowing through granular films corresponds to the tunnelling current between two superconducting granules, consisting of two components: the superconducting Josephson current of Cooper pairs, and a single particle dissipative current. The Josephson current can be suppressed for various reasons; in particular, it is suppressed by fluctuations [105].

As a result, good superconducting properties of NbN films are achieved only in crystalline films [106], which are affected by crystal defects, limiting (i) the fabrication yield of large-area devices, (ii) the choice of substrates for fabrication and (iii) the design parameters of optical structures that can enhance absorption in the nanowires. Furthermore, although the 30- and 20-nm-wide NbN nanowires have demonstrated a saturated detection efficiency at 1550 nm, the fabrication of uniform NbN SNSPDs with a large area based on such narrow nanowires remains challenging [19].

In order to achieve homogeneous NbN thin films with good quality, researchers have tried to deposit NbN on various substrates. Commonly, nanometers thick NbN is deposited on sapphire substrates above 750 ℃ by reactive magnetron sputtering [45, 49]. Great effort has been devoted to the film growth, aiming at improving their critical temperature and critical current density, while keeping the film thickness around 5 nm. With respect to the film growth, MgO and R-plane sapphire are usually considered as the most suitable substrates since the lattice mismatch with NbN is small (a_{MgO} = 4.212 Å, a_{NbN} ~ 4.39 – 4.46 Å, a_{sapphire} = 4.763 Å). In order to improve the film quality for the SNSPDs fabrication, Lamaestre *et al.* deposited NbN on different sapphire orientations. They found that the growth on M-plane sapphire at 600℃ showed the highest T_c of the films. The uniform 4.4 nm thick NbN film (indicated by X-ray reflectivity) showed a T_c as high as 13.3 K and a T_c of 7.8 K for 2.6 nm thick films [107]. Such high depositing temperatures, however, are not compatible with the fabrication of detectors on substrates that enables integration with optical elements such as waveguides, cavities or Bragg reflectors.

As an alternative to sapphire substrates, single-crystalline MgO substrates have the same cubic lattice structure and a very similar lattice constant as NbN, which allows for epitaxial growth from the initial layer and excellent superconductivity when compared to non-epitaxial NbN thin films on other substrates. Miki *et al.* tried to deposit and fabricate detectors on single-crystalline MgO substrates, and measurements of the kinetic inductance versus bias current indicated that the constriction density of SNSPDs was low [108, 109]. The QE of these devices, however, still remained at relatively low values. Later, Marsili *et al.* also deposited NbN on MgO at 400℃ and a QE of 20% for 1300 nm photons was achieved at 4.2 K [110, 111].

In order to make a good optical and electrical coupling with semiconductor devices, SNSPDs need to be fabricated on semiconductor materials, for instance, on GaAs. However, due to As outgassing, the GaAs substrates are not suitable for high temperature deposition [112]. During the deposition of NbN on GaAs distributed Bragg reflectors, the substrate temperatures were usually kept at 350 - 400℃, and a good detection performance was realized [74, 113-115]. Finally, besides the substrates mentioned above, lithium niobate and silicon substrate with a TiN buffer layer are also good substrate candidates for NbN based SNSPDs [116, 117].

1.1.2.2 Niobium titanium nitride (NbTiN)

The conditions for deposition of NbN and the substrate materials were limiting a large area NbN device fabrication. Compared with NbN material, the introduction of Ti into the NbN system can lower the energy for crystallization, and the NbTiN can be deposited at relatively low substrate temperature. In order to enable an easy integration in advanced electronic circuits, Dorenbos *et al.* fabricated NbTiN SNSPDs on Si, which showed a bulk T_c of 15 K, slightly lower than the bulk NbN with good quality, ~ 17 K. They found that SNSPDs made of NbTiN showed a reduced dark count rate by a factor of 10 as compared to identical NbN detectors, and matched the quantum efficiency of NbN detectors, leading to an improved signal-to-noise ratio [118]. Moreover, high quality NbTiN films have also been deposited by reactive dc magnetron sputtering at room temperature on a Si substrate with a 225 nm SiO_2 layer [119], with a resulting DE of 23.2% and 1 kHz dark count rate at 1310 nm [70].

Besides Si substrates, NbTiN can also be easily deposited on MgO. When compared with NbN, epitaxial NbTiN thin films on MgO substrates have better superconducting properties and a more favorable crystal structure as compared to epitaxial NbN thin films since the lattice mismatch of NbTiN on MgO substrates is smaller than that of NbN (with the same depositing conditions, $a_{\mathrm{NbN}} \sim 4.5$ Å, $a_{\mathrm{NbTiN}} \sim 4.4$ Å). Miki *et al.* successfully deposited 3.5-nm-thick $Nb_{0.8}Ti_{0.2}N$ films with comparable T_c to NbN, and the resistivity of NbTiN at 20 K was lower than NbN thin films. It is interesting to note that NbTiN based SNSPDs have a 25% lower kinetic inductance than NbN-SNSPDs, which indicates faster operation of NbTiN SNSPDs [120].

1.1.2.3 Amorphous superconductors

Amorphous superconductors are perfectly suitable for the fabrication of on-chip superconducting devices. The degradation of fabricated superconducting nanoscale devices is much less pronounced than that based on crystalline materials, and the amorphous nature makes the film robust down to a thickness of 1 nm [121, 122].

In 2011, Baek *et al.* were the first to utilize amorphous WSi as the absorbing medium instead of NbN or NbTiN for the SNSPDs fabrication. The bulk WSi films have a T_c of 5 K, but it reduces to around 4 K in 4 – 5 nm thick thin films. This material is able to overcome the limitations of the prevalent detectors based on NbN and lead to more practical single-photon detectors with high efficiency, low noise, and high count rates [76]. A uniform detector with a practical sensitive area as large as 16 µm × 16 µm was prepared. A significant improvement of WSi SNSPDs was that it showed a broad saturated DDE with bias current and over a wide wavelength range of 1280 - 1650 nm [76]. Afterwards, by embedding the WSi detector into an optical cavity, the highest ever reported SDE of 93% was observed in WSi [19], as it is shown in Fig. 1.5.

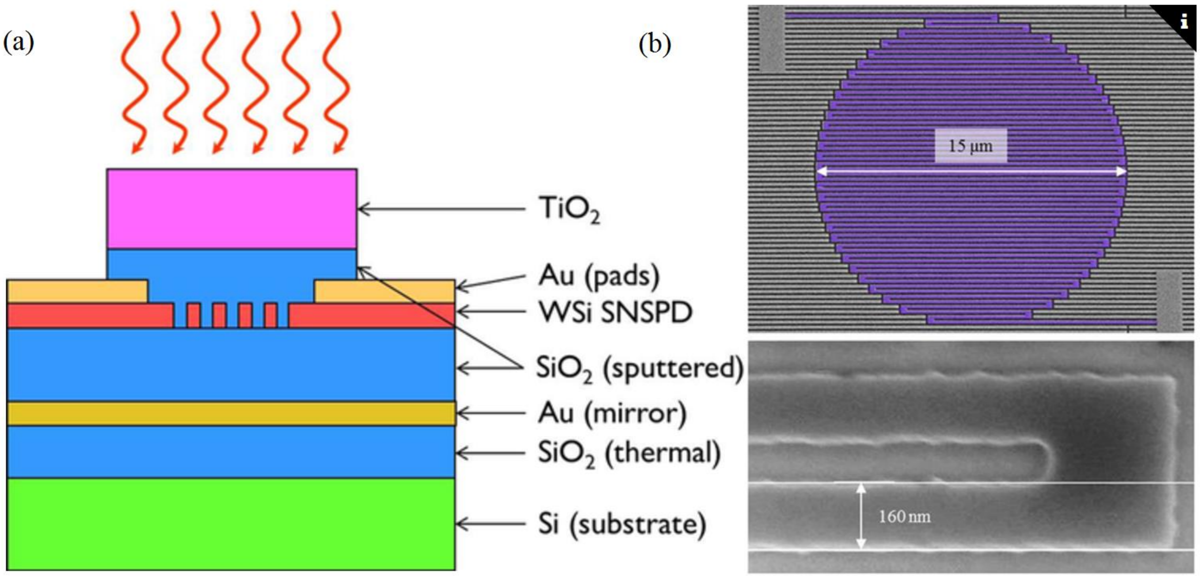

Fig 1.5: The optical cavity structure (a) and the SEM picture (b) of the WSi meander (top) and a single nanowire (bottom) adopted in Ref. [19]

Besides the high detection efficiency achieved with WSi due to its amorphous nature, WSi can even be deposited on photon resist. Verma *et al.* demonstrated vertically stacked two-layer WSi SNSPDs, which were electrically connected in parallel to form a three-dimensional superconducting nanowire avalanche photodetector (SNAP) [82]. This SNAP nanowire architecture in three-dimensions represents a significant advancement in single-photon detector technology. The optical stacking and using a high-fill-factor nanowire meander allowed for an SDE approaching 100%. Meanwhile, the intrinsically polarized optical response for SNSPDs could also be eliminated [82].

Though an ultrahigh SDE can be prepared with WSi SNSPDs, the corresponding operating temperature is still relatively low. The best detection performance of WSi SNSPDs has been measured at T = 120 mK. Verma *et al.* realized a $W_{0.8}Si_{0.2}$ nanowire meander with a width of 130 nm and a pitch of 260 nm, which is able to be operated at 2.5 K with an SDE as high as 78% for 1310 nm photons by modifying the tungsten stoichiometry [123].

The amorphous WSi is at present one of the most promising materials for the SNSPDs fabrication. The low operating temperature, however, is limiting their applications in many cases. Other amorphous superconductors have also been adopted for the SNSPDs fabrications. Verma *et al.* used $Mo_{0.75}Ge_{0.25}$ for SNSPD design and fabrication, which has a slight higher bulk T_c of 7.36 K than WSi. This SNSPD based on $Mo_{0.75}Ge_{0.25}$, however, shows a saturation of the internal detection efficiency only at temperatures below 1 K, with system dark count rates ~ 500 Hz, which is inferior to that of WSi based detectors [124]. Alternatively, MoSi with bulk T_c of 7.5 K was introduced into the SNSPDs fabrication. The first MoSi device was fabricated by Korneeva *et al.*, which showed a DE of 18% for the unoptimized detector. The DE of this MoSi system, however, did not show any saturated behaviour with the bias current [135]. Recently, an SNSPD based on MoSi with T_c of 5 K was realized, and a clear saturation behaviour was reported but the SDE is unknown [126].

1.1.2.4 Other low temperature superconductors

Soon after the successful application of NbN and NbTiN for SNSPDs, researchers also attempted to fabricate detectors based on pure Nb. Annunziata *et al.* built SNSPDs based on Nb with different thicknesses, and a comparison between Nb and NbN was made. Though Nb has a smaller sheet resistance, it is more susceptible to thermal latching than NbN [127].

Intuitively, an incident photon breaks more Cooper pairs and thus can create a larger hotspot , in materials with a smaller Δ, which in turn favors a higher detection efficiency of low-energy photons. Based on this idea, materials with lower T_c ($\Delta \propto k_{\mathrm{B}}T_c$) have been used for the SNSPDs fabrication. When compared with NbN and NbTiN, TaN has a lower T_c with a smaller energy gap and a lower density of states at the Fermi level [87]. Though the sensitivity to low energy photons is improved in TaN, the SDE still remains low. Meanwhile, NbSi with an even smaller T_c of 2 K and Δ was adopted for the SNSPDs fabrication, resulting an increased sensitivity for infrared wavelengths, but still with a moderate SDE [77].

1.1.2.5 Magnesium diboride (MgB_2)

Up to now, the state-of-the-art SNSPDs are based on low-critical-temperature superconductors so that the detectors need to be operated at low temperatures (typically below 4 K) for optimal performance. In laboratory research, the performance of SNSPDs has been measured at temperatures as low as 16 mK. However, in some cases, the operating temperature is limited, for instance, for optical communication applications in the on-orbit satellites. In such cases, an SNSPD with a relatively high transition temperature would be needed.

Monticone *et al.* fabricated MgB_2 meander nanowires by Electron Beam Lithography (EBL) with a wire width ranging from 250 nm to 500 nm and a T_c of 34 K. Critical current measurements showed that the superconducting properties of narrow nanowires were not affected by the nano fabrication process [128]. Shibata *et al.* measured the optical response of a 10 nm thick, 300 nm wide and 10 µm long single MgB_2 wire fabricated by EBL [129]. Afterwards, a 10 nm thick, 300 nm wide and 8 µm MgB_2 single nanowire based on a lift-off like technique was tested [130, 131]. The detector was able to be triggered by 1550 nm photons and a repetition rate of 100 MHz has been observed at high photon flux, which indicated that the detector worked at multiphoton detection regime [130, 131]. In 2015, Marsili *et al.* tested the optical response of a MgB_2 meander nanowire with T_c of 33 K. This MgB_2 SNSPD showed three-photon response at 4 K and a sub-ns relaxation time without latching [132]. However, SNSPDs based on MgB_2 are still far from practical applications.

1.2 Superconducting nanowire single X-ray photon detectors

Ultrafast single photon sensitive X-ray detectors have a potential for important applications in many areas. Using photon-counting detectors (PCDs), the image quality of the medical X-ray computed tomography (CT) with a low X-ray dose can be significantly improved [133, 134]. Such applications can even be extended to single molecular, virus, or cell CT and X-ray imaging [135]. The currently used energy integrating detectors (EIDs) in CT scanners and X-ray systems, however, have certain limits with regard to this technology. The EIDs measure the energy integrated signals of X-ray photons [133, 136], and they are affected by the electronic noise and Swank noise [137]. As a result, the weight of low energy photons is decreased, which in turn leads to an increase of noise and a decrease of contrast.[1] Moreover, the performance of PCDs based on semiconductor technology is not impeccable as the respective count rate is limited [133, 136, 138, 139]. These detectors have a typical dead time of several hundred nanoseconds, which limits the maximum count rate per pixel to a few megahertz. Meanwhile, the pixel size of these detectors is of the order of several hundred micrometers, which results in a maximum counts-per-second-per-square-millimeters (CPSPSM) of 10^6 cps [133]. The required count rate for a clinical X-ray CT scanner, however, may be as high as 10^9 cps [138]. Apart from the medical applications, ultrafast single X-ray photon detectors can also be used in synchrotron X-ray sources, free-electron lasers, and astronomy. Synchrotron radiation, for example, has provided the possibility to perform X-ray experiments at very short time scales, and the use of time resolving detectors is therefore essential [140-142]. The currently used Fast-Readout Low-Noise (FReLoN) detectors, however, have relatively large time jitter (more than ten nanoseconds) [142, 143]. Therefore, the highest possible time resolution in these experiments is limited.

There are several types of X-ray detectors with single photon sensitivity. If we categorize the detectors by the applied materials, single X-ray photon detectors can be divided into two types, namely the semiconductor based and the superconductor based X-ray detectors.

1.2.1 Semiconducting X-ray photon counting detectors

Semiconductor based X-ray detectors with a thickness on the millimetre level (1-3 mm) are chosen to effectively absorb X-ray photons in the energy range from 20 keV to 140 keV [133]. Alternative materials include cadmium telluride (CdTe) [144], cadmium zinc telluride (CZT) [145], silicon (Si) [146,147], mercury iodide (HgI_2) [148, 149] and gallium arsenide (GaAs)

[150, 151]. These detectors always have a *p-i-n* structure or a metal-semiconductor diode with a Schottky diode structure, and they commonly work in an avalanche multiplication mode. The pixel size ranges from several tens of micrometers to the millimetre scale. However, one of the main limitations of this type of detectors is that they cannot reach high enough counting rates as required by applications [152-168]. Except for the direct photon detection by semiconductor diodes, indirect X-ray detectors use a two-step process to detect X-ray photons. X-ray photons are firstly absorbed by a scintillator and subsequently converted into visible photons; then the signal is created by visible photon detection techniques [169, 170]. These detectors, however, have high dark count rate when the incident X-ray photon energy is relatively high. Moreover, their time resolution is limited due to their operation mechanism. In conclusion, the semiconductor single X-ray photon detectors cannot provide high speed and high time resolution at the same time. Moreover, the long term exposure to high energy X-rays degrades the detector performance due to their crystalline structure or the multiple strained heterostructure interface of these detectors. These material and structural drawbacks are also limiting their applications as detectors with an ultra large sensitive area.

1.2.2 Superconducting stripe for X-ray photon detection

In 1989, Gabutti *et al.* used a superconducting stripe for 6 keV X-ray photon detection. In their research, 3.5 mm long, 0.2 - 1.5 μm wide, and 0.4 - 0.8 μm thick NbN or Nb stripes were fabricated by a standard photolithographic process. Though the photon energy is huge, the detection efficiency was relatively low due to the large cross section of the stripes. From the digital oscilloscope traces, the dead time for such devices (time for bias current recovery) was found to be ~ 2.5 μs [171].

Later, a 1.25 mm long, 2 μm wide, and 0.4 μm thick superconducting stripe of granular aluminum was used to detect the 6 keV X-ray photons from a ^{55}Fe source [172]. For this detector, a plateau in the DDE versus normalized bias current (I_b/I_c) was observed between 0.3 and 1. Such a detector is similar to the NbN and Nb superconducting stripe detectors, but it showed a slow response time ~ 3 ns and a signal rising time as high as 450 ns. Moreover, since the stripe was current-biased at a fraction of the critical current so that the hotspot propagated along the strip after switching, it was necessary to decrease the bias current to zero for ~100 ms so that the film completely recovered to the superconducting state before the bias current could be restored to its initial value for the next X-ray photon. Otherwise, the detector was latching into a resistive state, where it is no longer responsive to incident photons [172].

In order to build a faster, self-recovering superconducting stripe detector, a 550 μm long, superconducting granular W stripe with a rectangular cross section of $1.8 \times 0.24\ \mu\text{m}^2$ was used for detecting the X-ray photons [174]. However, a saturated DDE as a function of bias current was only observed at relatively low temperatures (~ 1.7 K). Though a 50 ns' recovery time was observed, the detector was still affected by the latching problem [174].

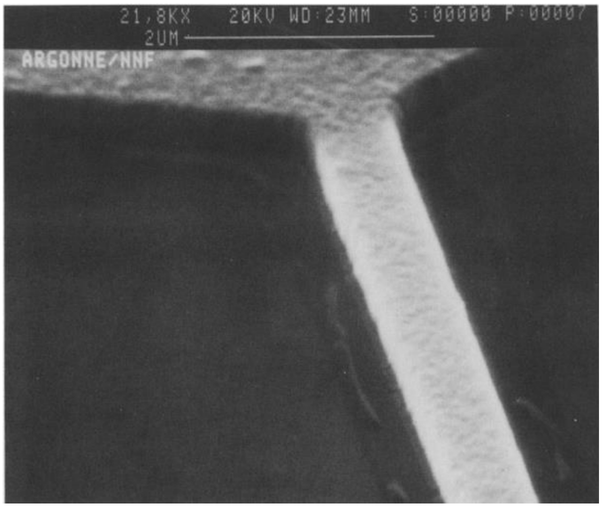

Fig. 1.6: Schematic diagram for the microstrip detector from Gabutti *et al.* [173].

The early stage superconducting stripe X-ray detectors based on highly disordered granular superconductors showed a long response time to X-ray photons, and the recovery time was up to the millisecond scale, which limited the count rate of these detectors. Moreover, the devices worked in a self-recovery mode only when the bias current was low, and only the granular W stripe detector showed a bias current self-recovery. When compared with a meander structure, these superconducting stripes have a small sensitive area, which does not allow for an efficient X-ray photon coupling.

1.2.3 Superconducting nanowire single X-ray photon detectors (X-SNSPDs)

Soon after the first detection of single visible and infrared photons with a superconducting nanowire, this idea was adopted for detecting high energy particles and keV-X-ray photons with relatively thick superconducting films.

Superconducting stripeline detectors (SSLDs), which are based on thick and ~ 1 µm (or less) wide superconducting stripes, were adopted by Suzuki *et al.* for time-of-flight mass spectrometry. They primarily used a very thin niobium nitride (NbN) film, and patterned it to a nanowire meander pattern with a thickness of 6.8 nm and a width of 200 nm on MgO substrate for detecting biomolecules ionized by laser radiation and accelerated by a static high voltage of 17.5 kV. This detector had a rise time of 640 ps and a fall time of about 50 ns, which was much faster than superconducting tunnel junction (STJ) detectors [175]. The relatively long rise time (360 – 640 ps) was due to the large kinetic inductance, which is also a key factor for the high-energy deposition in a range of over 10 keV [176]. Later, this type of detectors with thicker films (40 – 50 nm), wider stripes (1 – 2 μm), and much larger detecting areas (from 200 × 200 μm^2 to 2 × 2 mm^2) were fabricated for the same type of applications [177-185].

Until 2008, SNSPDs for visible and infrared photons based on NbN have been significantly improved. The response of 5 nm thick, 120 nm wide NbN based SNSPD to 6 keV X-ray photons was investigated by Lara *et al.* [185] (see in Fig. 1.7). This detector responded to 6 keV X-ray photons above a normalized bias current of $I_b/I_c = 0.7$. Due to the use of ultrathin films, the X-ray photon energy is mostly dissipated in the substrate, and a detection event is most probably indirectly induced by phonons from the substrate that are subsequently collected by the nanowire. This makes thin film based SNSPDs not suitable for detecting high energy X-ray photons [186].

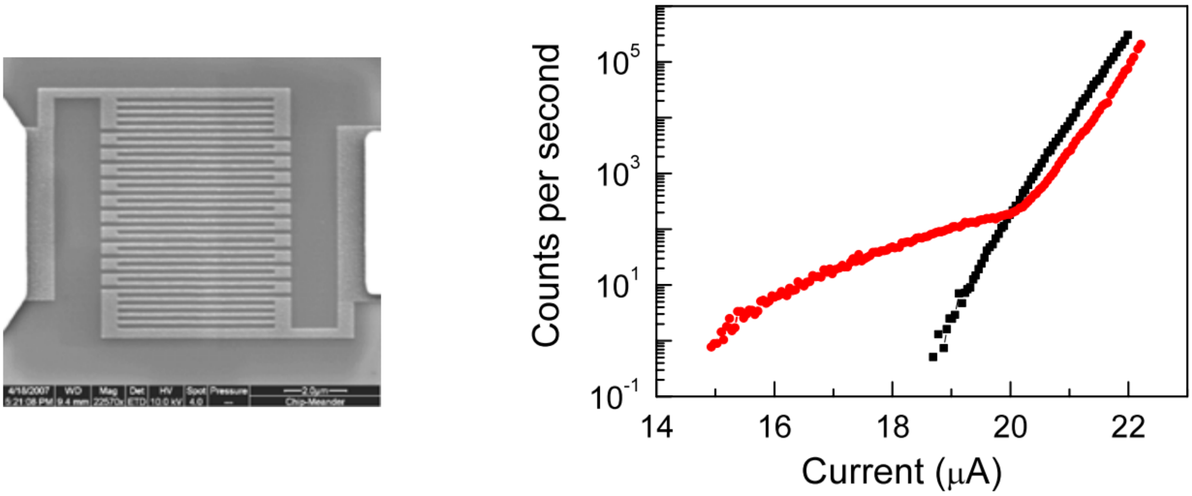

Fig. 1.7 Left: SEM Photo of the NbN SNSPDs used in Ref. [186]; Right: Count rate versus bias current with (red-dots curve) and without (black-squares curve) X-ray photons.

The first effective X-ray photon detection by a meander stripe structured superconducting nanowire was reported by Inderbitzin *et al.* in the University of Zurich [187]. Continuous X-ray photon counting detectors fabricated from a 100 nm thick Nb film were reported without dark counts, which was capable to detect photons even at reduced bias currents of 0.4%. Later on, the TaN (the heavy element tantalum can enhance the X-ray photon absorption) was also used for fabricating X-SNSPDs in the same research group. However, only the narrowest TaN detector with a wire width of 250 nm showed a promising X-ray photon detection performance at 1.85 K [188]. Currently, the best detection performance of X-SNSPDs to 10 keV photons has been achieved by us for amorphous WSi films [189], which we will discuss in detail in Chapter 6.

1.3 Advantages of amorphous superconducting X-SNSPDs

1.3.1 Radiation effects on semiconductor detectors

Currently, semiconductor-based X-ray diode, avalanche photodiode, and pixel sensors are the most commonly used X-ray detectors. These detectors, however, can be severely damaged by the radiation of X-ray photons. For example, the X-ray dose for Si pixel sensors at the European X-ray Free Electron Laser (XFEL) can be up to 1 GGy within three years [190]. Such a large X-ray irradiation dose can induce two kinds of radiation damage: bulk damage, which is due to the non-ionizing energy loss (NIEL) causing damage to the crystalline structure by incident particles; and interface damage, which is due to the ionizing energy loss of X-ray photons, causing a build-up of positive charges and traps in the SiO_2 and at the Si-SiO_2 interface.

Though the momentum of photons are relatively small, the induced secondary electrons still have enough energy to displace the lattice atoms, which in turn results in an interstitial atom (I) - vacancy (V) pair. For example, the threshold energy for displacing a Si atom to produce point defects is 25 eV [191]. X-ray photons induced defects can be classified as point defects (due to their low momentum), namely a Frenkel-pairs. The energy levels of these defects can be located in the bandgaps, which act as recombination or generation centers in semiconductor detectors. As a result, after a long term high energy particle irradiation, the leakage current or dark current will significantly increase.

The ionizing energy deposition induced degradation is due to the large number of electron-hole pairs created by the incident particles on their paths. Most of the electron-hole pairs are self- recombined but some of them can migrate into the materials. Especially at the Si-SiO_2 interface, some of radiation induced carriers cannot escape from this layer and form permanent charges in the insulating layer, which can be trapped at the interface between the silicon and the insulating layer. This effects can break the Si-O chemical bonds and induce dangling bonds in the interface. These interface effects can significantly degrade the detection performance of detectors.

1.3.2 Drawbacks of granular NbN detectors

NbN based superconducting detectors are more robust against the X-ray radiation effects due to the higher binding energy between Nb and N, and the interface effects can also be neglected due to the device structure of corresponding superconducting detectors. However, as it is discussed in chapter 1.1.2, these granular materials have more intrinsic defects or inhomogeneity problems for large area detector fabrication.

Gaudio *et al.* fabricated 100 nm wide nanowires with lengths ranging from 100 nm to 15 μm, and they found that the critical current was not independent of wire length but decreased with increasing length [192]. Their observations revealed that each nanowire showed an inhomogeneous distribution of I_c. This variation of I_c among nominally identical devices constituted a direct proof for the inhomogeneous nature of the wire. More specifically, a comparison between the experimental critical current and the Ginzburg-Landau (GL) depairing current suggested that inhomogeneity is the main reason for the observed low critical currents in long meanders.

In ultra large parallel superconducting NbN stripe detectors, a detector works in the single stripe switch regime because the kinetic inductance for a single long wire is large. The generated output pulses have varying amplitudes in such devices [177, 191], which indicates a non-uniform current distribution among the parallel strip-lines. In such detectors, the kinetic inductance for a single wire is around 2.1 nH, and for the remaining 4 parallel strips 0.5 nH in total, so that the current recovery time is less than 1 ns. As a result, the observed amplitude variation cannot be ascribed to an inadequate current recovery of the hit stripe-line mentioned in Ref. [184], but must be due to an intrinsic difference between the properties of these 1 mm long superconducting NbN stripes.

1.3.3 Advantages of amorphous WSi detectors

Highly disordered WSi materials can be deposited on various substrates at room temperature. A uniform and homogeneous WSi film can be deposited over an area as large as 4 inch in diameter (~ 10 cm), which favours the fabrication of X-ray photon number resolving detectors with a sensitive area in the centimetre scale. Moreover, as we have mentioned above, due to the modest substrate requirements for WSi, more complicated structures can be designed and fabricated to enhance the X-ray photon absorption probability. Currently, X-SNSPDs are commonly based on 100 nm thick superconductors. As a consequence, the effective X-ray photon absorption probability is confined in the several percentage range. By adopting a multi-layer structure (similar with the structures in Refs. [82, 98]) the detection efficiency of X-SNSPDs could be significantly improved. Thanks to the amorphous nature of these films, the radiation damage cannot play such a decisive role as in crystalline films. Even after long time exposure to keV electrons, the superconducting performance of a WSi detector does not show any signs of degradation. Therefore, amorphous WSi containing the heavy tungsten element is the perfect choice for high energy particle detection.

2 Film deposition

Currently, the most widely used methods for the SNSPDs fabrication are the top-down techniques and the lift-off method. The top-down techniques are based on nanolithography, in which the superconducting nanowires are protected by EBL resist and the gaps between the nanowires are etched away. All the detectors and structures in this work are fabricated by the top-down method. The superconducting films involved in this research, including WSi and NbTiN, have been deposited by magnetron sputtering at the FIRST Center for Micro- & Nanoscience of ETH Zürich.

2.1 Deposition of WSi

We used the plasma vapor deposition (PVD) technique via magnetron sputtering which is based on the superimposition of positive ions in the plasma accelerated by an electrical field onto the negatively charged electrode or target. These positive ions are at first accelerated by an applied voltage in order to obtain a kinetic energy ranging from a few hundreds to a few thousands of electron volts, and to bombard the negative electrode with sufficient energy to dislodge and eject atoms from the target. These atoms are ejected in a typical line-of-sight cosine distribution from the face of the target and are deposited on the substrate surface. In order to effectively dislodge atoms from the target, a magnetic field is applied on the electrode to trap the electrons perpendicular to the electric field between the cathode and anode, which enhances the efficiency of the initial ionization process for generating plasma at lower pressures. The W atoms are deposited through this dc sputtering process.

The electrical and thermal conductivities of Si are not as good as those of the metal targets. As a result, we have to adopt the radio frequency (rf) sputtering technique, which alternates the electrical potential of the plasma in the vacuum environment at radio frequencies to avoid a charge accumulation on certain types of sputtering target materials. For the dielectric target materials, the positive ions will accumulate on the surface of the target face giving it a positive charge after some time of the dc sputtering deposition. With the rf power, the electrons are attracted to the target material during the positive cycle, and the positive ions can be released, while during the negative cycle, the ion bombardmenting on the target continues the sputtering deposition.

In this way, superconducting amorphous W_xSi_{1-x} films were grown on silicon and sapphire substrates by dc magnetron sputtering of a pure W (99.95%) target and rf magnetron sputtering of a pure Si (99.999%) target in argon (Ar) atmosphere, at a total pressure of 3 mTorr.

2.1.1 Film thickness measurement

In order to deposit binary alloy materials with a specific stoichiometry, the deposition rate of each target needs to be determined. For the W target with dc sputtering, the deposition rate is relatively large (~ 3.44 nm/min at 50 W), while for the Si target with rf sputtering, the deposition power is limited to 75 W, and therefore the deposition rate is relatively low (~ 0.6 nm/min at 50 W). In order to deposit a W_xSi_{1-x} film with $x = 0.75$ or 0.8, the power for the W target is kept around 20 ~ 40 W, while the power for Si is kept at 50 ~ 70 W, depending on the expected stoichiometry.

Fig. 2.1: A schematic picture of thick films used for deposition rate measurements.

The deposition rate is obtained from the resulting film thickness and the deposition time. In order to minimize any deposition rate fluctuations, the deposition time for this process is relatively long. For the W target with higher deposition rate, the deposition time is set to more than 1 hour, and for the Si target the corresponding time can be as long as 3 hours. We firstly deposited materials onto a glass substrate with patterns marked either with photon resist or with printing ink. Then the patterns on the glass substrate were lifted off after deposition in hot acetone and isopropanol, as it is shown in Fig. 2.1.

The film thickness was measured by a *Dektak* surface step profiler, which is able to do a 3D mapping of the films. Figure 2.2 shows a measurement for a 520 nm thick film. Since the uncertainty of this method is larger than that of an atomic force microscope (AFM), a thick film is used for this measurement.

In order to determine the exact films thickness, more than 30 groups of data were collected and the films thickness *d* was averaged from these data.

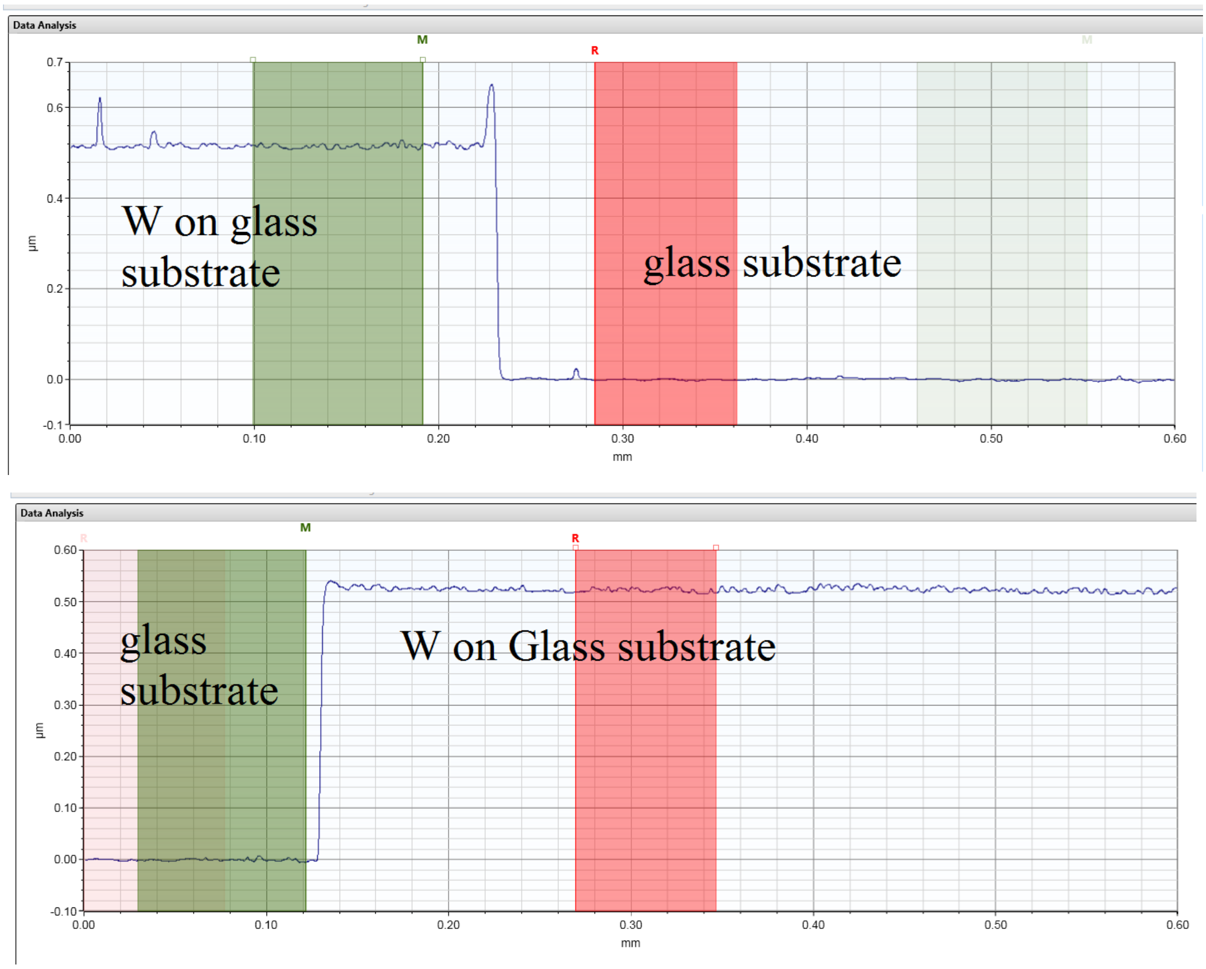

Fig. 2.2: Film thickness measured by a *Dektak* surface step profiler.

2.1.2 Deposition rate of W and Si targets

From the measured films thickness and deposition time, we can accurately determine the deposition rate of each target. By choosing different deposition rates, materials with the expected stoichiometry can be deposited. The deposition rate is solely determined by the power applied on the magnetron when the other deposition parameters are fixed. The resulting deposition rate dependence on the power is shown in Fig. 2.3.

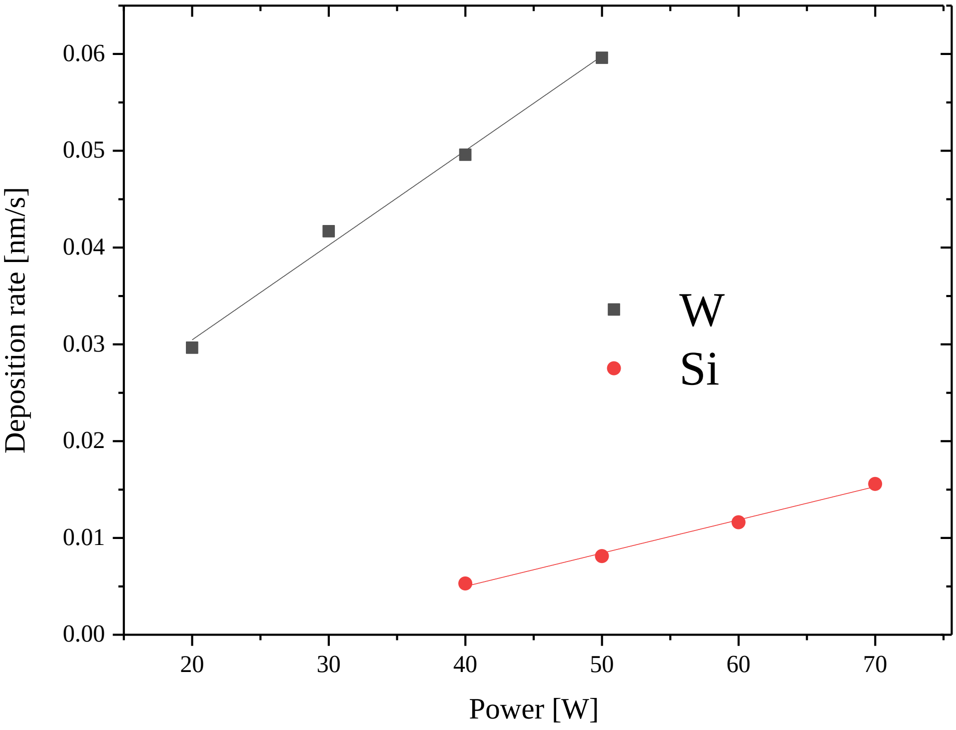

Fig. 2.3: Deposition rate as a function of applied power on the magnetron. The solid lines are a linear fit to the data.

The determined deposition rates for W and Si are $r_{\mathrm{W}} = (9.77 \cdot 10^{-4} \times P + 1.07 \cdot 10^{-2})$ nm/s and $r_{\mathrm{Si}} = (3.36 \cdot 10^{-4} \times P - 0.83 \cdot 10^{-2})$ nm/s, respectively. A standard atomic volume method is used to determine the deposition power and deposition time according to the measured deposition rates and the expected film thickness. For growing $\mathrm{W_xSi_{1-x}}$, the stoichiometry ratio is defined as $C_{\mathrm{W}}/C_{\mathrm{Si}} = x/(1-x)$ and the atomic volume ratio for WSi is $\Omega_{\mathrm{W}}/\Omega_{\mathrm{Si}} = 9.53/12.10 = 1.27$. If the expected film thickness is d, then the relative film thicknesses for W and Si are

$$d_\mathrm{W} = \frac{d}{1+(\Omega_\mathrm{W}/\Omega_\mathrm{Si})/(C_\mathrm{W}/C_\mathrm{Si})},\ d_\mathrm{Si} = d - d_\mathrm{W}. \tag{2.1}$$

According to the desired deposition time t, the deposition rate can be obtained through

$$r_\mathrm{W} = d_\mathrm{W}/t \text{ and } r_\mathrm{Si} = d_\mathrm{Si}/t, \tag{2.2}$$

which in turn determines the power applied on the magnetron. For example, to grow a 5 nm thick $W_{0.8}Si_{0.2}$ film, with a deposition time of 108 s, the input power for W is 24.8 W and the input power for Si is 58 W. To exactly control the film thickness, the co-sputtering deposition rate with two input values has been re-calibrated, however.

The stoichiometry of the resulting deposited films was examined by energy-dispersive X-ray spectroscopy (EDX) on sapphire substrate, and the films thicknesses were checked by atomic force microscope (AFM) techniques.

2.1.3 Sheet resistance

For the SNSPDs fabrication, nearly all the processes are based on 4 – 8 nm thick films. In this case, the calculation of the resistivity based on some bridge structures is not so accurate due to film thickness variations. In a 2D geometry, the sheet resistance R_S is a much more convenient quantity to characterize the thin films, and it is one of the most basic properties of thin films. For a bridge structure or other patterned structures, the total resistance can be written as

$$R = \rho\frac{L}{dw}. \tag{2.3}$$

Here ρ is the specific resistivity, L is the length, d is the thickness, and w is the width of the structure. R_S is defined through

$$R = R_\mathrm{S}\frac{L}{w},\ R_\mathrm{S} = \frac{\rho}{d}, \tag{2.4}$$

i.e., the resistance per m^2 of a film of thickness d.

The most significant advantage of using the sheet resistance is that it can be directly measured by the four-point Van der Pauw method. This method was proposed by L. J. van der Pauw in 1958, and it can be used to measure the specific resistivity or Hall effect of arbitrarily shaped flat samples [193].

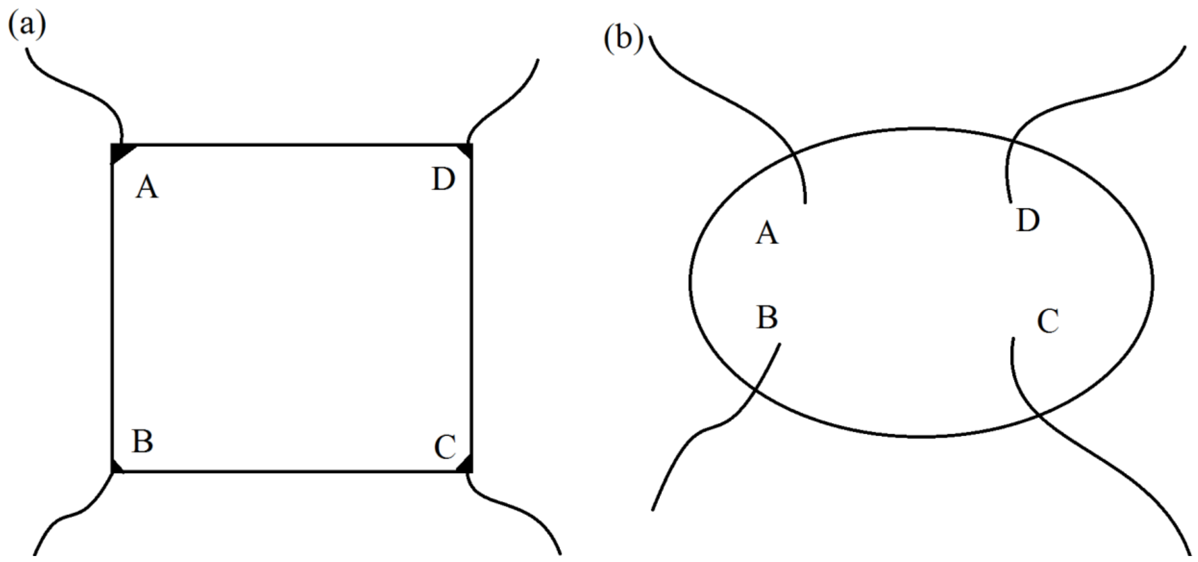

Fig. 2.4: A schematic diagram of a square shaped sample (a) and a general configuration (b) for a Van der Pauw measurement.

Figure 2.4 shows a schematic diagram of wire bonding for a Van der Pauw measurement. A specific resistance $R_{\mathrm{AB,CD}}$ is defined by the potential difference between contact pads C and D per unit current through contact pads A and B. A relationship between $R_{\mathrm{AB,CD}}$ and $R_{\mathrm{BC,DA}}$ can be written as [192]

$$\exp(-\pi R_{\mathrm{AB,CD}}/R_{\mathrm{S}}) + \exp(-\pi R_{\mathrm{BC,DA}}/R_{\mathrm{S}}) = 1. \tag{2.5}$$

The sheet resistance is uniquely determined by the measured specific resistance, and it can be written in the form

$$R_{\mathrm{S}} = \frac{\pi}{\ln 2}\left(\frac{R_{\mathrm{AB,CD}}+R_{\mathrm{BC,DA}}}{2}\right) \cdot f\left(\frac{R_{\mathrm{AB,CD}}}{R_{\mathrm{BC,DA}}}\right), \tag{2.6}$$

where f is a function of the ration $\frac{R_{\mathrm{AB,CD}}}{R_{\mathrm{BC,DA}}}$, which satisfies

$$\frac{R_{\mathrm{AB,CD}}-R_{\mathrm{BC,DA}}}{R_{\mathrm{AB,CD}}+R_{\mathrm{BC,DA}}} = f \cdot \operatorname{arccosh}\left\{\frac{\exp(\ln 2/f)}{2}\right\}. \tag{2.7}$$

This standard Van der Pauw method, however, is not so suitable for our simple measurements since the substrates used in this research are cut from a 3 inch or 4 inch wafer, and the edges of the square are defective. As a result, a modified Van der Pauw method has to be applied instead, which is also suitable for films with an arbitrary shape as shown in Fig. 2.4(b). By applying a current between the contact pads on one side (e.g. between A and B in Fig. 2.4(b)), we measure the voltage on the other side (between C and D). The measurements are repeated by changing the current and voltage terminals clockwise, resulting in four different voltages. Finally the sheet resistance is

$$R_\mathrm{S} = \frac{\pi}{8\ln 2}\sum_{n=1}^{4}\left(\frac{V_n+V_{n+1}}{I}\right)\cdot f\left(\frac{V_{n+1}}{V_n}\right), \tag{2.8}$$

where the Van der Pauw function is given by

$$\frac{\frac{V_{n+1}}{V_n}-1}{\frac{V_{n+1}}{V_n}+1} = \frac{\operatorname{arccosh}\left(\frac{\exp(\ln 2/f)}{2}\right)}{\ln 2/f}. \tag{2.9}$$

Commonly, for a square homogeneous sample, V_n and V_{n+1} are rather close to each other, and the modification function $f\sim 1$ [194].

As a cross-check, we compared the result for a microbridge measured by the modified Van der Pauw method and by a bridge measurement with known geometry, and the obtained R_S are perfectly consistent. Table 2.1 shows corresponding values for a 5 nm thick 4×4 mm^2 $W_{0.75}Si_{0.25}$ film. The sheet resistance for 5 nm thick films as a function of the composition is displayed in Fig. 2.5.

TABLE 2.1 Van der Pauw measurement for a 5 nm thick 4×4 mm^2 $W0_{.75}Si_{0.25}$ film, with a bias current of 1 mA.

Voltage [mV]	Modification factor f	Sheet Resistance R_S [Ω]
$V_1 = 85.539$	0.999996	388
$V_2 = 85.878$	0.999982	
$V_3 = 84.651$	0.999967	
$V_4 = 86.360$	0.999996	

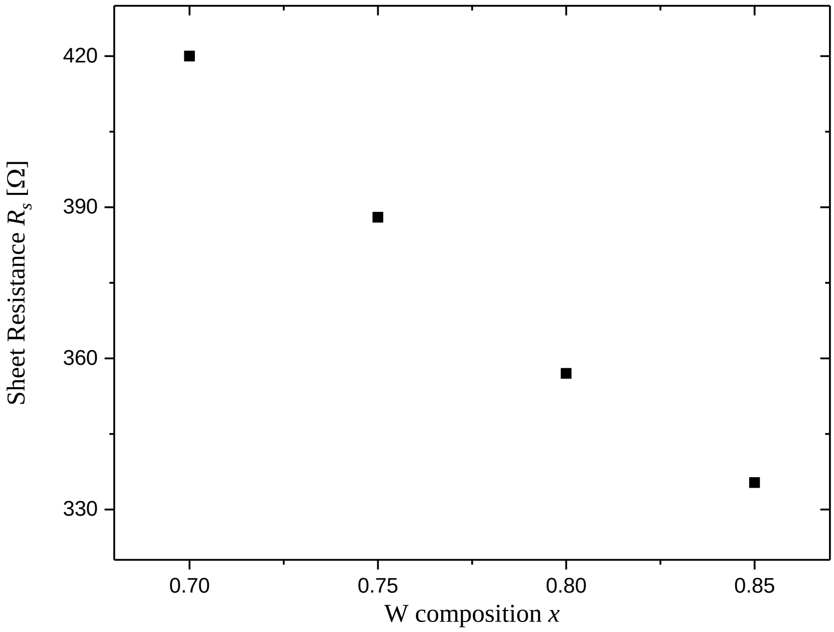

Fig. 2.5: Room temperature sheet resistance as a function of the W composition for 5 nm thick W_xSi_{1-x} films.

2.1.4 Optimization of the critical temperature T_c

In 1990， Suzuki *et al*. found a substantial increase of the superconducting transition temperature of W films prepared by low-pressure chemical vapour deposition (LPCVD) using tungsten hexafluoride (WF_6) and silane (SiH_4) up to T_c ~ K [195], which is considerably higher than T_c of crystalline W (T_c ~ 0.01 K) [196]. This effect has been ascribed to the amorphous structure of the films as a result of Si impurities. With respect to WSi compounds, there are two kinds of known compounds, W_5Si_3 and WSi_2. The critical temperature of these crystalline WSi compounds, however, are much lower than those of the corresponding amorphous structures [197-200]. For the amorphous WSi, Kondo investigated the critical temperature as a function of the W composition in detail, and found a maximum T_c ~ 5 K for Si contents ranging between 15% and 35% [201]. In Ref. [76], Baek *et al*. also studied the T_c dependence on the film thickness. The optimization of WSi deposition with respect to T_c is therefore based on these studies, and a T_c ~ 5 K can be achieved for relatively thick films of the order of ~ 50 nm.

By optimizing the Ar gas flow, the deposition pressure in the chamber and the rotator speed, WSi films with comparable and even higher quality can be deposited. In Fig. 2.6, we compare the superconducting transitions for 100 nm thick and 5 nm thin $W_{0.8}Si_{0.2}$ films. The 100 nm film shows a superconducting transition at ~ 5 K, while the 5 nm film has a T_c ~ 4 K.

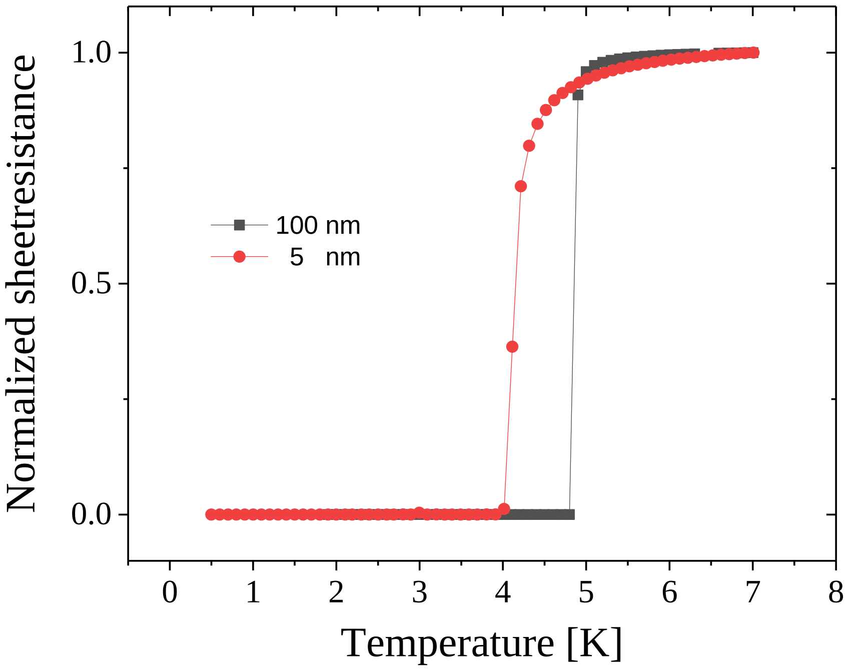

Fig. 2.6: Normalized square resistance for a 100 nm thick and a 5 nm thin $W_{0.8}Si_{0.2}$ film.

2.1.5 Amorphous nature of WSi

For amorphous WSi films deposited on a polished Si substrate, it is nearly impossible to see any characteristic structure using a scanning electron microscope (SEM). In order to examine and compare the structures and morphologies between films with different quality, we performed $\theta - 2\theta$ measurements.

Figure 2.7 shows the $\theta - 2\theta$ X-ray scanning profiles of two 100 nm thick $W_{0.8}Si_{0.2}$ films with very different critical temperatures. In Fig. 2.7 (a), the corresponding film has a T_c of 4.9 K, which no characteristic peaks appear except for the characteristic peak from the Si substrate at 33°. This indicates a highly disordered or amorphous nature of the WSi film. The film investigated in Fig. 2.7 (b) has a reduced T_c of 3.8 K, and three distinct reflection peaks appear. These peaks can be attributed to either the β-W crystal structure or the WSi_2 compound. At any rate, these phases have much lower critical temperatures than the amorphous W_xSi_{1-x} at optimum x between 15% and 30%.

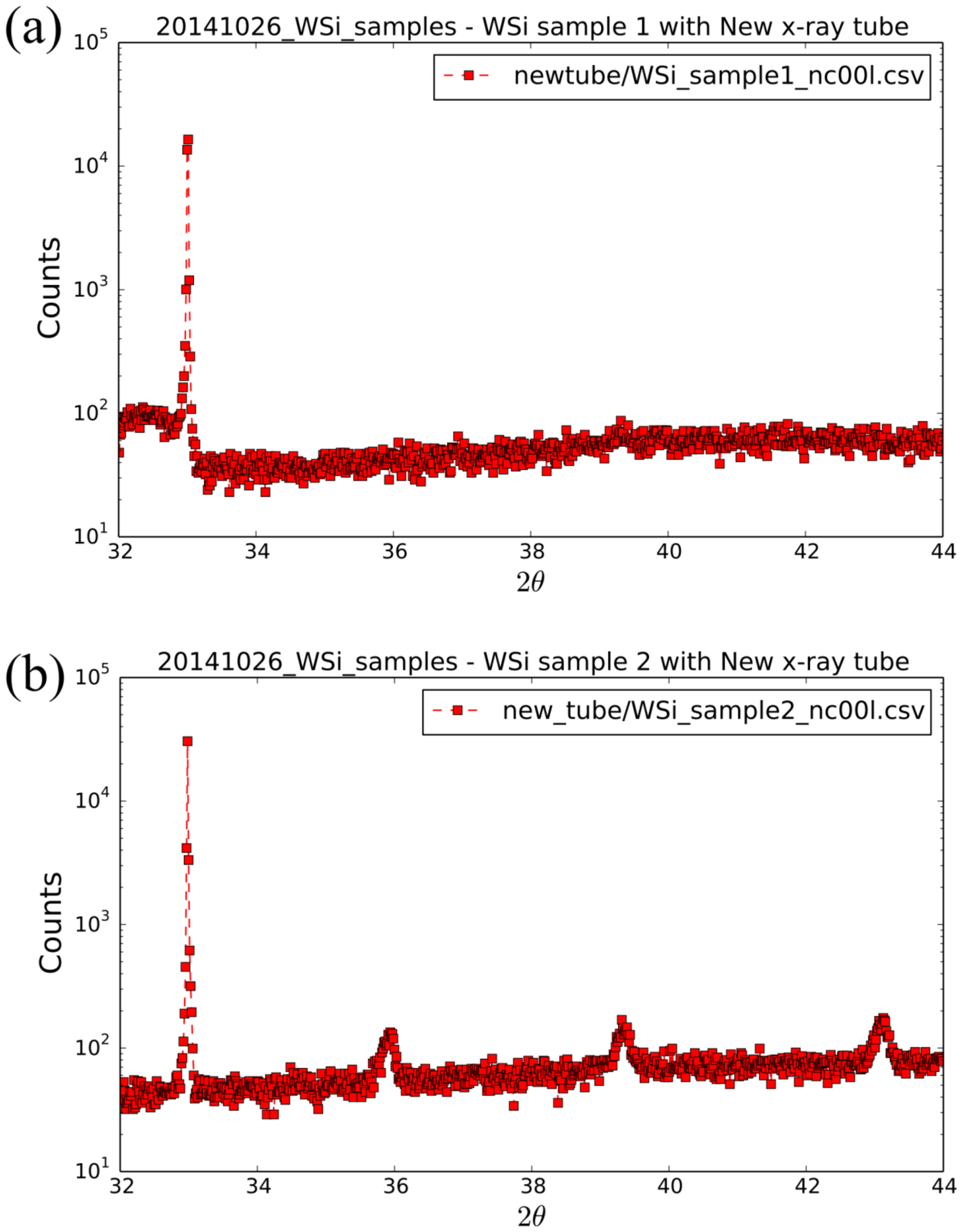

Fig. 2.7: $\theta - 2\theta$ profiles of a $W_{0.8}Si_{0.2}$ film with a T_c of 4.9 K (a), and a $W_{0.8}Si_{0.2}$ film with a reduced T_c of 3.8 K (b).

2.2 Deposition of NbTiN

2.2.1 Reactive sputtering deposition

Reactive sputtering deposition is a sputtering process where the target material (e.g. a $Nb_{0.8}Ti_{0.2}$ alloy) is sputtered in the presence of a gas or a mixture of gasses (e.g. Ar + N_2) that may partially react with the target material to form materials with different chemical composition (e.g., a compound $Nb_{0.8}Ti_{0.2}N$). In most cases, argon is the main gas during the sputtering process due to the high relative atomic mass and its inert nature. The amount of a reactive gas introduced into a process chamber is controlled to either achieve a certain amount of doping, or to produce a fully reacted compound.

At ambient conditions, N_2 is inert and stable, and does not react with most metals. In a plasma (which is primarily formed by the inert argon), however, the nitrogen atoms become reactive. They at first react with the surface of the sputtering target, and are subsequently sputtered away. Therefore, the composition of the deposited films can be controlled by adjusting the relative amounts of the inert and the reactive gases. As a result, the spatial distribution of the reactive gas inside the chamber dominates the quality and homogeneity of the deposited films. In order to produce a homogeneous film, it is necessary to inject the gases as uniformly as possible to the entire plasma around the cathode.

2.2.2 Deposition of $Nb_{0.8}Ti_{0.2}N$ at ambient temperature

It has been reported that $Nb_{0.8}Ti_{0.2}N$ thin films can be deposited on a MgO substrate without intentionally heating the substrate [120]. We therefore attempted to deposit $Nb_{0.8}Ti_{0.2}N_x$ at ambient temperatures on SiO_x substrates. A niobium titanium ($Nb_{0.8}Ti_{0.2}$) target with 99.95% purity was used with a target size of three inch in diameter. The plasma discharge was performed at a total pressure from 1 mTorr to 7 mTorr in a mixture of argon (Ar) and nitrogen (N_2) gases with various gas compositions.

Direct current power sputtering was used to stabilize the discharging state, and different powers were applied on the magnetron to optimize the deposition conditions. Three different 5 nm thick films are deposited with a dc power of 50 W, 100 W and 150 W at ambient temperature. Figure 2.8 shows the superconducting transitions of the resulting films in the low temperature range. With increasing power, T_c increases and the resistivity is lowered. This can be explained by a scenario in which a higher dc power leads to a certain heating of the substrate by a large number of deposited hot molecues. Indeed, films deposited at higher temperatures did not show this peculiar power dependence of T_c. With even higher powers, only the deposition rate was improved, and the discharge power on the magnetron was therefore fixed at 100 W.

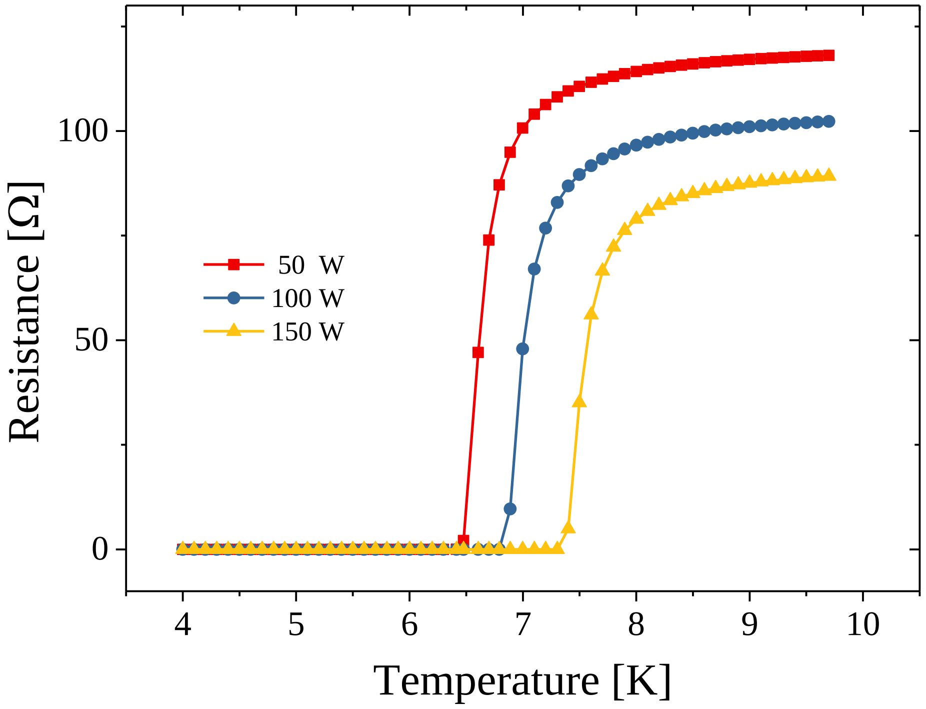

Fig. 2.8: Discharging power dependence of the superconducting transition for 5 nm thick $Nb_{0.8}Ti_{0.2}N_x$ films.

After optimization of the power, we also tried to optimize the chamber pressure with respect to the transition temperature T_c, varying the deposition pressure from 1 mTorr to 7 mTorr, but keeping other deposition conditions unchanged. Figure 2.9 shows the corresponding superconducting phase transitions for different films at different deposition pressures with the same deposition time.

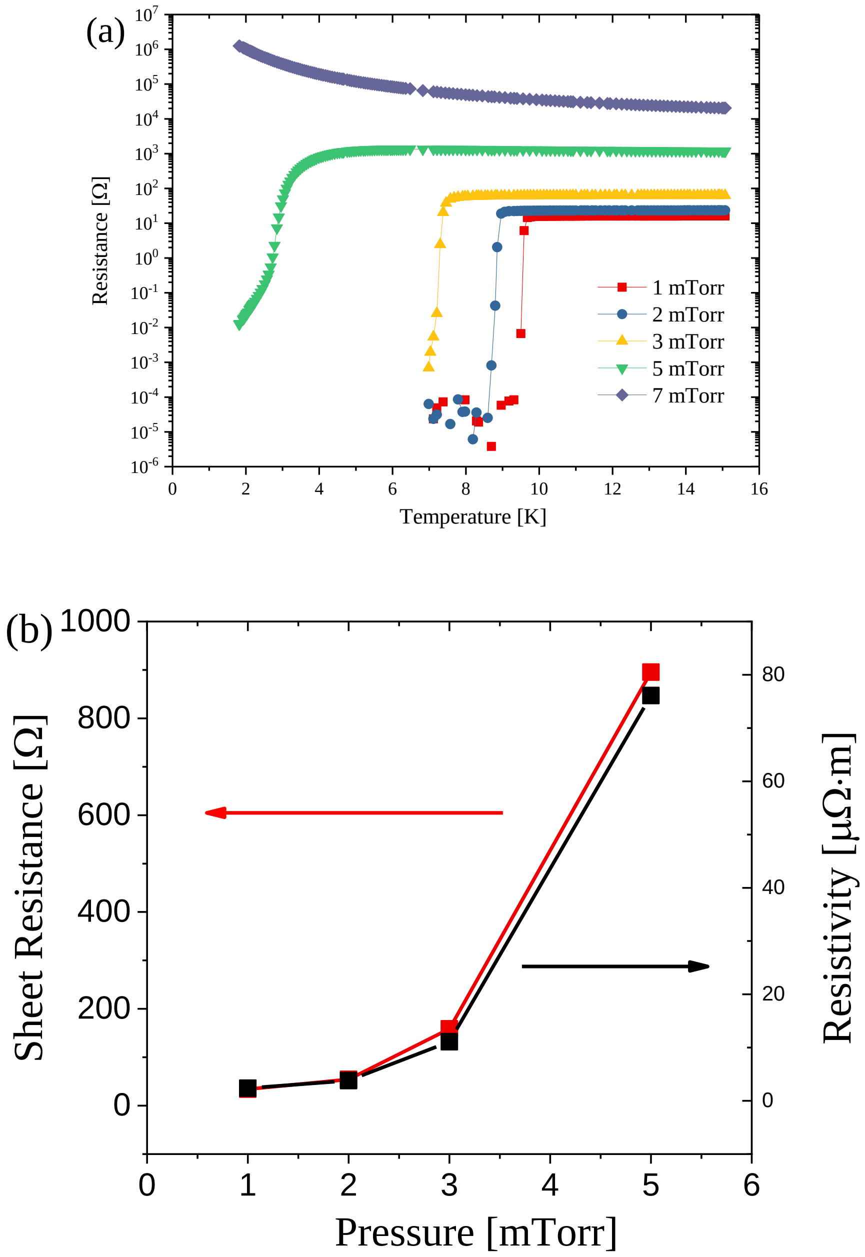

Fig. 2.9: Influence of the chamber pressure on the superconducting transition. (a) Resistance as a function of temperature near T_c. (b) The corresponding normal-state sheet resistance and resistivities.

In the low pressure range, T_c ranges from 9 to 10 K, and decreases with increasing the pressure. At room temperature, it is nearly impossible to measure the sheet resistance of this 7 mTorr film with the modified Van der Pauw method, which is two orders of magnitude higher than film deposited at 5 mTorr, as it is shown in Fig. 2.9(c). Based on these results, we fixed the chamber pressure to 1 mTorr during sputtering, which is the lowest applicable pressure in the deposition chamber. However, there are also certain risks using such a low pressure for plasma deposition: (a) the pressure control gate is not stable, and thus the pressure is not stable; (b) the plasma is not stable and can even quench sometimes; (c) the composition of the resulting films is not homogenous. Moreover, the plasma cannot be ignited with a shielding cover, and the best way for ignition is to firstly ignite the plasma at a higher pressure and then gradually decrease it to the expected pressure.

With respect to the film quality dependence on the Ar and N_2 gas content, the ambient growth condition was studied by changing different gas mixures. At first, the Ar gas flow was fixed at 20 sccm (standard cubic centimeters per minute), and the N_2 gas flow ranged from 1 sccm to 5 sccm. The resulting transition temperatures T_c monotonically decrease with increasing N_2 gas flow in the chamber, as it is shown in Fig. 2.10.

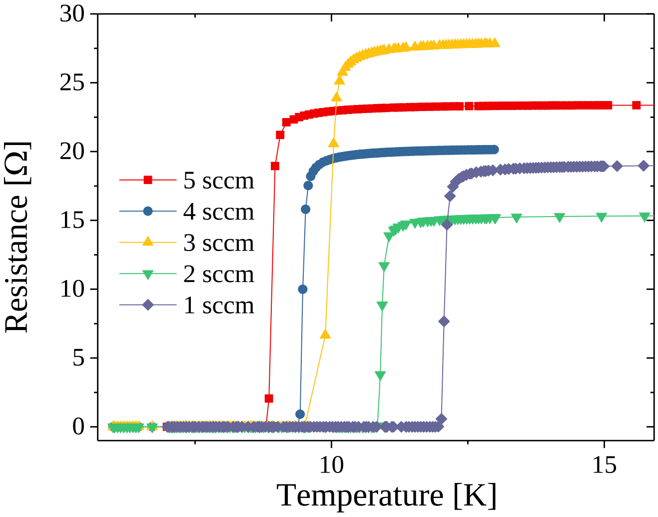

Fig. 2.10: N_2 content dependence of the superconducting transition temperature T_c.

Unfortunately, all these ambient temperature film deposition experiments (without intentionally heating the SiO_x substrate), did not reproduce the quality of $Nb_{0.8}Ti_{0.2}N$ thin films grown on MgO substrates. First, the lattice mismatch between SiO_x and NbN is much larger than that between MgO and NbN (a_{SiO2} = 4.91 Å). Second, the lowest pressure that can be achieved is limited around 10^{-6} Torr. As a result, the contamination from the impurity gas can hardly be eliminated. Finally, the distance between the target and the substrate in our case is much larger (more than 60 cm) than the reported distance for a deposition on the MgO substrate (0.6 cm in Ref. [120]). As a result, molecules that arrive at the substrate are less active and a more disordered film is deposited.

2.2.3 Deposition of $Nb_{0.8}Ti_{0.2}N$ on a heated substrate

Although the film quality deposited at the ambient temperature on SiO_x/Si turned out to be moderate, we found that increasing the substrate temperature resulted in films as good as those using an MgO substrate. After heating the substrate up to 600 ℃ within 20 min, the materials were sputtered onto the substrates at stable high temperature. After the film deposition, the heating power was turned off and the substrate was cooled back to the ambient temperature in the vacuum chamber.

Figure 2.11 (a) shows the superconducting transition for a 200 nm thick film deposited at 600 ℃. This square film was cut from a 3 inches substrate, and the T_c was measured on a small square near the edge, which indicates that large uniform NbTiN films can be deposited on a Si/SiO_x substrate by magnetron sputtering. In Fig. 2.11 (b), we compare the quality of films deposited at ambient temperature with those deposited at elevated temperature. Both films have a nominal film thickness of 70 nm, which is controlled by the deposition rate and the deposition time. The more disordered film deposited at ambient temperature has a sheet resistance nearly twice as large as that of the high temperature deposited film. We conclude that thin films with a T_c above 10 K can be successfully prepared on a heated Si/SiO_x substrate, which are excellently suitable for the SNSPDs fabrication.

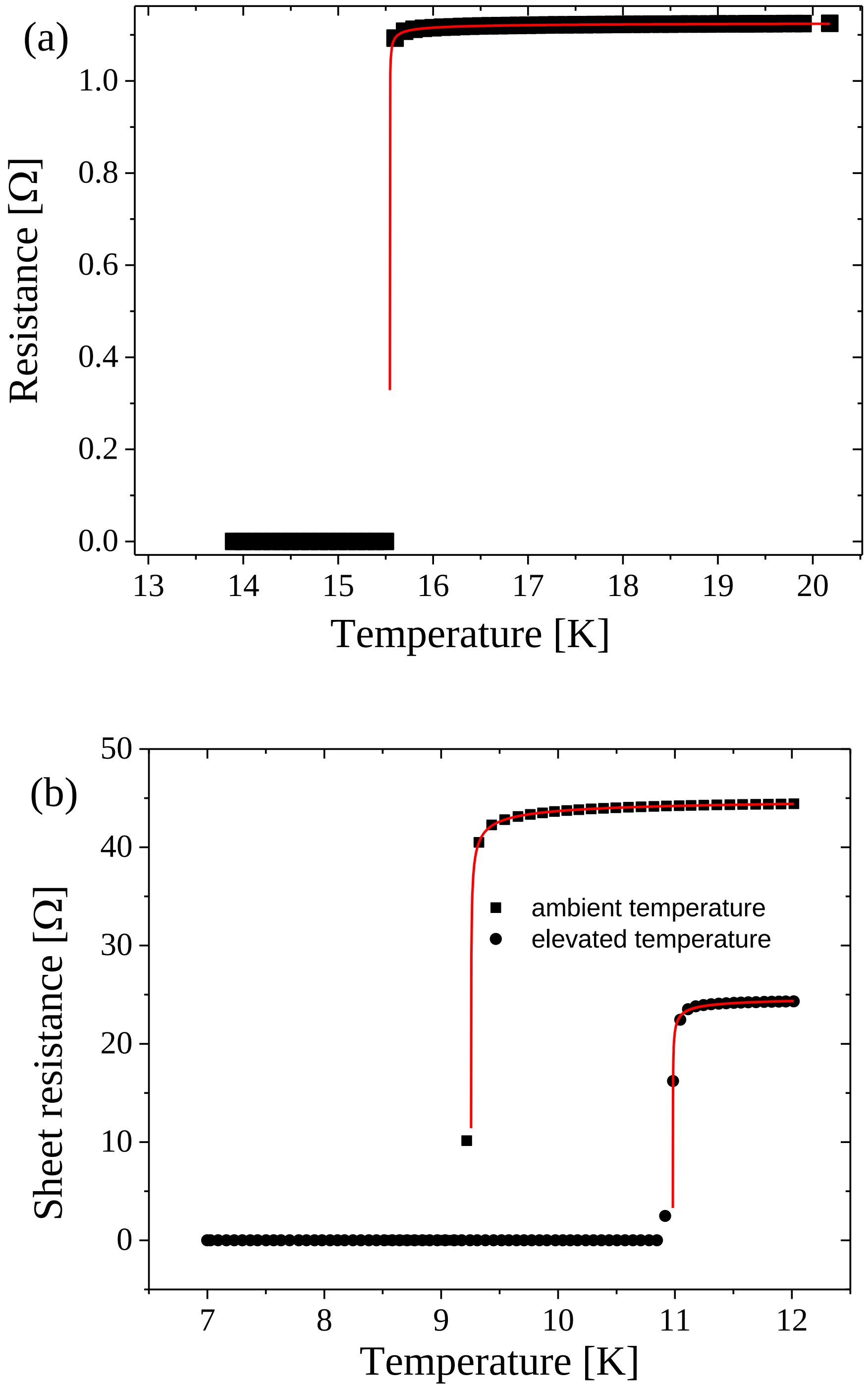

Fig. 2.11: (a) Transition to the superconducting state in a 200 nm thick film deposited at 600 ℃ on SiO_x/Si. (b) A comparison of the superconducting transitions between films deposited at ambient and elevated temperature. The bulk NbTiN films have a T_c around 15.5 K, which is as high as corresponding films grown on MgO.

3 Fabrication of superconducting nanowires

In order to effectively detect photons with an energy ~ 1 eV, the nanowire width (~ 100 – 150 nm) for WSi can be wider than that of a NbN wire due to the ≈ five times larger photon-induced hotspot (See later in chapter 3.5). EBL technology is commonly used for writing such narrow superconducting nanowires. Here we compare the use of positive ZEP 520 resist with results using negative HSQ resist for the nanowire writing by inspecting the SEM images of the resulting nanowires.

Before using the EBL to write the SNSPDs on the substrate, gold pads and a coordinate system are defined by optical lithography, as it is shown in Fig. 3.1.

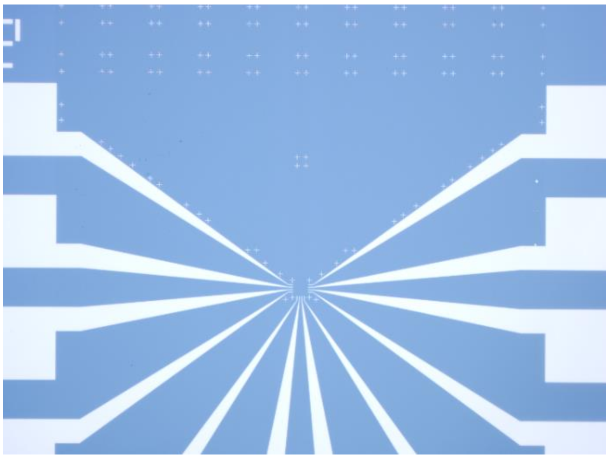

Fig. 3.1: The gold pads for the readout of the signals. The crosses in the picture are used for the coordinate system alignment.

3.1 ZEP 520

After baking the substrate at 190 ℃ for 10 minutes, the ZEP resist was spun onto the substrate with a spinning speed of 6000 rpm. Then the resist at the edge of the substrate was removed by using acetone on Q-tips. Afterwards, the substrate was baked at 198 ℃ for 30 min.

The EBL writing was performed with a 30 keV electron beam and an aperture size of 10 μm. The exposure dose was set to 100 $\mu C/cm^2$ for the EBL writing. Afterwards, the substrate was developed with pure n-Amylacetate at 11.5 ℃. Figure 3.2 shows an SEM image of a resulting WSi nanowire structure using ZEP 520. These wires have relatively large cross-section variations, larger than in those fabricated by using HSQ (see in chapter 3.2). As a result, the distribution of the bias current is not uniformly homogenous, and the resulting detection performance is position dependent.

Although the achieved spatial resolution of nanowires written with ZEP 520 is limited, the superconducting properties of such nanowires after this positive-resist process are more or less unchanged, since for a positive resist, the nanowire area is not irradiated by the energetic electrons. This is particularly important for the crystalline NbN structures used for the SNSPDs fabrication.

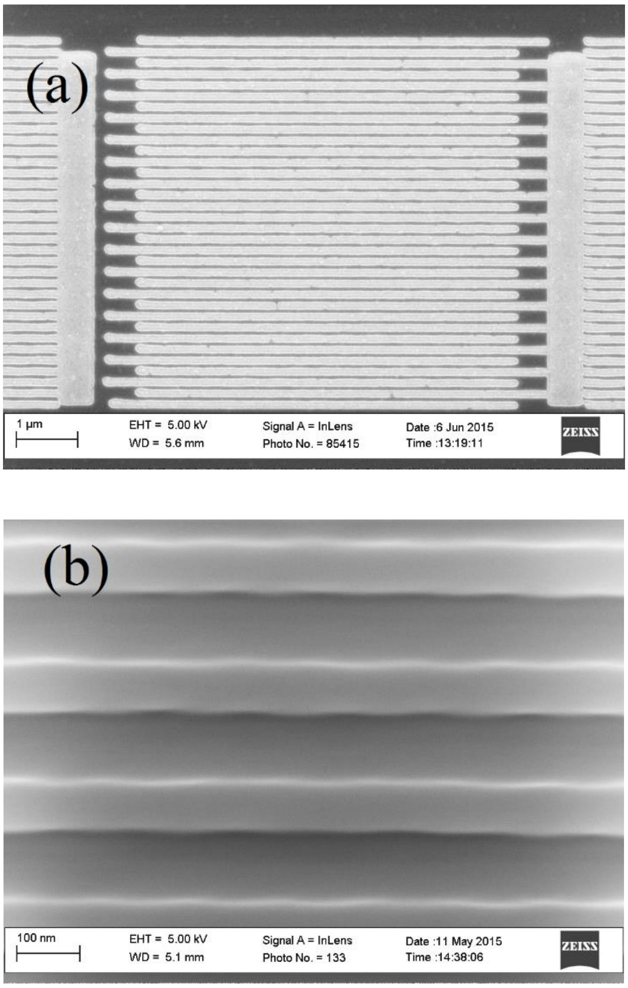

Fig. 3.2: (a) Narrow periodic WSi nanowires written by the ZEP 520. (b) An enlarged view of the center area of the meander wires.

3.2 HSQ

At present, the use of a high-resolution, negative-tone inorganic HSQ resist allows for a resolution of sub-10 nm [298]. Moreover, the SNSPDs fabrication process can be significantly simplified by using the HSQ, because the SNSPDs fabrication only involves two steps of lithography (an optical lithography and an EBL) instead of a three steps in lithography methods based on the positive resist.

At first, the substrate is baked at 180 ℃ to ensure a good attachment of the resist, and then the HSQ resist is spun onto the substrate or the sample with a speed of 6000 rpm for one minute. After the spinning, the sample is ready for EBL writing. When compared with the positive ZEP 520, the subsequent baking process with HSQ can be omitted. A striking characteristic of HSQ is the much higher EBL exposure dose, (up to 700 $\mu C/cm^2$, nearly 10 times higher than that of the ZEP 520), which decreases the influence from the beam current on the wire width. The exposed sample can be directly developed at room temperature. Figure 3.3 shows the SEM images for a periodic WSi nanowire prepared with HSQ.

In principle, a 100 nm wide periodic nanowire structure based on a 4 ~ 5 nm thick WSi film is sufficient for detecting single visible and infrared photons. However, for NbN, narrower nanowires are needed to detect infrared photons with high efficiency. Figure 3.4 shows a series of 20 nm wide nanowires from a 5 nm thick $Nb_{0.8}Ti_{0.2}N$ film prepared with HSQ.

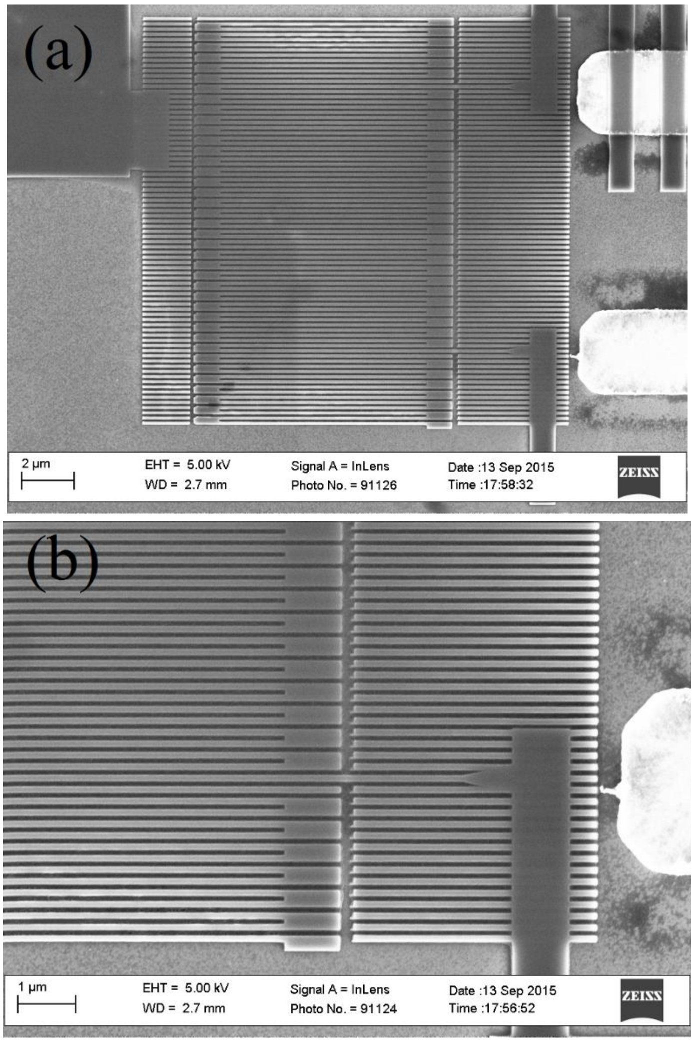

Fig. 3.3: (a) SNSPDs based on WSi film prepared with HSQ. (b) An enlarged view of the readout area of the detector. The wire width is 100 nm.

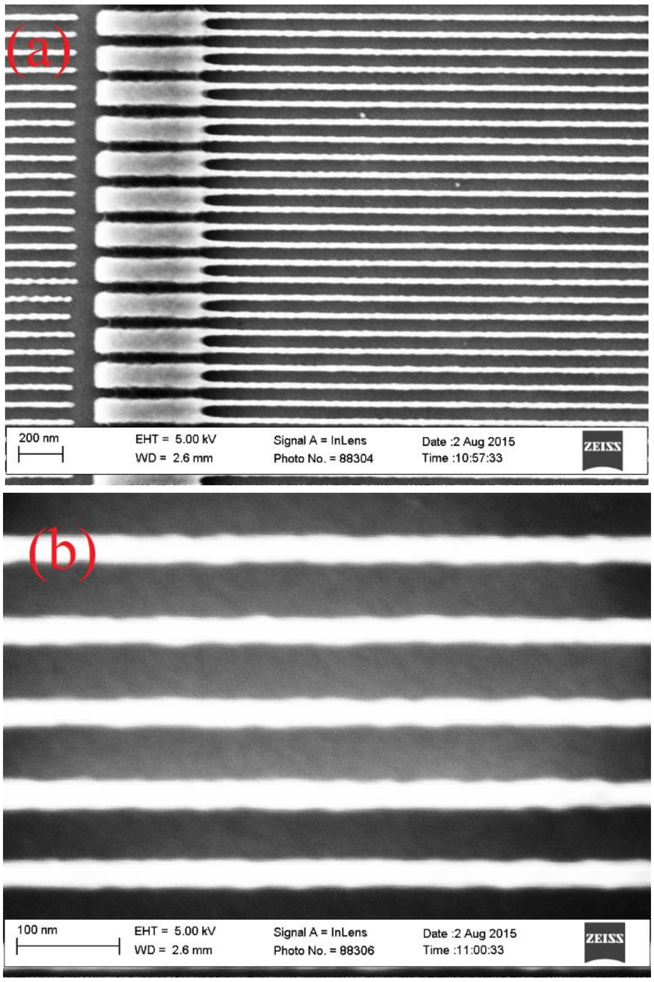

Fig. 3.4: (a) A 20 nm wide nanowire of a 5 nm thick $Nb_{0.8}Ti_{0.2}N$ film prepared with HSQ. The pitch (the period of the meander wire) is 80 nm, which is smaller than the commonly used 200 nm. (b) An enlarged image of nanowires for checking the wire width.

3.3 Wet etching for large scale YBCO stripes

With respect to the detection of keV X-ray photons, the induced hotspot size in a film can be as large as several hundred nanometers. Therefore, a stripe with a wire width as large as several micrometers can still be adopted for X-ray photon detection. In order to improve the X-ray absorption efficiency, the film thickness can also be several hundreds of nanometers. For the ceramic $YBa_2Cu_3O_7$ (YBCO) film (from *ceraco ceramic coating GmbH*), the dry etching (e.g. reactive ion etching) is very difficult. For instance, using a 200 W Ar milling, the etching rate is only around 0.7 nm/min. Moreover, in order to avoid overheating of the sample during etching, it is preferable to etch the sample in intervals. As a result, the etching of YBCO films can last as long as several hours.

To simplify the fabrication process of YBCO detectors, we adopt a wet etching method. At first, the stripes are defined by optical lithography with the positive resist AZ6632. Then the gaps (or unwanted YBCO film area) between the stripes are removed by the orthophosphoric acid (H_3PO_4) with a concentration of 1%. Figure 3.5 shows the resulting meander stripes of YBCO with a wire width of 2 µm.

In figure 3.5 (c), we compare the resistive transitions before and after fabrication. The as-grown YBCO film has a T_c ~ 83 K, which is already lower than that in crystalline YBCO (T_c ~ 93 K). After fabrication, the YBCO stripes shows a certain degradation of T_c by around 3 K. In principle, these structures are still superconducting at liquid nitrogen temperature. Whether they are able to detect single X-ray photons or not, is subject to future experiments.

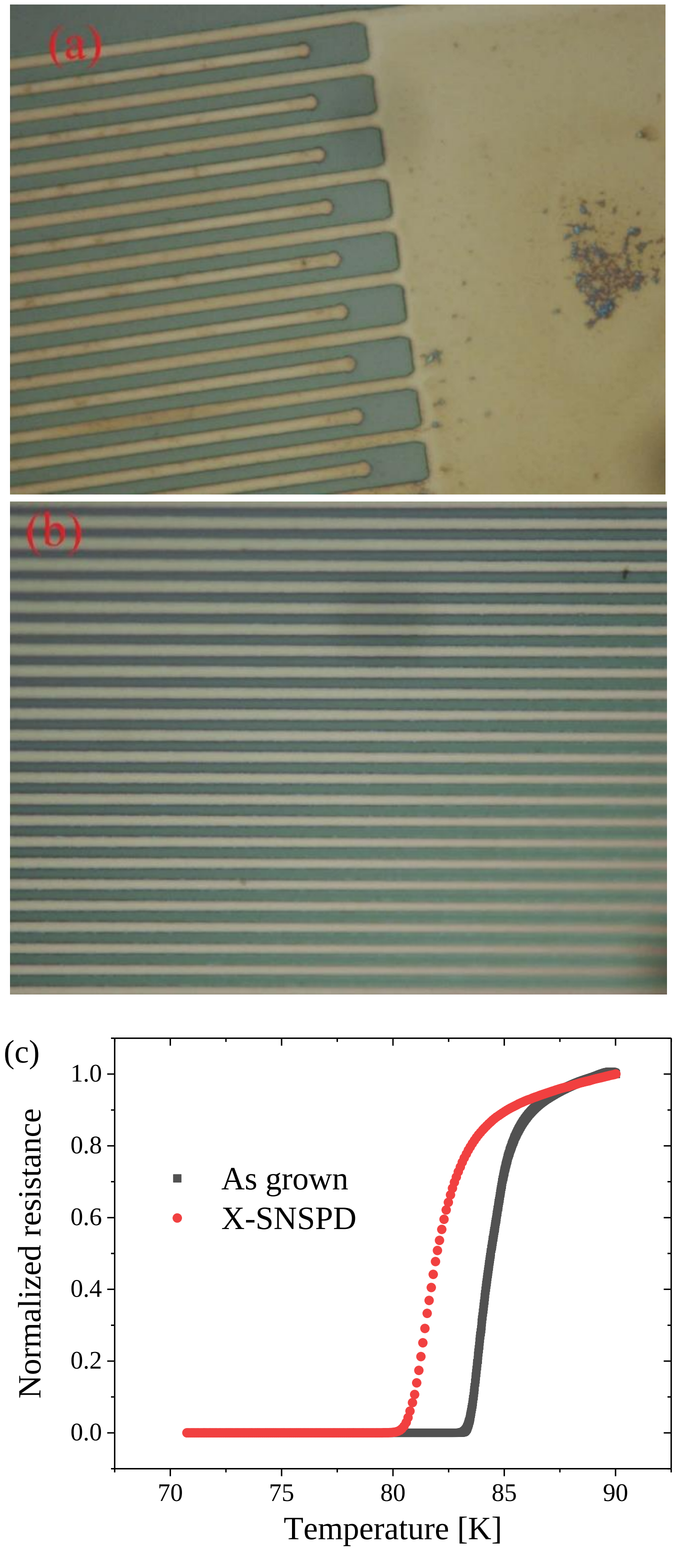

Fig. 3.5: (a) and (b) SEM images of the YBCO periodic stripes fabricated by wet etching. (c) Superconducting transition for the YBCO film and the patterned stripes for an X-SNSPDs.

3.4 Fabrication of superconducting WSi microbridges for transport measurements

Superconducting amorphous a-$W_{0.75}Si_{0.25}$, $W_{0.8}Si_{0.2}$ and $W_{0.85}Si_{0.15}$ films were grown on silicon substrates by means of dc magnetron sputtering of a pure W target, and rf magnetron sputtering of pure Si in argon atmosphere, at a total pressure of 3 mTorr. The resulting film thickness d was inferred from the predetermined growth rate and deposition time, and were also confirmed by Atomic Force Microscope (AFM) measurements. After the W and Si co-sputtering deposition, another ~ 1.5 nm silicon layer was deposited on top of the films surface.

The freshly deposited films were baked at 180 ℃ with hotplates HP 160 III BM for 10 min. The temperature accuracy is ± 1 ℃ over the 110 mm diameter. Afterwards, the thermally stable positive resist AZ6632 was spun onto the substrate, followed by a 1 min after-baking at 117 ℃. Near the edge of the substrate, there is a resist accumulation due to the surface tension. For contact photolithography, the maximum achievable resolution is proportional to $\sqrt{g \cdot \lambda}$, where g is the gap between the substrate and the mask, and λ is the exposure wavelength [203,204]. The resist accumulation near the substrate edge will lead to a large gap between the central part of the substrate and the mask, thereby decreasing the resolution and accuracy of optical lithography. As a result, the *edge removal* must be performed before the photolithography. By placing an $8 \times 8\ \mathrm{mm}^2$ square absorbing medium in the center of the substrate and flood exposing UV light in the lamp test mode, the edge area becomes soluble in the AZ 726 MIF developer. After developing, the substrate was exposed to λ = 325 nm light, and the patterns were transferred onto the substrate.

The exposed area was subsequently removed by reactive ion etching (RIE). The etching was performed with a base pressure less than 5×10^{-5} Torr, and the etching pressure is set at 15 μbar. The gases used for this process were Ar (30 sccm) and SF_6 (10 sccm), and the etching power was limited to 20 W. Under these etching conditions, the etching rate for WSi was around 200 nm/min.

The resulting bridge widths were ranging from 10 μm to 200 μm, with a constant bridge length of 500 μm. Each bridge contains six contacts for resistivity and Hall effects measurements (in this research, we only performed resistivity measurements, however). For each stoichiometry, five films were deposited, with films thicknesses of 5 nm, 10 nm, 20 nm, 50 nm and 100 nm. The geometrical dimensions of the microbridges were measured through SEM images, and the result shows that the uncertainty in the bridge width is much less than 1% (see in Fig. 3.6). All the calculations and data analyses to be presented in next chapters are based on the geometries determined by SEM measurements and the nominal films thickness.

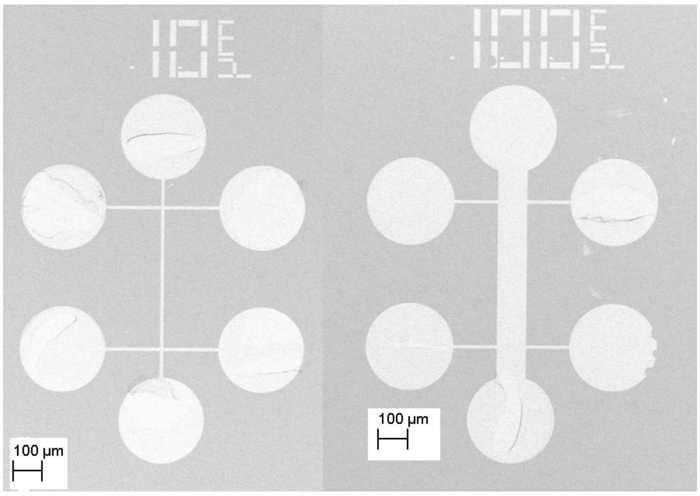

Fig. 3.6: SEM image of a WSi microbridge used for transport measurements.

3.5 Fabrication of a 50 Ω microbridge

In order to trace the recovery of superconductivity (namely the relaxation time of the hotspot) in a time-resolving experiment, we used a bow-tie microbridge. The microscopic images of the bow-tie and the whole structure are presented in Fig. 3.7.

Figure 3.7 (a) shows a microscopic image of a microbridge using two-step lithography method. We firstly deposited the gold contacts by optical lithography and lift-off methods. The bridge structure (in the center between these two gold contacts) was subsequently defined by EBL, and the residual WSi (black area) was etched away by reactive plasma etching. The bridge length with this simple method is fixed at 3 um. The resulting impedance of the bridge is thus determined by adjusting the bridge width.

A more sophisticated fabrication process of the microbridge included three lithographic steps, which adjusted both the bridge width and the length. Two small gold pads (see the inset in Fig. 3.7(b)) were patterned onto the WSi film by means of EBL. Then, these pads were separated by a slit, which defines the length *L* of the microbridge (see the enlarged part in Fig. 3.7(b)). PMMA resist with a thickness of 150 nm on top of WSi film was exposed using 10 kV electron beam with a dose of 120 $\mu C/cm^2$. The Nb / Au bi-layer consisting of 8 nm Nb and 100 nm Au was deposited on top of the WSi film by magnetron sputtering at a partial pressure of $P_{Ar} = 5 \times 10^{-3}$ mbar. The lift-off process was carried out in a warm acetone and ultrasonic bath. To pattern the large contact pads, the substrate was covered by photo-resist with a thickness of 950 nm. By the subsequent photolithography, magnetron sputtering and lift-off processes, a three-layer Nb/Au/Nb (8 / 250 / 15 nm) sandwich was formed on the surface of the substrate. The width of bridge, *W*, was defined by the EBL over negative resist. Finally, the WSi microbridge was etched using Ar ion milling. During the etching process, the upper Nb layer of the large contact pads protected the gold layer from Ar ions milling. The dimensions (*L* and *W*) of the microbridge in the slit of the bow-tie and the embedding co-planar transmission line were designed in such a way that the microbridge in the normal-state and the line had a total impedance of approximately 50 Ω (see the inset in Fig. 3.7(b)). The widths of all microbridges are kept the same (5 μm), while the length varied between 700 and 900 nm. In the time-resolving experiment, the beam of a femtosecond pulse laser with a wavelength of 800 nm was positioned over the center of the bow-tie. The beam diameter at the bow-tie was much larger than both *L* and *W* to ensure uniform excitation of the microbridge. The electric response to the laser pulses was monitored with a time-resolving readout with a resolution 1.25 ps (see in chapter 5.3).

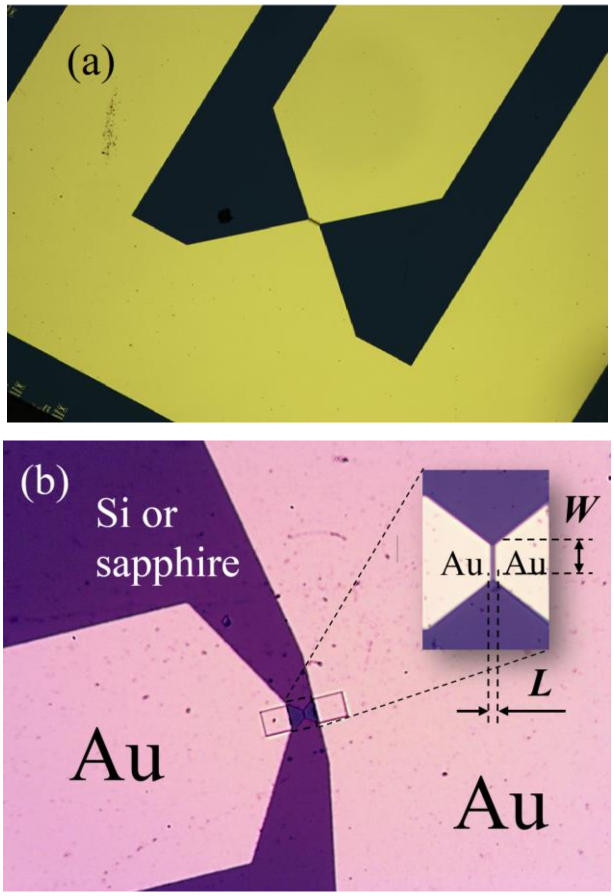

Fig. 3.7: SEM images of the specimens used for the measurements of τ_R. (a) The microbridge fabricated by using the two-step lithography method. The calculations are based on the measured strip geometries. (b) The bow-tie structure used for the τ_R measurements. The inset shows the enlarged sensitive area and the WSi microbridge located between the two gold pads.

4 Physical properties

4.1 Motivation

So far, the highest detection efficiency reported in SNSPDs has been achieved in the WSi material system [19]. In order to achieve a good system detection efficiency, researchers have used different superconducting materials for the SNSPDs fabrication, as it is summarized in chapter 1. The system detection efficiencies, however, varied considerably among the SNSPDs based on these superconducting materials as various meander geometries and waveguides were adopted. The role of the material parameters affecting the detection performance have still been poorly understood.

A very important limiting factor of the intrinsic detection efficiency is the constriction in the SNSPDs [51]. Non-uniformity of the superconducting film or local imperfection within the nanowire, which are introduced during the structuring process, can result in a reduction of the critical current, which in turn severely suppresses the internal quantum efficiency. Amorphous thin superconducting films are generally much more homogeneous at a relevant length scale from a few nanometers up to a few tens of nanometers as compared to the crystalline granular films. But this effect alone cannot explain the extraordinary performance of WSi-SNSPDs. Intuitively, an incident photon breaks more Cooper pairs in films with a smaller superconducting energy gap, thus the resulting detection efficiency should be higher. Indeed, superconductors with the smaller energy gap do extend the resulting SNSPDs’ saturation regime of intrinsic efficiency towards longer wavelengths. However, the system detection efficiency of the wire-structure remains relatively low and is limited by its optical absorption, which can be improved by the optimization of either geometry or material of the wire-structure. Besides the wire geometry and the superconducting energy gap, other factors restricting the detector performance have not been clearly investigated. An indication that material parameters are indeed important for the detection mechanism and the performance of SNSPDs has come from a comparison between NbN and NbC [202].

In order to understand the remarkable improvement of detection efficiency for WSi-SNSPDs, we need to obtain a detailed knowledge about the physical properties of the WSi films beyond their superconducting transition temperature. To achieve this, we studied the electronic transport parameters of WSi films with different thicknesses. We prepared WSi microbridges with different widths and thicknesses (see in chapter 3.4). By measuring the superconducting transition under different magnetic fields, we derived the relevant superconducting transport parameters, and we present the results in the following.

4.2 Critical temperature T_c

The critical temperature T_c is the most basic property for the superconducting phase transition. T_c is commonly determined from the temperature dependence of bridge sheet resistance $R_S(T)$, which is calculated from the measured total resistance and the bridge geometry. We use a wedge wire bonder for electrical connections, and four contacts are connected for the R_S measurements. The microbridges are then characterized by their normal state resistivity and the superconducting critical parameters. The resistivity measurements were performed in a physical property measurement system (PPMS from *Quantum Design*) in magnetic fields up to 9 T perpendicular to the microbridge surface. In Fig. 4.1, we show the zero field transition to superconducting state for a thick (d = 100 nm) film and a two dimensional (d = 5 nm) film.

Due to the amorphous nature of WSi, the temperature dependence of the sheet resistance does not follow the general behaviour of metallic films between room temperature and the temperature where superconducting fluctuation become relatively strong. In the relatively high temperature range (far away from the fluctuation regime), the R_S increase with decreasing temperature, which is due to the weak localization effects that stems from quantum-interference of the conduction electrons on the defects of the systems (see in chapter 5 for more details).

With decreasing temperature, R_S reaches its maximum at $T \approx 14$ K for the 100 nm thick $W_{0.8}Si_{0.2}$ film and at ≈ 25 K for the 5 nm thick $W_{0.8}Si_{0.2}$ film, as it is shown in Fig. 4.1. As the temperature continuously decreases further, the film enters the regime where superconducting fluctuations become relevant. In the fluctuation regime, short lifetime Cooper pairs are formed thus decreasing the resistance. As a result, the total conductance is the sum of the normal conductance from the electrons and the fluctuating conductance from the Cooper pairs channel. The mean-field superconducting transition temperature T_c can be estimated by taking into account the contribution from fluctuating Cooper pairs to the total conductivity [205-207]. When expressed in terms of the measured square resistance, this contribution for three (3D) and two (2D) dimensional films takes the forms,

$$R_S(T) = \frac{1}{\frac{1}{R_{SN}} + \frac{1}{32} \cdot \frac{e^2}{\hbar \xi(0)} \cdot d \cdot \left(\frac{T_c}{T-T_c}\right)^{0.5}}, \tag{4.1}$$

$$R_S(T) = \frac{1}{\frac{1}{R_{SN}} + \frac{1}{16} \cdot \frac{e^2}{\hbar} \cdot \left(\frac{T_c}{T-T_c}\right)}, \tag{4.2}$$

where e is the elementary charge; $\hbar$ is the reduced Planck constant; $\xi(0)$ is the coherence length; d is the film thickness; and R_{SN} is the normal-state square resistance. In Eqs. 4.1 and 4.2, the superconducting fluctuation conductance is taken as the Aslamazov-Larkin (AL) fluctuation conductivity [205-207]. However, in the highly disordered WSi films, Maki-Thompson (MT) fluctuation due to coherent scattering of Cooper pairs on impurities also plays a important role near the superconducting fluctuation regime. In the 3D case, the MT fluctuation conductance can be written as

$$\sigma_{3D}^{\mathrm{MT}} = \frac{1}{8} \cdot \frac{e^2}{\hbar\xi(0)} \cdot d \cdot \left(\frac{T_c}{T-T_c}\right)^{0.5}. \tag{4.3}$$

In the 2D case, the MT fluctuation is very complicated and will be discussed in next chapter. The resulting total resistance for 3D and 2D films becomes

$$R_{\mathrm{S}}(T) = \frac{1}{\frac{1}{R_{\mathrm{SN}}} + C \cdot \left(\frac{T_c}{T-T_c}\right)^{0.5}}, \tag{4.4}$$

$$R_{\mathrm{S}}(T) \approx \frac{1}{\frac{1}{R_{\mathrm{SN}}} + D \cdot \left(\frac{T_c}{T-T_c}\right)}. \tag{4.5}$$

In the inset of Fig. 4.1, we show the best fitting based on the equations above. For the 3D fitting in Fig. 4.1 (a), $T_c \approx$ 4.94 K, which is rather close to T_c estimated from $R_{\mathrm{SN}}/2$ standard. If we simply view R_{SN} as $R_{\mathrm{S}}(7\text{ K})$, then the $R_{\mathrm{SN}}/2$ standard gives $T_c \doteq$ 4.95 K. The fitted R_{SN} value of 18.9 Ω, is slightly larger than the measured sheet resistance of 18.6 Ω. This is reasonable since at 7 K, the superconducting fluctuations are still strong and lower the total resistance from the true normal state resistance. With respect to the fitting parameter $C = \frac{5}{32} \cdot \frac{e^2}{\hbar\xi(0)} \cdot d$, C is obtained as $4.6 \times 10^{-4}\ \Omega^{-1}$ from the fitting. From the measured $\xi(0) = 6.5$ nm (see more details later), C can be calculated as $5.8 \times 10^{-4}\ \Omega^{-1}$, which is slightly larger than the fitted result.

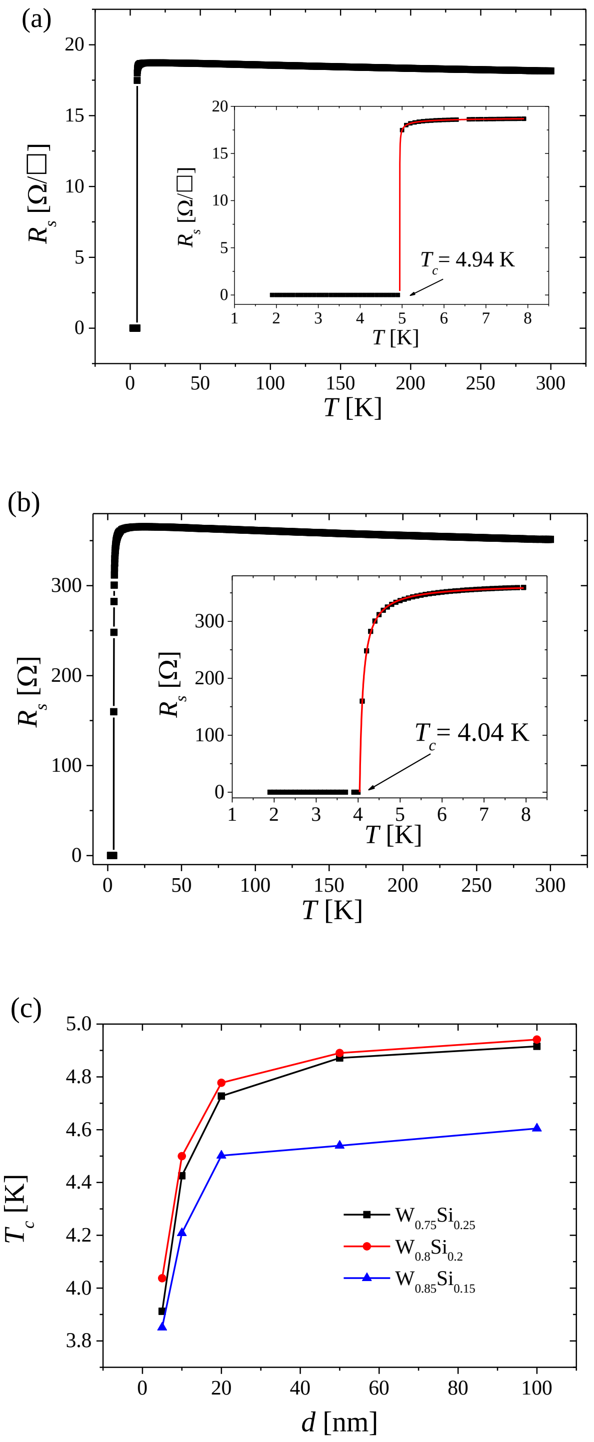

Fig. 4.1: (a) Sheet resistance as a function of temperature for the 100 nm thick and 100 µm wide W$_{0.8}$Si$_{0.2}$ bridge. (b) Temperature dependence of the square resistance for the 5 nm thick and 100 µm wide W$_{0.8}$Si$_{0.2}$ bridge. The red lines in the inset show the best fitting based on Eq. 4.4 and Eq. 4.5. (c) Thickness dependence of T_c for WSi films.

With regard to the 2D scenario for the 5 nm thick film, the best fit using Eq. 4.5 gives a T_c of 4.04 K, which is slightly smaller than that from the $R_{\mathrm{SN}}/2$ standard, ~ 4.1 K. The fitted normal state sheet resistance $R_{\mathrm{SN}} = 366\ \Omega$ is also slightly larger than the measured $R_{\mathrm{SN}} = 357\ \Omega$.

Films with a thickness larger than 10 nm were fitted with the 3D expression, and the 2D expression was used for thinner films. This criterion of choosing the formulas for films with differenct thickness is consistent with the calculated coherence length (see in the subsection 4.4). The film thickness dependence of T_c for all these three stoichiometries is shown in Fig. 4.1 (c).

4.3 Sheet resistance in different magnetic fields

In order to derive the transport parameters of WSi, the sheet resistance as a function of temperature is measured in different magnetic fields for all bridges. In Fig. 4.2, we show the $R_S(T,B)$ for the 100 nm thick and the 5 nm thick bridge with a bridge width of 100 µm.

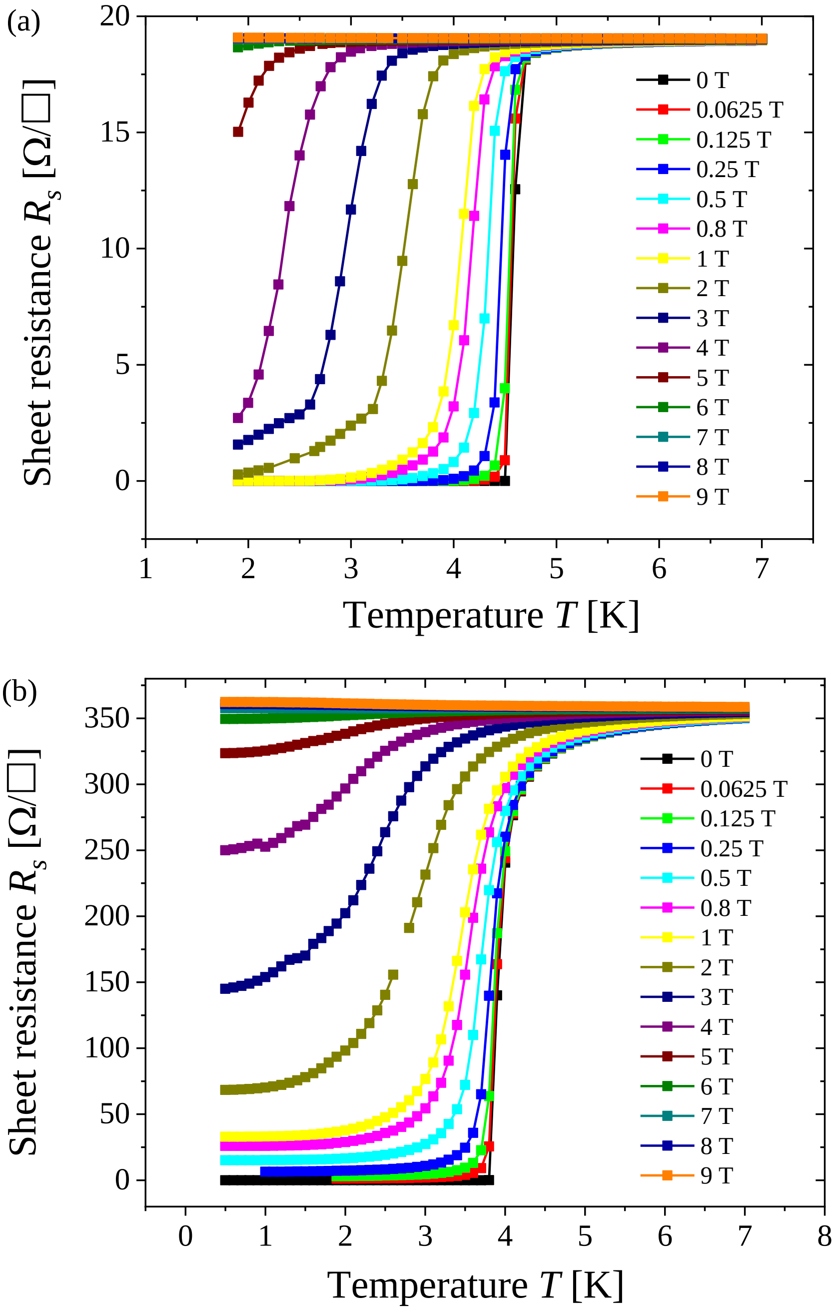

Fig. 4.2: Temperature dependence of sheet resistance at different magnetic fields. (a) R_s from the 100 nm thick 100 µm wide bridge. (b) R_s from the 5 nm thick 100 µm wide bridge.

By measuring the superconducting transitions in different magnetic fields, the magnetic field dependence of the transition temperature $T_c(B)$ from $R_{\mathrm{SN}}/2$ standard was obtained. According to the Ginzburg-Landau theory, $T_c(B)$ should be approximately linear at temperatures close enough to $T_c(0)$, as it is depicted in Fig. 4.3. The critical field at zero temperature for each film can then be estimated by linearly extrapolating the values to zero temperature. The thicker films exhibit a larger slope and higher T_c, thus resulting in a larger critical field. The experimental data deviate from the linear dependence when the applied magnetic field is comparatively large or small. However, these linearly extrapolated $B_{c2}(0)$ values are commonly larger than the actual critical fields, and must be multiplied with a factor of 0.69 to obtain realistic values [208, 209]. The linearly estimated $B_{c2}(0)$ values for different samples are listed in table 4.1.

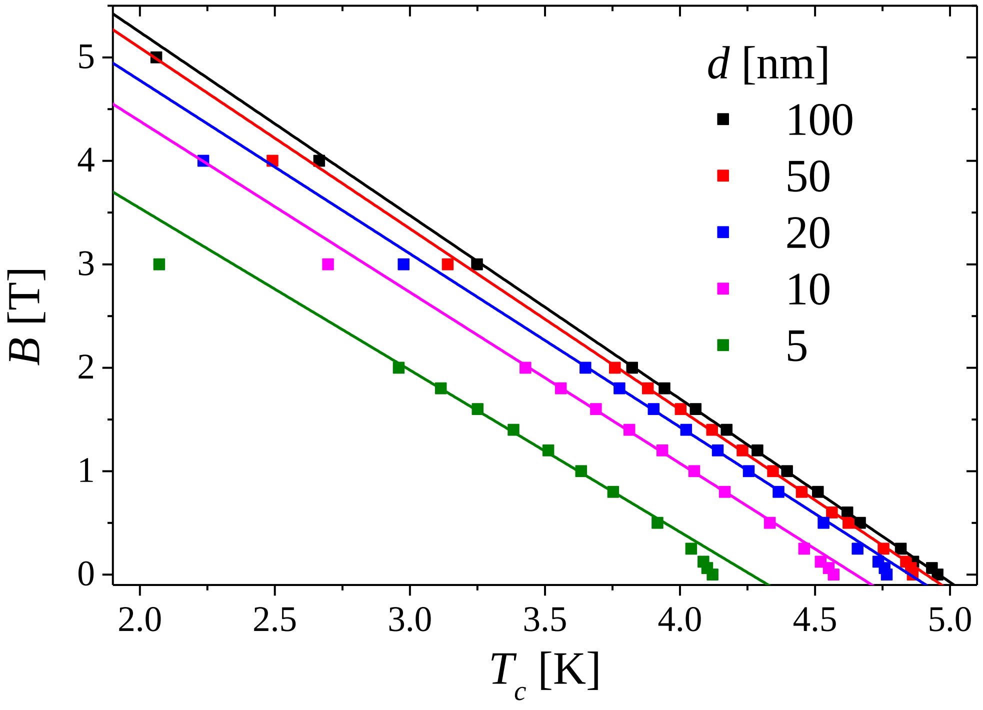

Fig. 4.3: The critical magnetic field at different temperatures for a series of 100 µm wide $W_{0.8}Si_{0.2}$ bridges. Through linear fitting of these temperature dependences, we extracted the zero-temperature critical magnetic field $B_{c2}(0)$.

4.4 Transport parameters

From the GL theory, the zero-temperature critical magnetic field $B_{c2}(0)$ is related to the GL coherence length [210] by

$$B_{c2}(0) = \frac{\Phi_0}{2\pi\xi^2(0)}, \tag{4.6}$$

where $\Phi_0 = h/2e = 2.07 \times 10^{-15}\ \mathrm{V \cdot s}$ is the magnetic-flux quantum. Here all the calculations are based on the extrapolated $B_{c2}(0)$, therefore the calculated coherence length is the Ginzburg-Landau (GL) coherence length. The GL coherence length ξ characterizes the distance over which the GL order parameter can vary without excessive energy increase. With the decrease of the films thickness, the zero-temperature GL coherence length exhibits a significant increase, as it is shown in Fig. 4.4.

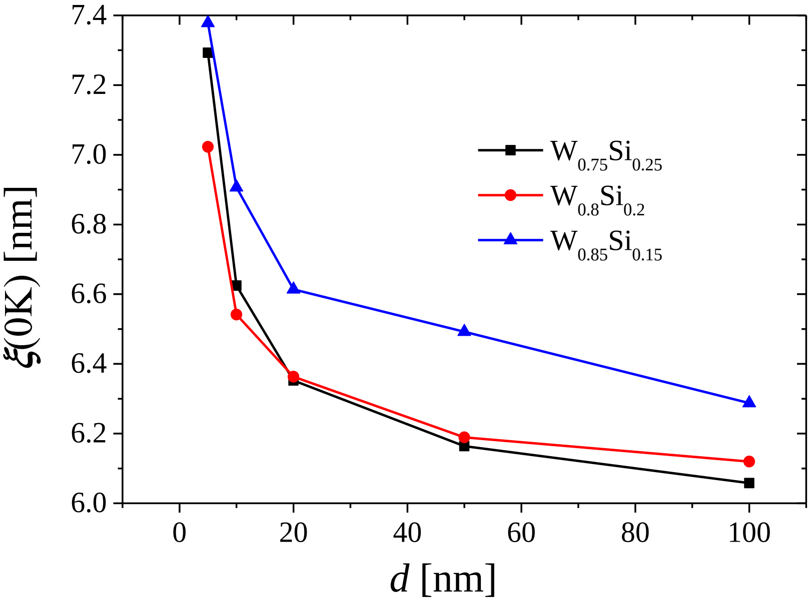

Fig. 4.4: The GL coherence length at zero temperature $\xi(0)$ as a function of film thickness.

For the highly disordered WSi, the electron mean-free paths l is relatively small and the magnetic penetration depths λ (which will be discussed later) is relatively large, which drives the WSi in the limiting case of a dirty superconductor and local electrodynamics. The diffusion constant of the normal-state electrons D_e can therefore be determined from the slope of the $T_c(B)$ curve in the vicinity of the superconducting zero field transition temperature $T_c(0)$ [208, 211, 212],

$$D_e = \frac{4k_\mathrm{B}}{\pi e}\cdot\left(-\frac{\mathrm{d}B_{c2}}{\mathrm{d}T}\right)^{-1}\Bigg|_{T\to T_\mathrm{C}(0)} = \frac{1.097}{\left(-\frac{\mathrm{d}B_{c2}}{\mathrm{d}T}\right)\Big|_{T\to T_C(0)}}\ (\mathrm{cm}^2/\mathrm{s}), \tag{4.7}$$

where k_B is the Boltzmann constant. As it is shown in Fig. 4.5, D_e increases with decreasing film thickness. For the thin films used for the SNSPDs fabrication, the D_e of WSi is around 0.75 cm^2/s, depending on the Si composition, which is nearly 25 percent higher than that of NbN. As a result, the incident photon induced normal state electrons diffuse farther than that in NbN materials, which results in a larger hotspot in WSi. This can partially explain the higher detection efficiency of WSi at low normalized bias current.

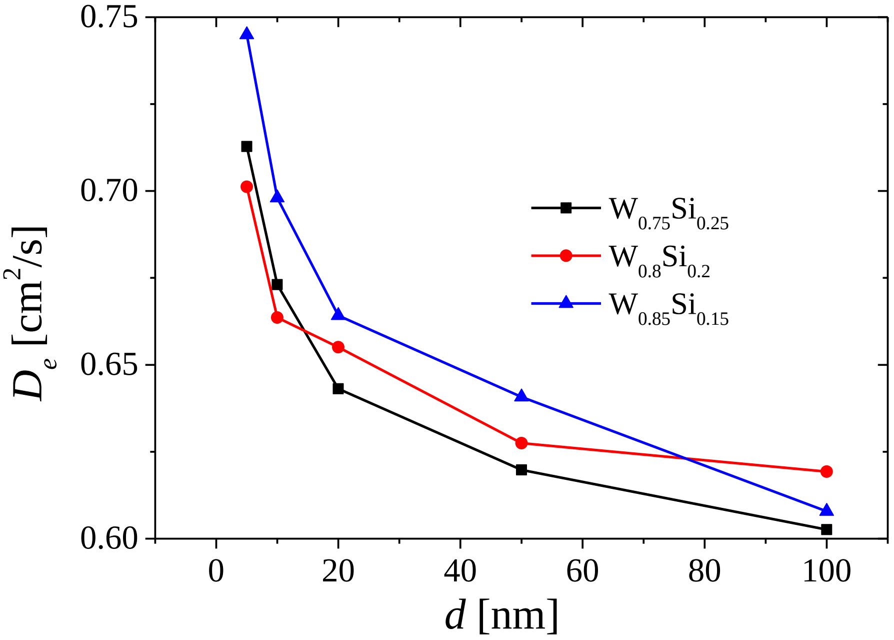

Fig. 4.5: Thickness dependence of the diffusion constant of the electrons in the normal-conducting state.

Taking the Einstein-Smoluchowski relation into consideration, the total density of states N_0 at the Fermi energy E_F in the normal conducting state can be written as [213, 214],

$$N_0 = \frac{1}{e^2\rho_n D_e}. \tag{4.8}$$

Here ρ_n is the normal state resistivity, which can be calculated from the sheet resistance at 7 K. It is interesting to note that the calculated electronic densities of states for our amorphous WSi films are one order of magnitude higher than the results for W_xSi_{1-x} of the crystalline structures ($N_0 = 3.64\times10^{46}$ $\mathrm{m}^{-3}\mathrm{J}^{-1}$ for WSi_2 and $N_0 = 1.36\times10^{46}$ $\mathrm{m}^{-3}\mathrm{J}^{-1}$ for W_5Si_3) [197, 198]. This explains the enhanced the critical temperature for amorphous W_xSi_{1-x} when x ranges from 70% to 85%.

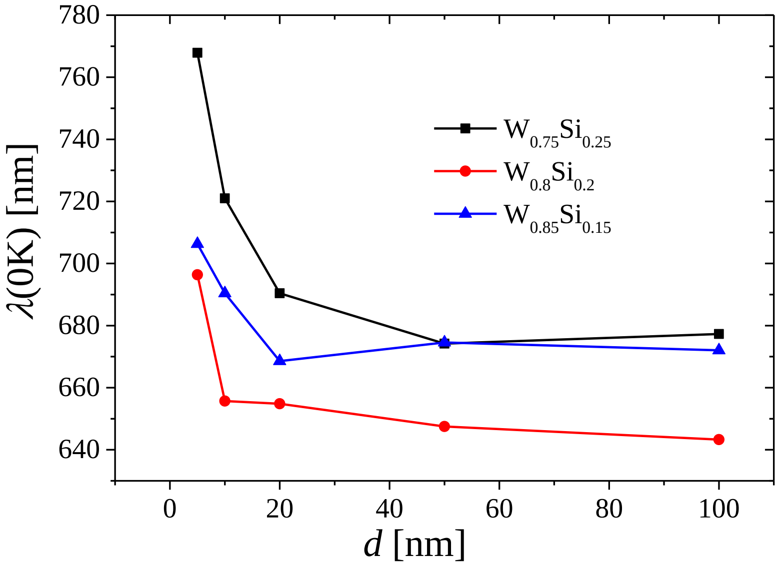

Fig. 4.6: The magnetic penetration depth $\lambda(0)$ as a function of film thickness d.

A basic characteristic of bulk superconductors below T_c is the perfect diamagnetism in low enough magnetic fields, which was found by Meissner and Ochsenfeld in 1933 [215]. However, the magnetic flux still enters near the edge of superconductors, and obeys exponential variation in space as [216],

$$B_z(x) = B_z(0)\exp(-\frac{x}{\lambda_L}). \tag{4.9}$$

Here λ_L is London magnetic penetration depth and the subscript z denotes the direction of the magnetic field. With respect to the BCS theory in dirty superconductors, the effective magnetic penetration depth λ can be expressed with the BCS coherence length ξ_0 and the electron mean-free path l [217],

$$\lambda(0) = \lambda_L(0)\sqrt{\frac{\xi_0}{l}}. \tag{4.10}$$

The BCS coherence length can be expressed by the Fermi velocity v_F and the superconducting zero temperature energy gap $\Delta(0)$ through $\xi_0 = \hbar v_F/\pi\Delta(0)$ [218]. Since we have not directly measured the values of the superconducting energy gap for W_xSi_{1-x} films, we used the BCS relation $\Delta(0) = (\pi/e^{\gamma})k_BT_c$ with γ=0.577 [218]. With the critical temperatures extracted from Fig. 4.1 (c), we can calculate the superconducting energy gaps, and obtain the magnetic penetration depths at zero temperature through

$$\lambda(0) = (\frac{\hbar\rho_n}{\pi\mu_0\Delta(0)})^{0.5}, \tag{4.11}$$

with μ_0 the vacuum permeability. The thickness dependence of $\lambda(0)$ is shown in Fig. 4.6.

A striking characteristic of thin amorphous WSi film is their large magnetic field penetration depth. $\lambda(0)$ of a 5 nm thick WSi film is more than 700 nm, which is nearly two times larger than that of NbN films.

All the calculated transport parameters presented here are listed in Table 4.1. For comparison, two groups of data for NbN and one group of data for TaN are also listed at the bottom of the same table.

Table 4.1 Material parameters of the 5 nm thick films. The material parameters from NbN and TaN SNSPDs are also listed.

Sample	d (nm)	w (μm)	R_{SN} (Ω)	$T_c(0)$ (K)	$\xi(0)$ (nm)	D_e (cm^2/s)	$N_0(0)$ ($\mathrm{m}^{-3}\mathrm{J}^{-1}$)	$\Delta(0)$ (meV)	$\lambda(0)$ (nm)
$W_{0.75}Si_{0.25}$	5	10	410	3.86	6.7	0.61	3.1×10^{47}	0.59	763
$W_{0.75}Si_{0.25}$	5	100	417	3.88	6.7	0.59	3.2×10^{47}	0.59	768
$W_{0.8}Si_{0.2}$	5	10	340	4.02	6.5	0.59	3.9×10^{47}	0.61	696
$W_{0.8}Si_{0.2}$	5	100	357	4.08	6.5	0.58	3.7×10^{47}	0.61	681
$W_{0.85}Si_{0.15}$	5	10	326	3.83	6.6	0.58	4.1×10^{47}	0.58	735
$W_{0.85}Si_{0.15}$	5	100	350	3.85	6.6	0.58	3.8×10^{47}	0.59	706
NbN[212]	6	0.053	445	12.73	4.0	0.49	3.6×10^{47}	2.30	404
NbN[87]	6	0.08	380	13.0	4.3	0.50	5.1×10^{47}	1.98	440
TaN [87]	3.9	0.126	380	9.30	5.0	0.60	4.4×10^{47}	1.24	490

In the reference [87,212], a correction of $\xi(0)$ is made since the real $B_{c2}(0)$ is smaller than the extrapolated $B_{c2}(0)$. Thus here the $\xi(0)$ from NbN and TaN are larger than the values calculated from the extrapolated $B_{c2}(0)$. With a correction factor, the $\xi(0)$ of WSi are slightly larger than the values listed above.

4.5 Influence of the transport parameters on the detection process

4.5.1 Direct photon detection by hotspot-induced current redistribution

We first consider a "hard" hotspot model, which means that we neglect all the indirect detection mechanisms, and a detection event is thought to be solely due to the physical hotspot size induced current redistribution. A hotspot is a nonequilibrium region containing broken Cooper pairs induced by incident photons. For photons in the visible and infrared wavelength range, the photon energy $h\nu$ is around 1 eV, which is nearly three orders of magnitude larger than the superconducting energy gap of the commonly used materials for the SNSPDs fabrication. The number of broken Cooper pairs can be written as

$$N = \varsigma \frac{h\nu}{\Delta(T)}, \tag{4.12}$$

where ς is the energy conversion efficiency of the absorbed photons. For commonly used superconducting materials, ς is estimated to be around 10% [87]. Immediately after the photon absorption, a small region of normal state electrons is formed, and they subsequently diffuse farther away from the absorption point. Such a diffusion process depends on the diffusion constant of the normal state electrons and their lifetime (the detailed hotspot formation process will be discussed in the next chapter). As a result, in materials with a higher normal state electron diffusion constant D_e, the resulting hotspot is larger, and they are thus more suitable for SNSPDs applications. For materials with smaller Δ, though there would be more broken Cooper pairs, the hotspot size is mainly determined by the distribution of quasiparticles.

Once such a nonequilibrium region is formed, the bias current is expelled outside the hotspot and flows within the sidewalk of the nanowire. This induces a dramatic increase of the local current density, which in turn drives the whole nanowire cross section into the normal state, and a signal pulse is created in the readout. The detection criterion for a simple hard hotspot model can be expressed as

$$j_{\mathrm{sidewalk}} = I_b \frac{1}{(w-2r_0)d} > j_{lc,dep}. \tag{4.13}$$

Here j_{sidewalk} is the current density in the sidewalk after the formation of the hotspot; r_0 is the hotspot radius; and $j_{lc,dep}$ is the local critical current density. The threshold bias current can be defined as

$$I_{th,1} = j_{lc,dep} d(w - 2r_0). \tag{4.14}$$

However, this definition is based on the assumption that the hotspot is located in the center of the nanowire. If the photon is absorbed near the edge, the hotspot size and the current redistribution will be different. Taking the geometry effects into consideration, the threshold bias current can be modified as

$$I_{th,2} = j_{lc,dep} d(w - r_0), \tag{4.15}$$

which means that even half of a normal hotspot is still able to drive the residual nanowire cross section into normal state. This demonstrates that, if the hotspot size is fixed, the only way to improve the detection efficiency is to increase the bias current. However, the maximum applicable bias current, which is commonly defined as I_{ce} or j_{ce}, is limited due to (a) constrictions of the nanowire; (b) film thickness non-uniformity; and (c) imhomogeneous films quality, namely the local defects inside the nanowire. As a result, the experimental critical current I_{ce} is limited by the weakest part of nanowire, which is expected to be around 60% of $I_{lc,dep}$ in narrow NbN nanowires [220, 221]. Therefore the closer I_{ce} approaches to $I_{lc,dep}$, the better detection performance can be expected. For a 5 nm thick WSi film, the GL coherence length $\xi(0)$ is around 6.5 nm, as compared to $\xi(0)$~4 nm of NbN. WSi SNSPDs can therefore be more robust against the defects and constrictions within the nanowire. As a result, I_b can be biased much closer to $j_{lc,dep}$, and the saturation regime of SDE vs. I_b curve is expected to be much larger.

4.5.2 Vortex assisted photon detection

Once the hotspot size and the bias current are not large enough to drive the whole nanowire cross section into normal state, assisted detection mechanisms need to be considered [222-229]. These mechanisms include phase slip events, thermally activated vortex-antivortex pairs, and vortices crossing nanowire. Here we do not consider the phase slip scenario since only when the cross section of nanowire is of the order of ξ^2, phase slip events become relevant. The energy barrier for the nucleation of phase slips in a nanowire belt is too large to be of importance because the belt volume $\sim d\xi w$ is large. As a result, the quantum phase slips and thermally activated phase slips caused dissipation are important only in the 1D limit. In current-carrying strips ($w \gg \xi$), 2π-phase changes along the strip appear with an extremely low probability [227].

We firstly discuss the vortex crossing case, namely the spontaneous nucleation of a single vortex near the edge of the nanowire and its motion to the opposite edge. For low energy photons and a low bias current scenario, a cloud of quasiparticles with energies above the superconducting gap is created due to the photon absorption, which grows in the number of quasiparticles and in size due to avalanche processes and diffusion [226,227,231,232]. However, within this quasiparticle cloud, the bias current is not totally interrupted. In the superconducting nanowire, the hotspot is able to cover the entire width w of nanowire when it reaches its maximal size, and inside the hotspot, the quasiparticles suppress the superconducting order parameter, but their density is not sufficient to convert the whole hot belt into the normal state. The superconducting condensation energy inside the hotspot and vortex-entry energy is significantly lowered accordingly. Due to the decrease of the energy barrier, a vortex appears at distances smaller than $x_0{\sim}\xi$ near the edge. Then the vortex moves from one side to the other side because of the Lorentz force provided by the bias current, and an energy amount of $\Phi_0 I_b/c$ is dissipated. Consequently, a vortex assisted photon detection event is formed in the readout [227].

In a current biased superconducting nanowire, the vortex energy can be written as [212,226,227,233],

$$E_V(X_v) = \mu^2\epsilon_0[\ln\left(\frac{2w}{\pi\xi}\sin X_v\right) - \frac{I}{\mu^2 I_0}X_v]. \tag{4.16}$$

Here $X_v = \pi x/w$ is a normalized coordinate in units of π/w; μ^2 denotes the amplitude of the order parameter; $I_0 = \frac{c\Phi_0}{8\pi\Lambda}$ is a characteristic current and Λ is the Pearl length [234]. ϵ_0 is the characteristic energy of vortex in thin films, which has the form [227]

$$\epsilon_0 = \frac{\Phi_0^2}{8\pi^2\Lambda}. \tag{4.17}$$

Finally, by taking the first order derivative $\frac{dE(X_v)}{dX_v} = 0$, the vortex entry energy barrier (the maximum vortex energy) is given by

$$\frac{E_V}{\mu^2\epsilon_0} = -\frac{1}{2}\ln[\frac{\pi^2\xi^2}{4w^2}\left(1 + \frac{I^2}{\mu^4 I_0^2}\right) - \frac{I}{\mu^2 I_0}\arctan\frac{\mu^2 I_0}{I}]. \tag{4.18}$$

For WSi, the magnetic penetration depth is nearly two times larger than that of NbN. As a result, the vortex energy barrier is around 25% of NbN with the same wire structures. Though the photon energy and bias current are not sufficient and the number of broken Cooper pairs is not sufficient to suppress the superconductivity within the nanowire completely, the vortices crossing the nanowire provide additional energy, which in turn improves the detection performance when compared to the NbN based detectors. On the other hand, the vortices also play an important role in the dark count event. In this case, the WSi based devices are expected to have higher dark count rates than NbN based detectors at the same normalized temperature T/T_c, reduced bias current I_b/I_c, and with the same device geometry.

With respect to the contribution from a vortex-antivortex scenario, in the high bias current range, a vortex-antivortex pair can be thermally excited by thermal fluctuations, which consists of two single vortices with the respective supercurrents circulating in opposite directions. Due to the Lorentz force from the bias current, this pair is prone to dissociate. The energy of a vortex-antivortex pair can be written as [227,233],

$$\frac{E_{VAP}}{\mu^2\epsilon_0} = \ln\left[\frac{4w^2}{\pi^2\xi^2}\sin X_1 \sin X_2 \frac{\cosh Y - \cos(X_1 - X_2)}{\cosh Y - \cos(X_1 + X_2)}\right]. \tag{4.19}$$

Here the vortex is assumed to be located at $(X_1, 0)$, and the antivortex is assumed to be located at (X_2, Y). With the increase of separation Y, the total energy increases and the lowest energy can be derived for $Y = 0$ [227]

$$\frac{E_{VAP}}{\mu^2\epsilon_0} = \ln\left[\frac{4w^2}{\pi^2\xi^2}\sin X_1 \sin X_2 \frac{\sin^2[(X_1 - X_2)/2]}{\sin^2[(X_1 + X_2)/2]}\right]. \tag{4.20}$$

To further simplify this expression, by assuming that these two vortices have a distance of $2b$ and at $b = \arctan\frac{2\mu^2 I_0}{I}$, the vortex-antivortex pair energy reaches the minimum [227]

$$\frac{E_{VAP}}{\mu^2\epsilon_0} = -\ln\left[\frac{\pi^2\xi^2}{w^2}\left(1 + \frac{I^2}{4\mu^4 I_0^2}\right) - \frac{I}{\mu^2 I_0}\arctan\frac{2\mu^2 I_0}{I}\right]. \tag{4.21}$$

Comparing with the single vortex crossing scenario, this energy barrier is twice larger than that needed for a single vortex crossing [227], and we will therefore not discuss the vortex-antivortex scenario any further.

5 Time constant measurements

5.1 Motivation for understanding the time constants

In order to understand the detailed detection processes and mechanisms in SNSPDs, we first consider how an incident photon is absorbed and how the photon energy is subsequently dissipated. The incident photon is firstly absorbed in the nanowire by an electron. This highly excited electron continuously loses its energy by inelastic scattering, and thermalizes with a time scale τ_i, thereby breaking Cooper pairs and creating quasiparticles within the nanowire. The growth of the quasiparticle number is controlled by the inelastic electron scattering rate $1/\tau_i$. While relaxing to low energy, the excited electron moves away from the site where the photon was absorbed. This thermalization (or relaxation) process can be simplified as a diffusion process with a diffusivity D_e that gives the probability to find the hot electron at the time t after the photon is absorbed at a distance r from the absorption point. Simultaneously, the created quasiparticles diffuse outside this relaxation area and recombine into Cooper pairs. In this process, the dynamics is dominated by the quasiparticle lifetime τ_r. After τ_r, the superconductivity is recovered in the hotspot, and the detector is ready for detecting the next photon. Therefore, the thermalization time τ_i of the highly excited electron and the quasiparticle lifetime τ_r are crucial for the quasiparticle dynamics and the detection mechanism in SNSPDs [104, 226].

The temperature dependence of τ_i is determined by the magnetoresistance measurement at different temperatures. With respect to the measurement of τ_r, it is directly measured from a time-resolving fast photon response experiment.

5.2 Dephasing time

In disordered thin films, the long inelastic lifetime of conduction electrons yields quantum interferences in a spatially extended region, which is generally called “weak localization” [235-242]. The localization effect can be directly probed by transport measurements in a magnetic field [243-245]. Magnetoconductivity measurements in the weakly localized regime yield valuable information on an intrinsic time scale of the system, which provides a way to determine the electron dephasing time τ_{ϕ}, i.e. the inelastic scattering time τ_i, which plays a significant role in quantum-interference devices [246-260]. The dephasing time τ_{ϕ} describes the electron lifetime of inelastic scattering in the equilibrium state, and it is different from the thermalization time τ_i of the hot electron in the nonequilibrium state, since the latter is energy dependent. However, in a numerical simulation of detection dynamics of SNSPDs, it was found that the most optimal thermalization time of the hot electron in NbN is rather close to the experimental value from the magnetotransport measurement [226]. Moreover, for photons in the visible and near infrared wavelength range, the photon energy $h\nu$ is around 1 eV and the thermalization process is relatively fast, and we will therefore ignore the difference between τ_{ϕ} and τ_i.

In the thin disordered superconducting films, the magnetoconductivity can be well described by the combination of the weak localization effect (WL) and superconducting fluctuations. Namely, in the vicinity of T_c, we must include the contributions from the Cooper pair channel into our analyses.

5.2.1 Weak localization effect

The magnetoresistance is in most cases dominated by the weak localization effect, which is essentially caused by the quantum-interference of the conduction electrons on the defects of the system [236,268]. At low temperatures, conduction electrons have two different lifetimes, the elastic lifetime τ_e (lifetime of electrons in an eigenstate of momentum, which is assumed to be the smallest scattering time and describes a reversible process) and the inelastic lifetime τ_i (lifetime of electrons in an eigenstate of energy, which is irreversible in nature and leads to either the loss of phase coherence or the energy relaxation). A coherent superposition of the scattered electron wave, which results in back-scattering of the electron wave and lasting as long as its coherence is not destroyed, leads to the magnetoresistance anomalies. As a result, the conductivity in the 2D case due to the basic weak localization effect for weakly spin-orbit coupling can be written as [236]

$$\sigma^{\mathrm{WL}} = \sigma_0 - \frac{e^2}{2\pi^2\hbar}[\psi\left(\frac{1}{2}+\frac{1}{\omega_H\tau_e}\right) - \psi\left(\frac{1}{2}+\frac{1}{\omega_H\tau_i}\right)], \tag{5.1}$$

where $\omega_H = 4eDH/\hbar c$ is the cyclotron frequency in a disordered conductor (D is the diffusion constant) and τ_e is the elastic scattering time. The first digamma function $\psi\left(\frac{1}{2}+\frac{1}{\omega_H\tau_e}\right)$ can be approximated by $\ln\frac{1}{\omega_H\tau_e}$.

The above expressions are still not able to give a quantitative description of the anomalous magnetoresistance in materials because it only discusses the scattering processes where the spin of the electron is conserved. If we also consider the spin-orbit scattering and magnetic scattering, Eq. 5.1 is no longer sufficient for describing the anomalous magnetoresistance. The influence of spin-orbit coupling on weak localization causes an increase of the conductance with decreasing temperature, and can even change the weak localization into weak antilocalization [269-271]. Finally, the conductance per sample square including the spin-orbit scattering and magnetic impurities scattering (neglecting the Zeeman effect in the perpendicular magnetic field) can be written as [244,271-273],

$$\sigma^{\mathrm{WL}}(H,T) = \sigma_0 - \frac{e^2}{2\pi^2\hbar}[\psi\left(\frac{1}{2}+\frac{1}{\omega_H\tau_1}\right) - \psi\left(\frac{1}{2}+\frac{1}{\omega_H\tau_2}\right) + \frac{1}{2}\psi\left(\frac{1}{2}+\frac{1}{\omega_H\tau_3}\right) - \frac{1}{2}\psi\left(\frac{1}{2}+\frac{1}{\omega_H\tau_4}\right)], \tag{5.2}$$

where:

$$\frac{1}{\tau_1} = \frac{1}{\tau_e} + \frac{1}{\tau_{so}} + \frac{1}{\tau_s} = \frac{1}{\tau_e} + \frac{1}{\tau_{so}},$$

$$\frac{1}{\tau_2} = \frac{4}{3}\frac{1}{\tau_{so}} + \frac{2}{3}\frac{1}{\tau_s} + \frac{1}{\tau_i} = \frac{4}{3}\frac{1}{\tau_{so}} + \frac{1}{\tau_i},$$

$$\frac{1}{\tau_3} = 2\frac{1}{\tau_s} + \frac{1}{\tau_i} = \frac{1}{\tau_i},$$

$$\frac{1}{\tau_4} = \frac{1}{\tau_2}.$$

and the characteristic time τ_{so} is spin-orbit interaction time. The parameter τ_s is the magnetic scattering time, and $1/\tau_s$ equals zero in our case because WSi is not a magnetic material with magnetic impurities. Therefore Eq. 5.2 can be simplified as,

$$\sigma^{\mathrm{WL}}(H,T) = \sigma_0 + \frac{e^2}{2\pi^2\hbar}\{\frac{3}{2}\psi\left[\frac{1}{2}+\frac{1}{\omega_H}\left(\frac{4}{3}\frac{1}{\tau_{so}}+\frac{1}{\tau_i}\right)\right] - \frac{1}{2}\psi\left(\frac{1}{2}+\frac{1}{\omega_H\tau_i}\right) - \psi\left(\frac{1}{2}+\frac{1}{\omega_H\tau_1}\right)\}. \qquad (5.3)$$

In the zero field limit, $H \to 0$, $\omega_H \to 0$, we obtain

$$\sigma^{\mathrm{WL}}(0,T) = \sigma_0 + \frac{e^2}{2\pi^2\hbar}\left[\frac{3}{2}\ln\frac{1}{\omega_H}\left(\frac{4}{3}\frac{1}{\tau_{so}}+\frac{1}{\tau_i}\right) - \frac{1}{2}\ln\frac{1}{\omega_H\tau_i} - \ln\frac{1}{\omega_H\tau_1}\right]. \qquad (5.4)$$

In the absence of spin-orbit and magnetic scattering, Eq. 5.4 results in a well-known localization logarithmic temperature dependence of the conductivity,

$$\sigma^{\mathrm{WL}}(0,T) = \sigma_0 + \frac{e^2}{2\pi^2\hbar}\ln\frac{\tau_1}{\tau_i}. \qquad (5.5)$$

On the other hand, in case of very strong spin-orbit scattering, Eq. 5.4 results in a weak antilocalization (WAL) logarithmic temperature dependence of the conductivity,

$$\sigma^{\mathrm{WL}}(0,T) = \sigma_0 - \frac{1}{2}\frac{e^2}{2\pi^2\hbar}\ln\frac{\tau_{so}}{\tau_i}. \qquad (5.6)$$

Finally, the excess magnetoconductance per square sample becomes

$$\delta\sigma^{\mathrm{WL}}(H,T) = \frac{e^2}{2\pi^2\hbar}\{\frac{3}{2}Y\left[\omega_H\left(\frac{4}{3}\frac{1}{\tau_{so}}+\frac{1}{\tau_i}\right)^{-1}\right] - \frac{1}{2}Y(\omega_H\tau_i) - Y(\omega_H\tau_1)\}. \qquad (5.7)$$

The universal function $Y(x)$ is in the 2D case is

$$Y(x) = \ln x + \psi\left(\frac{1}{2}+\frac{1}{x}\right). \qquad (5.8)$$

In the limiting cases, $Y(x) \approx x^2/24$ for $x \ll 1$ and for $x \gg 1$ $Y(x) \approx \ln x - 2\ln 2 - \gamma_E + \pi^2/2x$, with $\gamma_E = 0.5772$ is the Euler constant.

In the weak spin-orbit scattering case, $\tau_{so} \to \infty$, Eq. 5.7 can be simplified to

$$\delta\sigma^{\mathrm{WL}}(H,T) = \frac{e^2}{2\pi^2\hbar}\{\psi(\frac{1}{2}+\frac{1}{\omega_H\tau_i}) - \psi\left(\frac{1}{2}+\frac{1}{\omega_H\tau_1}\right) - \ln\tau_1/\tau_i\}. \qquad (5.9)$$

Moreover, since τ_e is much smaller than any other time scales here [25], the excess conductance can therefore be simplified to

$$\delta\sigma^{\mathrm{WL}}(H,T)=\frac{e^2}{2\pi^2\hbar}\{\frac{3}{2}Y\left[\frac{1}{2}+\frac{1}{\omega_H}\left(\frac{4}{3}\frac{1}{\tau_{so}}+\frac{1}{\tau_i}\right)\right]-\frac{1}{2}Y\left(\frac{1}{2}+\frac{1}{\omega_H\tau_i}\right)\}. \tag{5.10}$$

5.2.2 Maki-Thompson (MT) fluctuation

With decreasing temperature, the superconducting fluctuations appear in the films, resulting in the paraconductivity from the short-lived Cooper pairs [205,207,274,275]. Therefore the total magnetoresistance in this temperature range should also include the superconducting fluctuation, *i.e.*, the interaction corrections in the Cooper channel. It was shown that at finite temperatures there are three important fluctuation corrections to the conductivity: the Maki-Thompson (MT) correction $\delta\sigma^{\mathrm{MT}}$, the Aslamozov-Larkin (AL) correction $\delta\sigma^{\mathrm{AL}}$, and the density of states correction (DOS) $\delta\sigma^{\mathrm{DOS}}$.

In highly disordered superconductors, the MT fluctuation mechanism, due to the coherent scattering of electrons forming Cooper pairs at impurities, describes single-particle quantum interference at impurities in the presence of the superconducting fluctuations [207,276,277]. Maki introduced an indirect contribution of fluctuations to the conductance of an extremely dirty type II superconducting film in a field H slightly above H_{c2} [264]. Later, Thompson removed an unphysical divergence from Maki's theory by introducing a nonzero pair-breaking parameter δ, and recalculated the dynamic response of superconductors to electric fields, which resulted in significantly different results from previous calculations [207]. Then δ was found to be related to the inelastic scattering process, and Larkin introduced the inelastic process into the MT fluctuations [265]. In the 2D case, the magnetoconductivity from the MT correction can be written as [243,277-280]

$$\sigma^{\mathrm{MT}}=\frac{e^2}{\pi\hbar^2}\frac{k_{\mathrm{B}}T\tau_{\mathrm{GL}}}{1-\tau_{\mathrm{GL}}/\tau_i}[\psi\left(\frac{1}{2}+\frac{1}{\omega_H\tau_{\mathrm{GL}}}\right)-\psi\left(\frac{1}{2}+\frac{1}{\omega_H\tau_i}\right)]. \tag{5.11}$$

Here the τ_{GL} is the Ginzburg-Landau time ($\tau_{\mathrm{GL}}^{-1}=\frac{8k_{\mathrm{B}}T}{\pi\hbar}\ln\frac{T}{T_c}$). In the zero field limit, this reduces to the well-known result at the zero field,

$$\sigma^{\mathrm{MT}}(H=0)=\frac{e^2}{\pi\hbar^2}\frac{k_{\mathrm{B}}T\tau_{\mathrm{GL}}}{1-\tau_{\mathrm{GL}}/\tau_i}\ln\frac{\tau_i}{\tau_{\mathrm{GL}}}. \tag{5.12}$$

By taking τ_{GL}^{-1} into the expression, we can get

$$\sigma^{\mathrm{MT}}(H=0)=\frac{e^2}{8\hbar}\frac{\tau_i}{\tau_i-\tau_{\mathrm{GL}}}\ln\frac{\tau_i}{\tau_{\mathrm{GL}}}(\ln\frac{T}{T_c})^{-1}. \tag{5.13}$$

Therefore the excess conductivity due to the MT contribution can be derived as

$$\delta\sigma^{\mathrm{MT}}=\frac{e^2}{2\pi^2\hbar}\{\frac{\pi^2}{4}\frac{1}{\ln\frac{T}{T_c}(1-\tau_{\mathrm{GL}}/\tau_i)}\}[Y(\omega_H\tau_{\mathrm{GL}})-Y(\omega_H\tau_i)]. \tag{5.14}$$

When the temperature is relatively high, namely $\ln T/T_c \gg 1$, τ_{GL} is much smaller than τ_i. Thus $\psi\left(\frac{1}{2}+\frac{1}{\omega_H\tau_{\mathrm{GL}}}\right)$ can be approximated as $\ln\frac{1}{\omega_H\tau_{\mathrm{GL}}}$. As a result, Eq. 5.14 can be simplified to

$$\delta\sigma^{\mathrm{MT}}=-\frac{e^2}{\pi\hbar^2}\frac{k_{\mathrm{B}}T\tau_{\mathrm{GL}}}{1-\tau_{\mathrm{GL}}/\tau_i}Y(\omega_H\tau_i). \tag{5.15}$$

This simplification, however, is only valid in a relatively high temperature range above T_c. In the vicinity of T_c, $Y_2(\omega_H\tau_{\mathrm{GL}})$ cannot be neglected.

5.2.3 Aslamazov-Larkin (AL) fluctuation

Aslamazov and Larkin were the first to calculate the fluctuation conductance just above the superconducting transition [263]. Later, the influence of a magnetic field was included, and in the 2D case, the AL contribution to the magnetoconductivity can be written as [243,281-283]

$$\sigma^{\mathrm{AL}}=\frac{2e^2}{\pi\hbar}(\frac{k_{\mathrm{B}}T\tau_{\mathrm{GL}}}{\hbar})\mathcal{H}_2(\omega_H\tau_{\mathrm{GL}}), \tag{5.16}$$

$$\mathcal{H}_2(x)=\frac{1}{x}\{1-\frac{2}{x}[\psi\left(1+\frac{1}{x}\right)-\psi\left(\frac{1}{2}+\frac{1}{x}\right)]\}. \tag{5.17}$$

In the zero field limit, $\mathcal{H}_2(x\rightarrow 0)\approx\frac{1}{4}$, we recovers from the above equation to the famous AL fluctuation conductivity [263]

$$\sigma^{\mathrm{AL}}(H=0)=\frac{e^2}{16\hbar}\frac{1}{\ln T/T_c}. \tag{5.18}$$

Therefore the excess conductivity due to AL contribution can be derived as:

$$\delta\sigma^{\mathrm{AL}}=\frac{2e^2}{\pi\hbar}\left(\frac{k_{\mathrm{B}}T\tau_{\mathrm{GL}}}{\hbar}\right)[\mathcal{H}_2(\omega_H\tau_{\mathrm{GL}})-\frac{1}{4}]. \tag{5.19}$$

5.2.4 Density of states (DOS) correction

The formation of short lifetime Cooper pairs results in a change in the number of electrons near the Fermi level. Such an indirect effect from the quasiparticles is referred as the DOS contribution [284]. With respect to this DOS contribution, Glatz *et al.* recently recalculated it from the change of the single-particle density of states comprehensively. In low magnetic fields near T_c, the DOS contribution to the conductance can be written as [285,286]

$$\sigma^{\mathrm{DOS}}(H,T) = \frac{14\zeta(3)e^2}{\pi^4\hbar}[\ln\left(\omega_H\tau_{\mathrm{GL}}\ln\frac{T}{T_c}\right) + \psi\left(\frac{1}{2}+\frac{1}{\omega_H\tau_{\mathrm{GL}}}\right)], \tag{5.20}$$

where ζ is the Riemann zeta function, with $\zeta(3) = 1.202$. In the zero field limit, we have

$$\sigma^{\mathrm{DOS}}(H=0) = \frac{14\zeta(3)e^2}{\pi^4\hbar}\ln(\ln T/T_c). \tag{5.21}$$

Therefore the excess magnetoconductance due to the DOS contribution can be written as

$$\delta\sigma^{\mathrm{DOS}}(H,T) = \frac{e^2}{2\pi^2\hbar}\frac{28\zeta(3)}{\pi^2}Y(\omega_H\tau_{\mathrm{GL}}). \tag{5.22}$$

Besides the AL fluctuations, MT fluctuations, and DOS corrections, the renormalization of diffusion constant of normal state electrons due to quantum fluctuations needs to be considered. This fluctuation mechanism of renormalization of the single-particle diffusion coefficient can be safely neglected in the intermediate magnetic field range above T_c. In the relatively high temperature range, both AL fluctuation and DOS contribution are dominated by the MT fluctuation. However, as the temperature decreases, τ_{GL} gradually increases and exceeds τ_i near T_c. In this case, the magnetotransport will be dominated by the AL fluctuation and DOS contributions. It should also be noted that the 2D expressions discussed above will be no longer applicable in the ultrahigh magnetic field range since the characteristic length scale $l_B = \sqrt{\hbar/2eB}$ is lower than the film thickness d [273].

5.3 Measurement of τ_i

5.3.1 Magnetoresistance of WSi

Figure 5.1 shows the magnetoresistance $R_{\mathrm{S}}(B)$ at different temperatures. In the relatively high temperature range, the superconducting fluctuations are not strong, and the resulting excess conductivity is relatively small. In the low temperature range near T_c, the strong superconducting fluctuations induce large variations of sheet resistance, and the resulting excess conductance is huge. In this range, it is necessary to add the DOS correction to the fluctuation conductivity.

It is interesting to note that a crossing point appears in the $R_{\mathrm{S}}(B,T)$ plane, which hints to a superconductor to insulator transition at finite temperature. More details concerning this superconductor to insulator transition in WSi will be discussed in chapter 7.

The excess magnetoconductance is defined as,

$$\delta\sigma(T)=\frac{1}{R_{\mathrm{S}}(B,T)}-\frac{1}{R_{\mathrm{SN}}(T)}=\frac{R_{\mathrm{SN}}(T)-R_{\mathrm{S}}(B,T)}{R_{\mathrm{S}}(B,T)R_{\mathrm{SN}}(T)}. \tag{5.23}$$

By fitting the excess magnetoconductance data, we are able to determine the diphasing time of the thin films.

5.3.2 Fittings of the excess magnetoconductivity

In the relatively high temperature range, for instance, at $T=20$ K, τ_{GL} is 0.09 ps and 0.08 ps for the 5 nm and 4 nm thick films, respectively. In this temperature range, the diphasing time τ_i is nearly two orders of magnitude higher than τ_{GL}. As a result, in the high temperature range, $\delta\sigma(T)$ is dominated by the MT fluctuation and the WL effect. Comparing MT fluctuations and AL fluctuations, for example at $1/\omega_H\sim\tau_{\mathrm{GL}}$, the MT interaction dominates against the AL fluctuation mechanism by a factor of $\ln(\tau_i/\tau_{\mathrm{GL}})\sim 5$. As a result, the MT fluctuations in the high magnetic field range can be simplified as $\delta\sigma^{\mathrm{MT}}\propto\omega_H^2$, and $\delta\sigma$ decreases monotonically with ω_H, namely the magnetic field. Figure 5.2 shows the excess magnetoconductance for the 5 and 4 nm thick WSi films in the relatively high temperature range. The excess magnetoconductance increases with decreasing temperature and is negative in the considered magnetic field range. Above 6 K, the excess magnetoconductance can be well described by the MT fluctuation and WL effect over the whole magnetic field range.

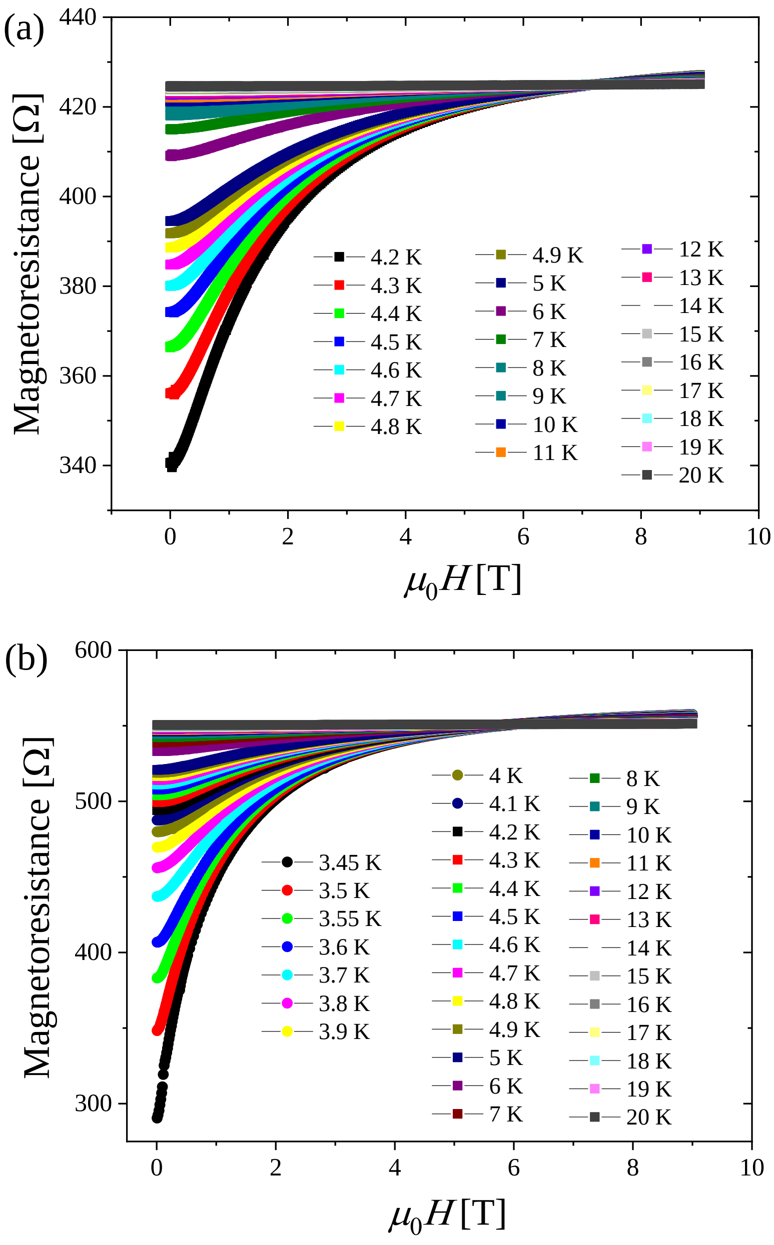

Fig. 5.1: Magnetoresistance at different temperatures for the 5 nm thick film (a) and 4 nm thick film (b).

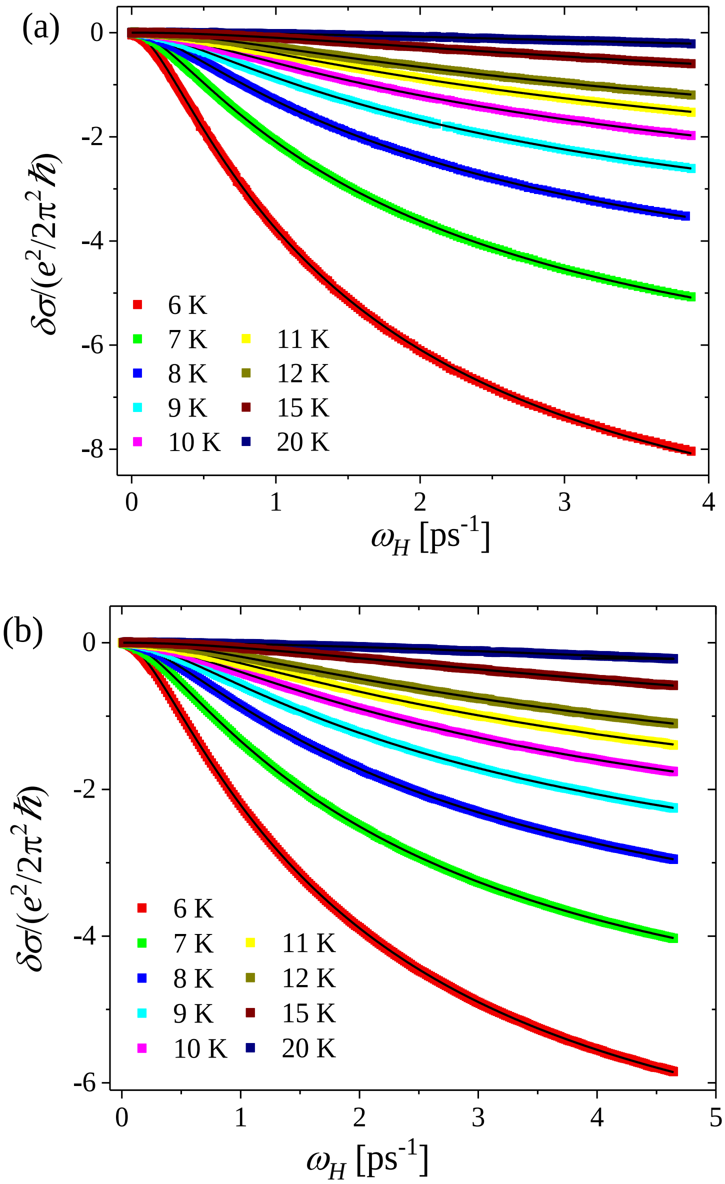

Fig. 5.2: The best fits to the measured the excess magnetoconductance based on the WL effect and the MT fluctuations for the 5 nm (a) and 4 nm (b) WSi film (solid black lines).

In the low temperature range near T_c, τ_{GL} is around 4.5 ps for the 5 nm thick film at 4.5 K, which is comparable with τ_i. With decreasing temperature, both τ_{GL} and τ_i increase and τ_{GL} becomes even larger than τ_i. In this case, the WL effect and MT fluctuations alone fail to give a satisfactory fit to the data in the low temperature range near T_c, and the excess magnetoconductance is dominated by the AL fluctuations and the DOS corrections. Therefore, the excess magnetoconductance has been fitted with the WL effect and including all the superconducting fluctuation contributions, as it is shown in Fig. 5.3. In the high magnetic field range, $\omega_H^{-1} \lesssim \tau_{\mathrm{GL}}$, $\delta\sigma$ is found to be independent of the magnetic field. A saturation of $\delta\sigma$

therefore appears in the high magnetic field range, as it is shown in Fig. 5.3. These fits yield maximum inelastic time scales τ_i of 6.6 ps for the 4 nm thick film at 4.5 K and 7.6 ps for the 5 nm thick film at 5 K.

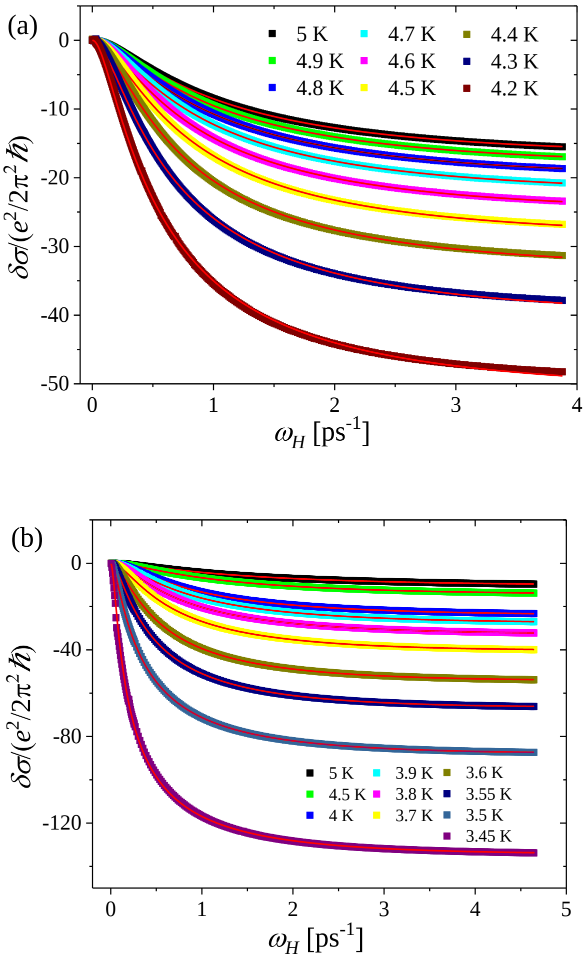

Fig. 5.3: The best fit of the excess magnetoconductance based on the WL effect, MT fluctuations, AL fluctuations, and the DOS contributions for 5 nm (a) and 4 nm (b) WSi film.

5.3.3 Interpretation of τ_i

Above T_c, the dephasing process of conducting electrons can mainly be interpreted in terms of electron-electron interaction (e-e), electron-phonon interaction (e-ph) and electron-Cooper pair interaction (or electron-superconducting fluctuation interaction, e-fl). In amorphous WSi films, the thermal diffusion length $L_T = (\hbar D/k_\mathrm{B}T)^{1/2}$ is larger than the film thickness d [287]. The e-e scattering rate can therefore be written as [288-290]

$$\tau_{e-e}^{-1} = \frac{e^2 R_\mathrm{S}}{2\pi^2\hbar} \cdot k_\mathrm{B}T \cdot \ln\frac{\pi\hbar}{e^2 R_\mathrm{S}}. \tag{5.24}$$

With respect to the e-ph interactions for WSi, we have obtained that $\tau_{e-ph}^{-1} \propto T^3$ [104]. Moreover, at temperature T close to T_c, the scattering process is dominated by superconducting fluctuations, and τ_{e-fl}^{-1} is given by [278,291]

$$\tau_{e-fl}^{-1} = \frac{e^2 R_\mathrm{S}}{2\pi^2 \hbar} \cdot k_\mathrm{B} T \cdot \frac{2\ln 2}{\ln\frac{T}{T_c} + G}, \; G = \frac{4\ln 2}{\sqrt{\ln^2(\frac{\pi\hbar}{e^2 R_\mathrm{S}}) + 128\hbar/e^2 R_\mathrm{S}} - \ln^2(\frac{\pi\hbar}{e^2 R_\mathrm{S}})}. \tag{5.25}$$

Figure 5.4 shows the best fit including the scattering mechanisms discussed above, of the total inelastic interaction time τ_i. The temperature dependence of τ_{e-ph} for the 5 nm thick film is found to be $\tau_{e-ph} = \alpha \cdot T^{-3}$ with $\alpha = 5.5 \times 10^3$ ps · K^3, and a τ_{e-ph} = 93 ps at T_c and 86 ps at 4 K. For the 4 nm thick film we find $\alpha = 4.8 \times 10^3$ ps · K^3, which corresponds to τ_{e-ph} = 118 ps at T_c and 75 ps at 4 K. Sidorova *et al.* recently also studied the electron-phonon relaxation time in a 3.4 nm thick WSi film using an amplitude-modulated absorption of sub-THz radiation (AMAR) method, and τ_{e-ph} was estimated to be in the range of 100-200 ps at 3.4 K [292], which coincides well with our result from the magnetoresistance method. With respect to the contribution from the electron-electron interaction, a temperature dependence $\tau_{e-e} = \beta/T$ with $\beta = 95$ ps · K was determined for the 5 nm film from the fit in Fig. 3, which results in a τ_{e-e} of 24.4 ps at T_c. For the 4 nm thick film, we obtained $\beta = 60$ ps · K, and τ_{e-e} is found to be 17.4 ps at T_c.

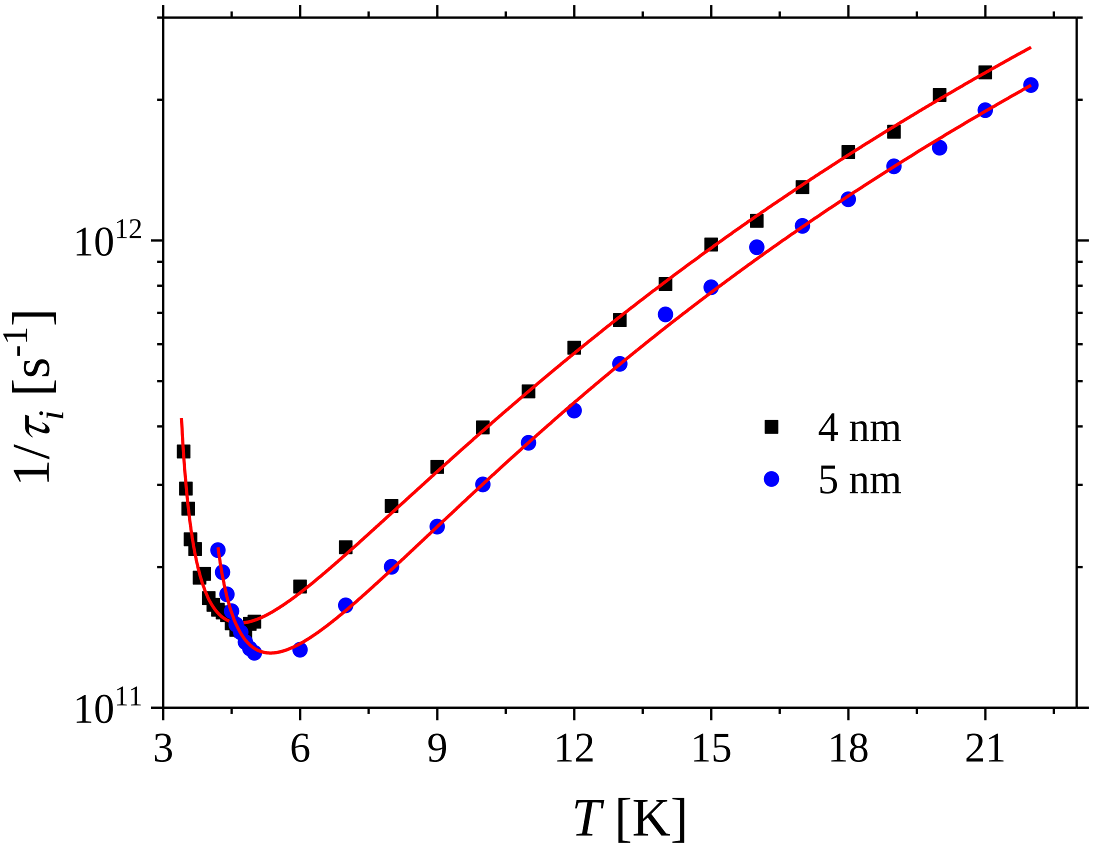

Fig. 5.4: The best fits of the inelastic scattering rate, based on e-e interaction, e-ph interaction and e-fl interaction.

5.4 Fast optical response of a WSi microbridge

Figure 5.5 shows the current-voltage (*IV*) curve of a $W_{0.85}Si_{0.15}$ bridge at 3.2 K (shown in Fig. 3.7(b)). From the slope of the linear regime in the superconducting state, we calculate the series resistance of the bias circuit to be 14 Ω. The critical current is defined as the maximum applicable superconducting bias current on the bridge, which gives a I_c of 119 μA.

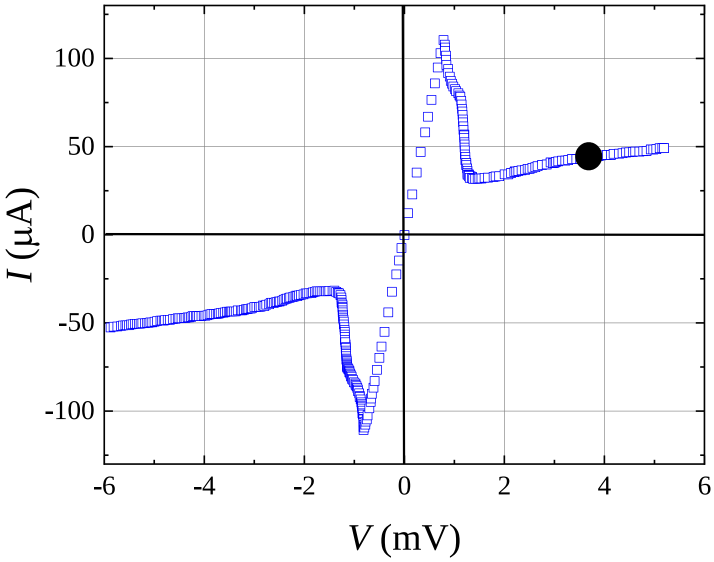

Fig. 5.5: The *I*-*V* curve of the $W_{0.85}Si_{0.15}$ microbridge measured at T = 3.2 K. The critical current for the device is around 119 μA and the series resistance of the bias circuit is 14 Ω. The black dots marks the bias condition for transient response.

To measure the recovery time of the superconducting state, the microbrige was cooled to T = 3.2 K, slightly below its transition temperature T_c = 3.8 K, and biased with a direct current on the bridge. The excitation with a light-pulse creates an impedance change of the bridge, which is translated by the bias current into a voltage transient $V(t)$ between the bow-tie pads. The transients were amplified and recorded with a sampling oscilloscope. The effective bandwidth of the readout was limited to 8 GHz by the amplifier. At bias currents less than the critical current, the dc resistance was zero and the recorded transient was bipolar. Such bipolar shape is typical when a non-equilibrium state is associated with the change in the kinetic inductance [293]. The recovery of the kinetic inductance is controlled by the gap relaxation time. In order to exclude the contribution of the kinetic inductance, the detector was driven by the bias current almost into the normal-state, as it is shown in Fig. 5.5. At currents larger than the critical current, the negative part of the transient disappeared. The decaying edge becomes exponential in time

$V(t) \propto \exp(-t/\tau_f)$ with a characteristic time τ_f which initially decreases with the increase of the bias current and saturates when the actual dc resistance approaches the normal-state resistance.

Figure 5.6 shows the measured transient $V(t)$ for the 5 nm thick $W_{0.85}Si_{0.15}$ microbridge. The microbridge was biased to the operation point with the current I = 37.3 μA and the voltage V = 3.6 mV beyond which the decay time did not vary any more, as it is shown in Fig. 5.5. We fitted the rising edge and the falling edge of the transient $V(t)$ separately. For the rising edge, we fitted the transient optical response with

$$V_{\text{rising}} = V_0\{1 - \exp[-(t - t_0)/\tau_{\text{rising}}]\}, \tag{5.26}$$

resulting in a rising time of $\tau_{\text{rising}} = 52$ ps. Above the superconducting transition, τ_{rising} is mainly determined by the thermalization time τ_{th} (due to *e-e* and *e-ph* interaction), and τ_{readout} (limited by the bandwidth of readout system),

$$\tau_{th} = (1/\tau_{e-e} + 1/\tau_{e-ph})^{-1}, \tag{5.27}$$

which amounts to 27 ps at T_c. We therefore extracted the contribution of the readout τ_{readout} from the rising edge according to

$$\tau_{\text{rising}} = (\tau_{\text{readout}}^2 + \tau_{th}^2)^{1/2}. \tag{5.28}$$

The calculated τ_{readout} = 44 ps is consistent with the effective bandwidth of 8 GHz.

With respect to the falling edge, we fitted it according to

$$V_{\text{falling}} = -V_0 \exp(-t/\tau_{\text{falling}}), \tag{5.29}$$

which results in a decay time $\tau_{\text{falling}} = 630$ ps. However, the contribution from the readout needs to be removed from the total time response. The intrinsic relaxation time τ_R of the non-equilibrium state in the microbridge can be derived by combining τ_{readout} and τ_{falling} through

$$\tau_{\text{falling}} = (\tau_{\text{readout}}^2 + \tau_R^2)^{1/2}, \tag{5.30}$$

which results in a relaxation time $\tau_R = 628$ ps. Compared with the total response time of 630 ps, the contribution from the readout system to the intrinsic recovery is negligible. Since the diffusion length $\sqrt{D\tau_R} \approx 1800$ nm in our microbridge is larger than the bridge length L (for this particular 5 nm thick $W_{0.85}Si_{0.15}$ microbridge $L \approx 870$ nm), the measured relaxation time may bear a contribution from the diffusion of non-equilibrium electrons into the contact pads of the bow-tie.

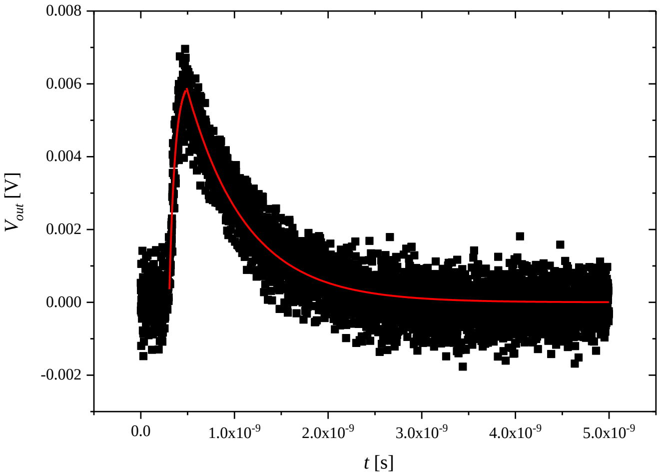

Fig. 5.6: Transient voltage response of the $W_{0.85}Si_{0.15}$ microbridge. The rising and the falling edges of $V_{out}(t)$ were fitted separately to exponential functions with time constants τ_{rising} and τ_{falling}, respectively.

Recently, Marsili *et al.* used a two-photon excitation method to deduce the hot-spot relaxation time t_{HS} in WSi SNSPDs [294]. A pair of photons was introduced with a time delay onto the nanowire meander in the superconducting state. The meander was biased at a relative current less than $I/I_c = 0.65$ in order to operate the detector in a two-photon excitation regime. Only if the time delay is shorter than the relaxation time of the hot-spot due to the first photon, a detection event can be registered. According to this method, t_{HS} was derived to be around 800 ps at T = 0.25 K. Moreover, the hotspot relaxation time is strongly dependent on the bias current, operating temperature, and photon energy. The authors interpreted the results according to a quasiparticle relaxation model based on the uniform kinetic equation [295]. We therefore can view the hotspot relaxation time as the intrinsic lifetime of the quasiparticles, and the measured τ_R can be viewed as the limitation in the normal state. In both experiments, the formation of the fluctuation area and the subsequent recovery are dominated by the diffusion and recombination of the quasiparticles.

5.5 Definition of the hotspot size based on a two-stage quasiparticle diffusion model

The most widely used model for a qualitative description of the detection process in SNSPDs is the hotspot model. A hotspot is created in the nanowire after the absorption of the incident photon, and then the bias current flowing through the hotspot area is expelled into the sidewalk outside the hotspot. When the hotspot is large enough, the current density in the sidewalk exceeds the local critical current density, which in turn drives the sidewalk into the normal state. Then the entire cross section of the nanowire becomes normal due to the Joule heat from the normal or resistive area. As a result, the bias current is shunted into the readout line, and a voltage signal is created on the readout [296]. We proposed a two-stage diffusion model to describe the formation of the hotspot [226]. To summarize, the excited electron which absorbs the incident photon continuously loses its energy by means of inelastic interactions and creates non-equilibrium quasiparticles. The growth of their number is controlled by the inelastic electron scattering rate τ_{qp}. While relaxing to low energies, the excited electron moves away from the site where the photon is absorbed. The latter process can be simplified as the diffusion with a diffusivity D_e that gives the probability to find the hot electron at the time t after the photon is absorbed at a distance r from the absorption point. Simultaneously, the created quasiparticles diffuse outside this relaxation area and recombine into Cooper pairs. The local quasiparticle density $C_{qp}(r,t)$ changes due to the diffusion and recombination with the rates $D_{qp}\nabla^2 C_{qp}(r,t)$ and $C_{qp}(r,t)/\tau_r$, respectively, which are controlled by the quasiparticle diffusivity D_{qp} and the recombination time τ_r. Diffusion dominates the evolution of $C_{qp}(r,t)$ in the nanowire when $t > \tau_{qp}$ (assuming that the photon is absorbed at $t = 0$), and finally all quasiparticles recombine back into Cooper pairs. As a result, by first assuming $D_{qp} = D_e = D$ and neglecting the edge effects, the density of quasiparticles $C_{qp}(r,t)$ around the photon absorption area can be analytically expressed as [226]

$$C_{qp}(r,t) = \frac{\varsigma h\nu}{\Delta} \cdot \frac{\tau_r}{\tau_r - \tau_{qp}} \left[\exp\left(-\frac{t}{\tau_r}\right) - \exp\left(-\frac{t}{\tau_{qp}}\right)\right] \times \frac{1}{4\pi D t} \exp\left(-\frac{r^2}{4Dt}\right). \tag{5.31}$$

In a more realistic situation, $D_{qp} \neq D_e$ (the excited high energy electron is different from the depaired quasiparticles) and also the temperature dependence of the superconducting parameters should be considered. Under such complicated conditions, we cannot give an analytical solution to the diffusion equation and only a numerical calculation can simulate the time evolution of the quasiparticle distribution [226]. When the operating temperature is not too low, however, D_{qp} is estimated to be of the same order of magnitude as D_e (e.g. in Ref.

295, D_{qp} is estimated to be $0.5D_e$ at $T > 0.5T_c$), thus we still use this approximation $D_{qp} = D_e$ in the following discussion. Within this simplified model, the total number of quasiparticles, which are introduced by the absorbed photon, is obtained by integrating the quasiparticle distribution within the two dimensional film [22],

$$N_{qp}(t) = \int_0^{\infty} C_{qp}(r,t) \cdot 2\pi r \cdot dr = \frac{\varsigma h\nu}{\Delta} \cdot \frac{\tau_r}{\tau_r - \tau_{qp}} [\exp\left(-\frac{t}{\tau_r}\right) - \exp(-\frac{t}{\tau_{qp}})]. \tag{5.32}$$

Although the lifetime of quasiparticles is much longer than the thermalization time τ_{qp}, for the sake of generality we determine the time scale t_{maxHS} at which the total number of quasiparticles reaches the maximum from $dN_{qp}(t)/dt = 0$ as

$$t_{maxHS} = \frac{\tau_r \tau_{qp}}{\tau_r - \tau_{qp}} \ln(\frac{\tau_r}{\tau_{qp}}). \tag{5.33}$$

Though the quasiparticles are continuously diffusing further away from the absorption point after t_{maxHS}, the total number of the quasiparticles starts to decrease, and the global superconductivity begins to recover. We therefore define the hot-spot radius at t_{maxHS} as

$$R_{hs} = (Dt_{maxHS})^{1/2} = [D \frac{\tau_r \tau_{qp}}{\tau_r - \tau_{qp}} \ln(\frac{\tau_r}{\tau_{qp}})]^{1/2}. \tag{5.34}$$

As a consequence, the hot-spot diameter in our case amounts to 107 nm for the 5 nm thick $W_{0.85}Si_{0.15}$ film by taking $\tau_{qp} = 9.1$ ps [104] and assuming $\tau_r = \tau_R = 628$ ps. Note that the quasiparticle recombination time approximately equals to the electron-phonon interaction time at $T \leq T_c$ only. At an operation temperature of 0.25 K, the recombination time will grow to a few microseconds, increasing the hot-spot size to approximately 400 nm. Anyway, even at $T \approx T_c$, the expected hot-spot size is comparable with the most commonly used nanowire width of 100 nm. Neglecting the diffusion process would result in a hard core hot-spot $\sim(D\tau_{qp})^{1/2}$ with a diameter of only 52 nm. Hence, without consideration of the diffusion, the hot-spot size is significantly underestimated. According to our simplified model, both time constants play important roles in the formation of the hot-spot although τ_{qp} is significantly shorter than τ_r. The hot-spot size is determined by a diffusion-based multiplication process, i.e., is mainly dominated by the lifetime of the non-equilibrium quasiparticles. With increasing bias current and decreasing temperature, Marsili *et al.* found that the hot-spot relaxation time τ_r increased significantly, which in turn leads to the increase of the hot-spot size [294]. The hotspot size estimated here is quantitatively consistent with the experimental determined hotspot size from a 130 nm wide WSi SNSPDs [297].

With respect to NbN-based devices, the τ_r is around 20 to 25 ps, and τ_i is found to be around 1.6 ps. The experimentally determined D_e of NbN ranges from 0.4 to 0.5 cm^2/s. Inserting them into Eq. 5.34, we can estimate that the hotspot size of NbN for 1550 nm photons is around 25 nm, which is significantly smaller than the wire width of the commonly used NbN nanowire detectors, ~ 100 nm. This estimated hotspot size can also be quantitatively examined by a quantum detection tomography experiment, which found a hotspot size of 23 nm for NbN [297].

For this simple two-stage diffusion model we did not consider the suppression of superconductivity from the incident photon and the bias current, namely the changes of the depairing energy and the order parameter. Moreover, in order to have an even more accurate description of the dynamic process and the dependence of the hot-spot size on external parameters, the escape of phonons should also be considered.

6 Superconducting nanowire single X-ray photon detectors

6.1 X-ray source calibration

Throughout our experiment, a tungsten target based X-ray tube from *Oxford Instrument* has been used. The applicable voltage V_A of this tube is limited at 49.9 keV, and the current I_A of the tube is limited at 2 mA. In order to introduce the X-ray photons into the cryostat, a 100 µm thick kapton film as a window is placed on the wall of the cryostat for keeping the vacuum, as it is shown in Fig. 6.1. Moreover, a huge number of infrared photons are ejected from the tungsten target during the X-ray photon emitting. In order to shield these infrared photons from the detector and achieve a good temperature stability at the sample stage, a 1 µm thick aluminum film is placed on the wall of liquid nitrogen jacket (see in Fig. 6.7).

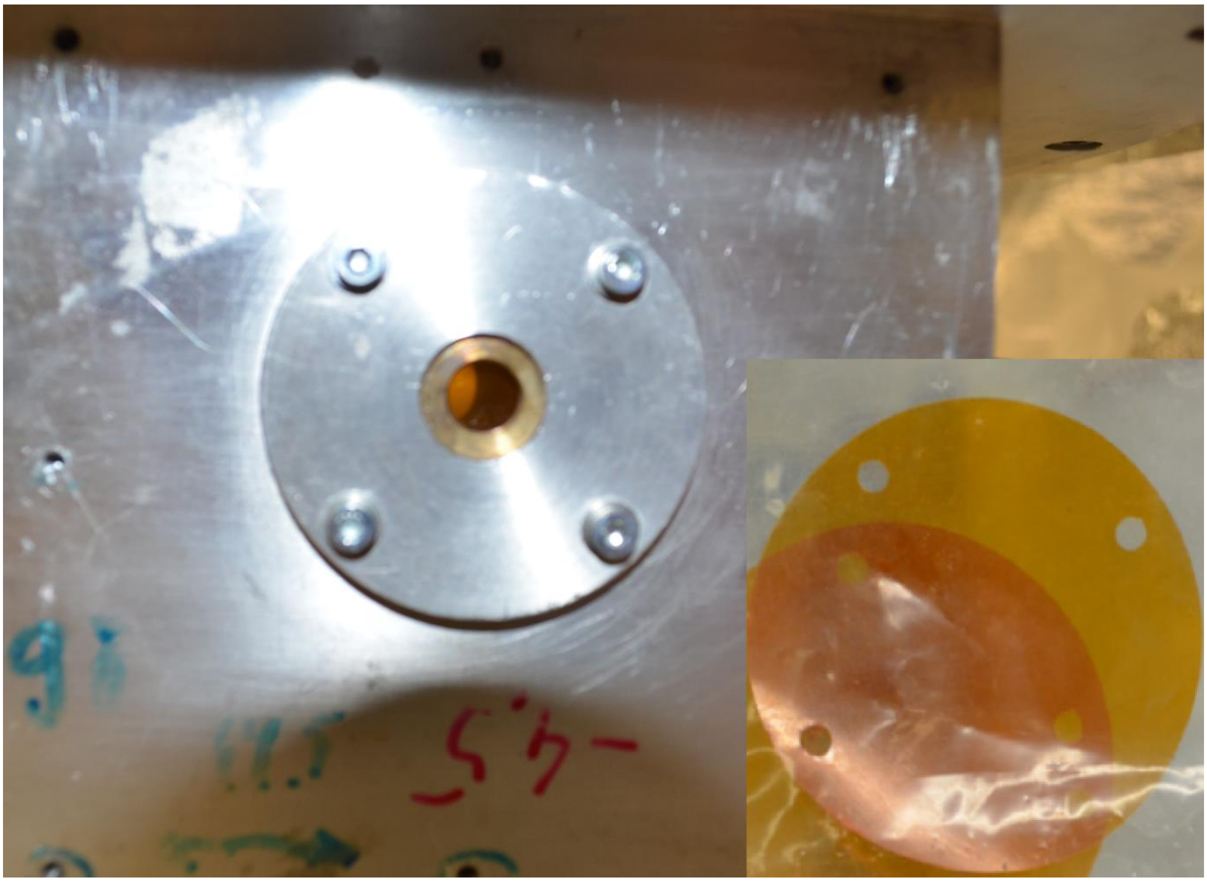

Fig. 6.1: The 100 µm thick kapton film used for keeping the vacuum is essentially transparent for X-ray photons.

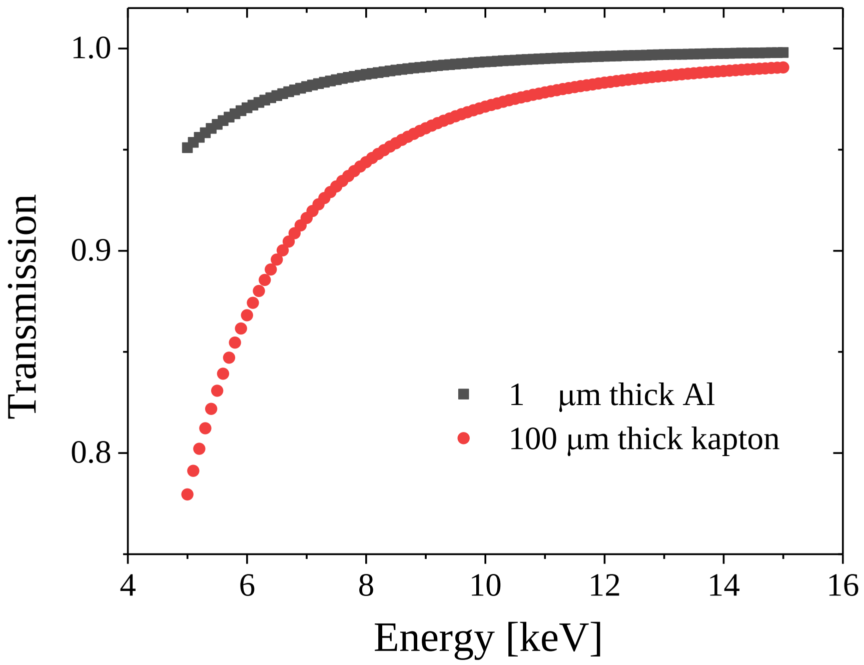

Fig. 6.2: Transmission probability of X-ray photons through the 100 μm thick kapton film and the 1 μm thick Al film.

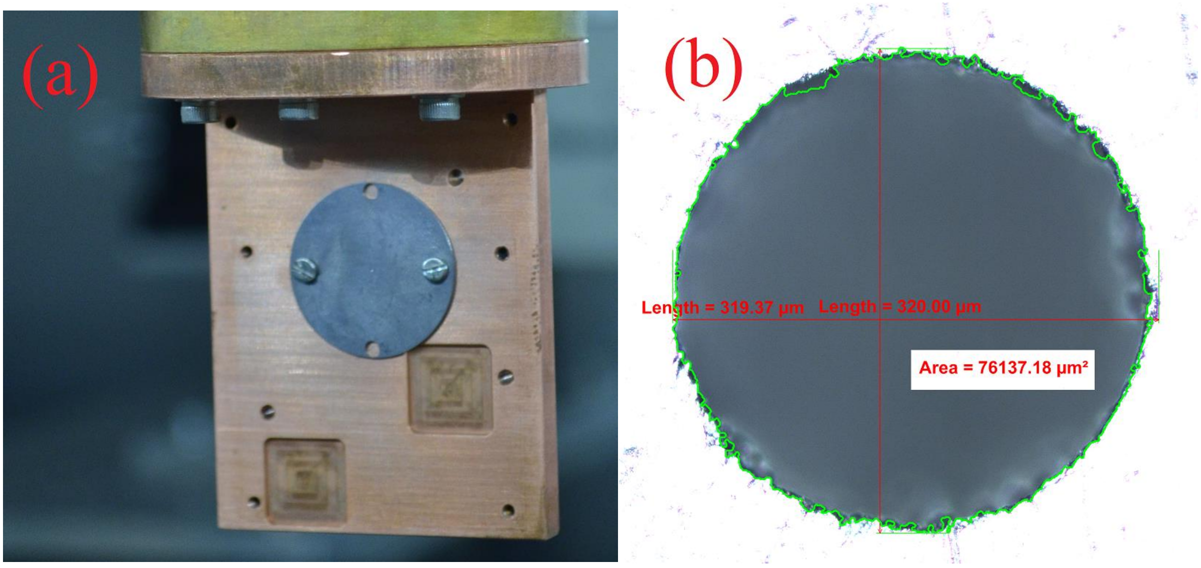

Fig 6.3: (a) Configuration for the X-ray photon flux measurement. (b) The microscope image of the small hole in the center of the tantalum film.

Though the kapton film and the Al film on the optical path attenuate the X-ray photons flux, there are still enough X-ray photons incident on the sample stage due to the ~ 90% transmission probability of these two films, as it is shown in Fig. 6.2.

In order to measure the X-ray photon flux on the sample stage (X-SNSPD), a tantalum film with a small hole in the center is placed on the sample stage, as it is shown in Fig. 6.3. Behind the tantalum film, the X-ray photons transmitted through the hole are detected by a commercial semiconductor detector (see below). The area of the small hole ~ 76137.18 μm^2 is measured via a *Nikon* microscope. From the area of the hole and the photon number per second detected by the detector, the flux of X-ray photon can be determined.

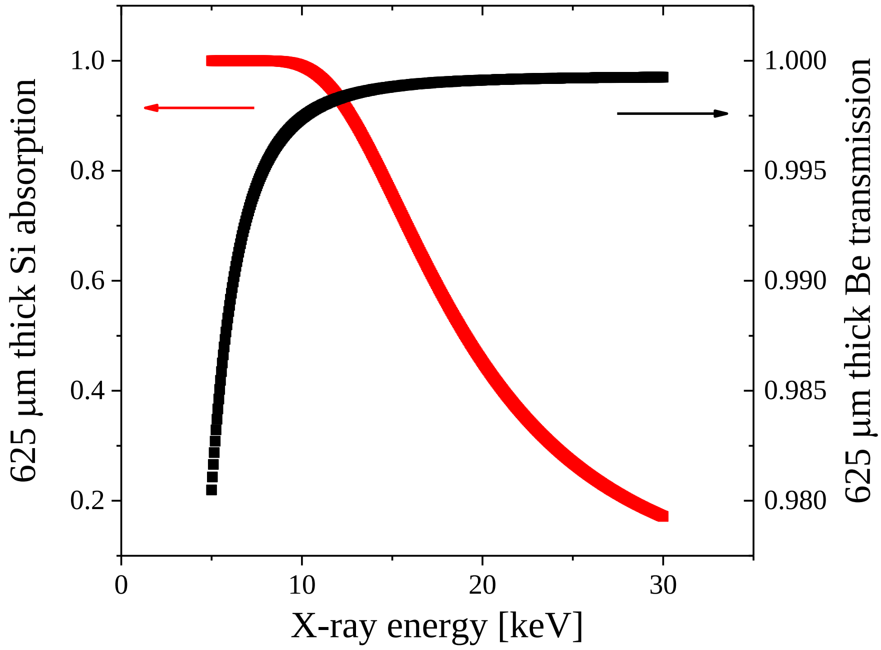

Fig. 6.4: The absorption of the 625 μm thick Si PIN detector (red) and the transmission of 25 μm Be window (black).

The X-ray photons are counted by XPIN-BT X-ray detector, which is a compact, low-cost Energy Dispersive X-Ray Florescence (EDXRF) device. The X-ray photons are directly detected by a silicon PIN diode, which has an area of 6 mm^2 and a thickness of 625 μm. In front of the detector, there is a 25 μm thick beryllium protection window. In order to exactly determine the X-ray flux near the sample stage, we have excluded the influence from the attenuation of the beryllium window and the absorption of the PIN detector, as it is shown in Fig. 6.4.

Figure 6.5 shows a measured X-ray spectrum after calibration under an acceleration voltage of $V_A = 30$ kV and a cathode current of $I_A = 0.01$ mA. The corresponding characteristic energies for this tungsten-based X-ray are L_α = 8.4 keV, $L_{\beta 1}$ = 9.67 keV, $L_{\beta 2}$ = 9.96 keV, and L_γ = 11.29 keV.

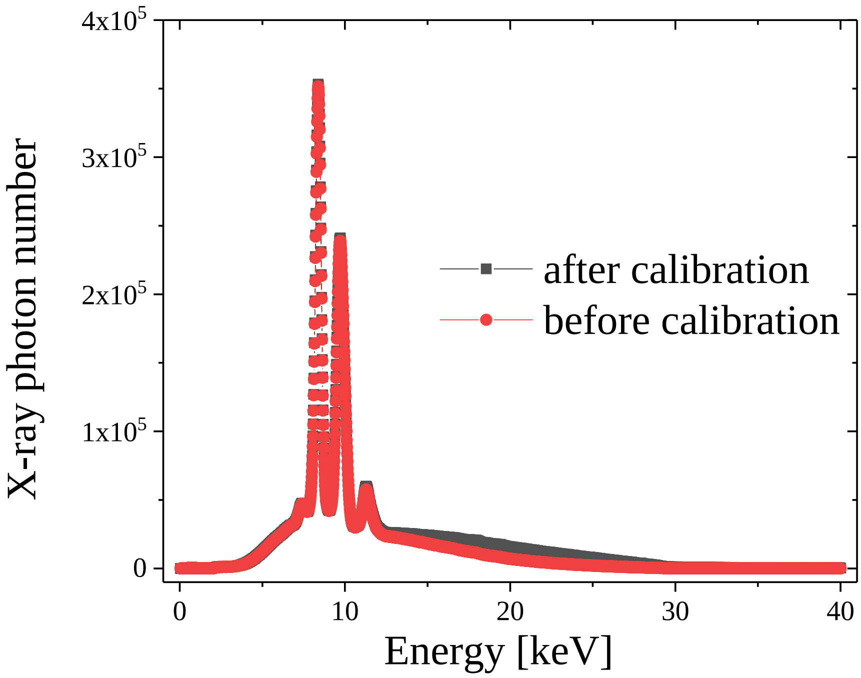

Fig. 6.5: A calibrated characteristic X-ray spectrum for our tungsten target. The applied acceleration voltage is 30 kV and the current is 0.01 mA.

For experiments with this tungsten tube, some high energy photons (> 11.3 keV) are also irradiated onto the detectors due to the bremsstrahlung effect. In order to eliminate this and to achieve X-ray photons with expected characteristic energies, we designed a reflection-based configuration, which is described in detail in ref. [299]. As it is shown in Fig. 6.6 (a), the X-ray photons are incident on a pure metal target, and the fluorescence X-ray photons are then reflected and introduced onto the sample.

We have tested the fluorescence spectrum from a copper and a germanium targets. The characteristic X-ray photon energies for Cu are $K_\alpha = 8.042$ keV and $K_\beta = 8.906$ keV, as it is shown in Fig. 6.6 (b). With respect to the Ge target, there are two characteristic X-ray peaks, $K_\alpha = 9.876$ keV and $K_\beta = 10.983$ keV. In order to achieve the highest X-ray photon flux, these data are obtained with the settings $V_A = 49.9$ kV and $I_A = 2$ mA. Moreover, we also adopted a ^{55}Fe radioactive X-ray source, which has two characteristic X-ray photon energies of 5.90 keV and 6.49 keV, as it is shown in Fig. 6.6 (c).

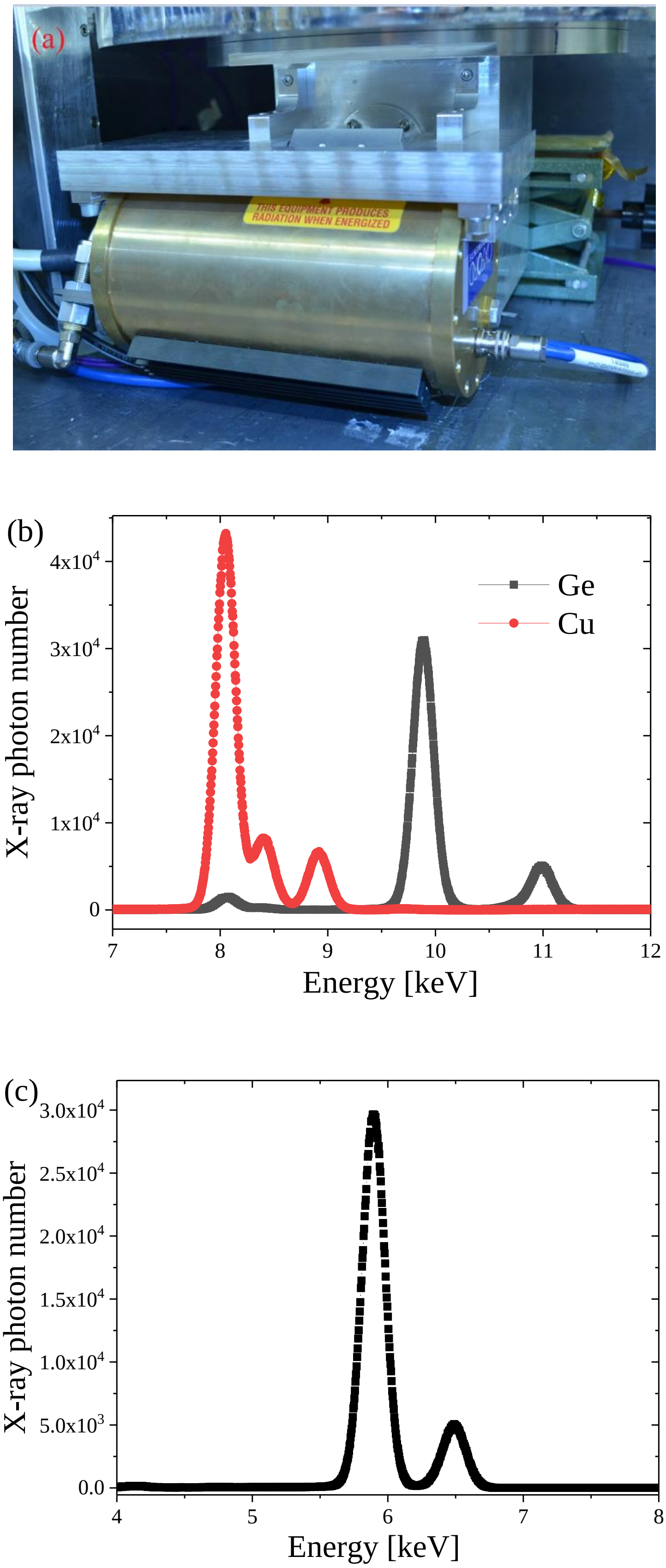

Fig. 6.6: (a) The designed X-ray reflection configuration. (b) Characteristic X-ray spectrum of Cu and Ge targets. (c) Characteristic X-ray spectrum from the radioactive ^{55}Fe source.

6.2 Physical properties of WSi-X-SNSPD

The WSi-X-SNSPD was prepared from a 100 nm thick $W_{0.8}Si_{0.2}$ film. The narrow stripes were patterned by EBL with HSQ resist and etched by reactive ion etching in SF_6. The device has a stripe width of w = 920 nm with a filling factor of 66%, which covers a sensitive area of 41.6 $\times$ 28 μm^2, as it is shown as a inset in Fig. 6.7. The sample was fixed at a He-3 cooling stage, which is able to stabilize the temperature below 1 K. The detector was biased with a constant current through a series of low-pass filters at room temperature. The detection signal was at first amplified with two amplifiers with a total gain of $G = 60$ dB, and then fed into a 3.5 GHz *Tektronix* digital oscilloscope for photon counting.

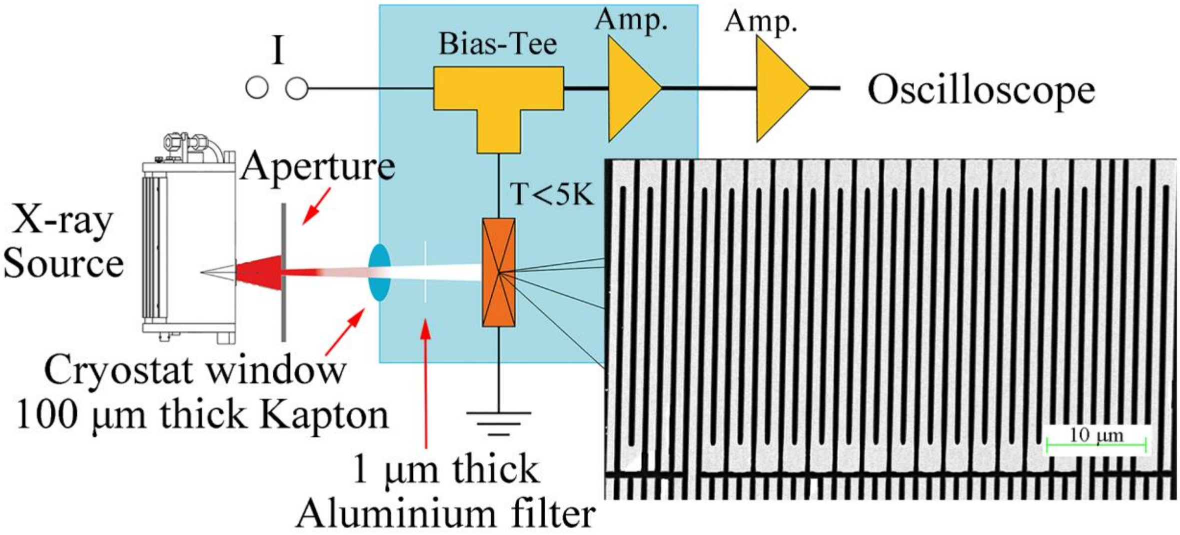

Fig. 6.7 Scheme of the experimental setup. Inset: SEM image of the X-SNSPD.

Figure 6.8 (a) shows the superconducting transition of the device. The temperature dependence of resistance was fitted according to the 3D AL fluctuation formula Eq. 4.1. The thus obtained critical temperature is T_c = 4.97 K, which is identical with that of the as-grown films. Therefore, the fabrication process does not have any detectable influence on T_c. The experimental critical current I_c, which was obtained from the I-V curve without X-ray illumination, is plotted as a function of temperature in Fig. 6.8(b), and the data can be well fitted by the GL mean field expression [300],

$$I_c(T) = I_c(0)[1-(\frac{T}{T_c})^2]^{3/2}[1+(\frac{T}{T_c})^2]^{1/2}. \tag{6.1}$$

Here $I_c(0)$ is the critical current at 0 K, which is determined by the critical field $H_c(T)$ and the penetration depth $\lambda(T)$. The corresponding value of the critical temperature from this fitting is T_c = 5.02 K, which is consistent with the result from the resistance measurements.

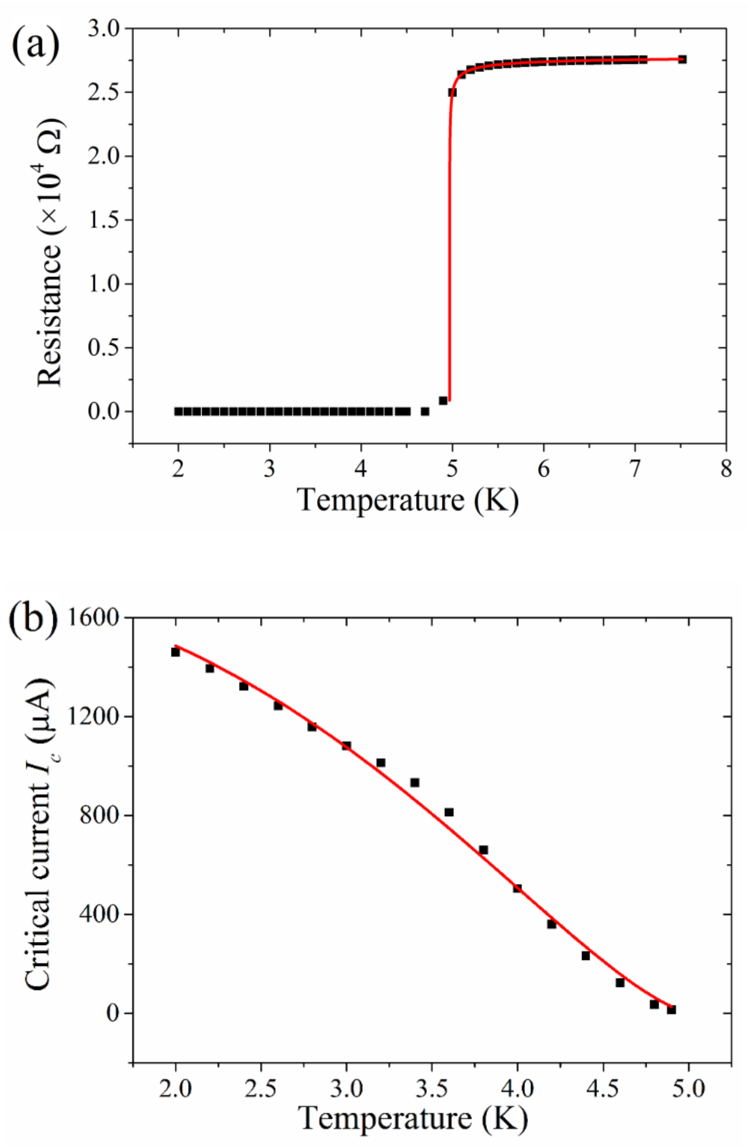

Fig. 6.8: (a) $R(T)$ with a fit to the AL fluctuation formula (red line). (b) The critical current as a function of temperature is fitted with Eq. 6.1 (red line).

6.3 Single X-ray photon sensitivity

In order to investigate the photon number resolving ability of this detector, we measured the count rate dependence on the X-ray source current I_A. Figure 6.9 shows the measured count rate as a function of the current at $V_A = 30$ keV. The X-ray photon number is proportional to the source current, therefore Fig. 6.9 illustrates the count rate dependence on the X-ray photon number at different device bias currents I_b. The dashed line in the diagram has a slope of 1. The linear behavior of the count rates at all bias currents indicates that the detector is operated in the single photon detection mode [16].

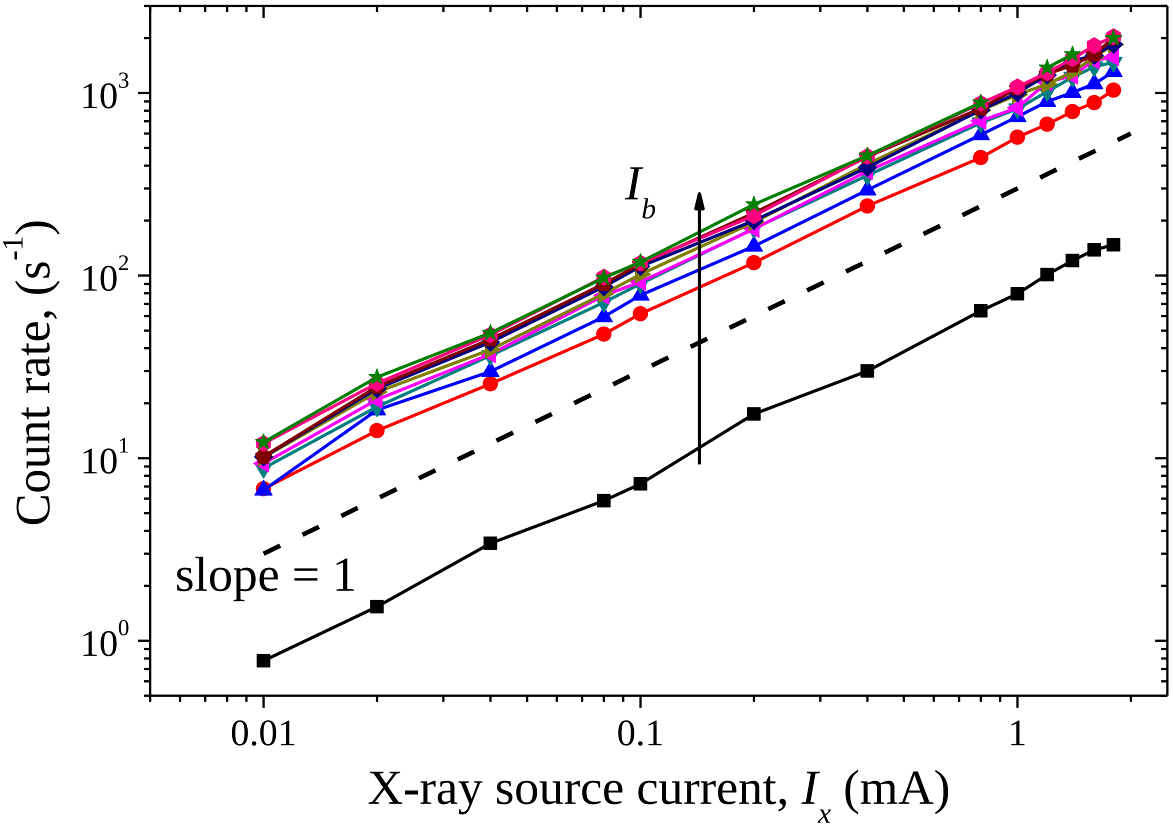

Fig. 6.9: The measured count rates vs. the X-ray source current I_x (with an acceleration voltage V_A = 30 kV) at bias current I_b ranging from 10 µA to 100 µA, in increments of 10 µA. The dashed line has a slope of unity.

6.4 Detection performance

In order to test the detection performance, we measured the count rate dependence on the bias current at different temperatures with X-ray source voltages of 30 kV and 50 kV.

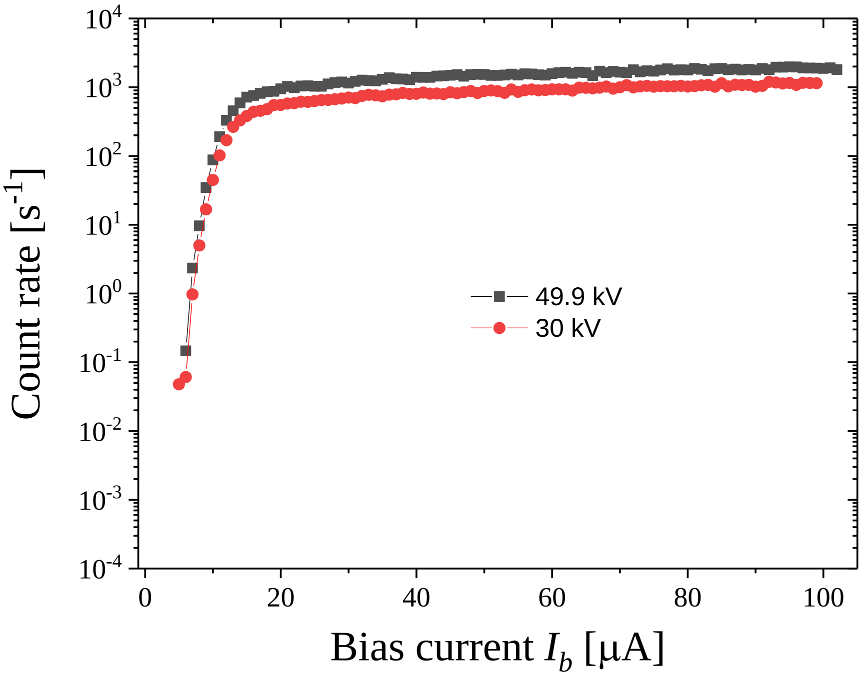

Fig. 6.10: Count rate as a function of the bias current at 1.8 K with X-ray source voltages of 30kV and 50kV.

At first, we measured the WSi X-SNSPD at low temperatures. Figure 6.10 shows the bias current dependence of the count rate at different source voltages at $T = 1.8$ K. The detector starts to respond to the X-ray photons at a bias current as low as 5 μA. At relatively high currents, the detection performance is limited by the latching effect, which will be discussed in next section.

For characterizing a low temperature detector in the context of practical applications, the detection performance at $T = 4.2$ K is of great importance. Figure 6.11 shows the detection performance of the WSi X-SNSPD at 4.2 K. This detector is still sensitive to the incident X-ray photons at a bias current as low as 3 μA, which is two orders of magnitude smaller than its critical current.

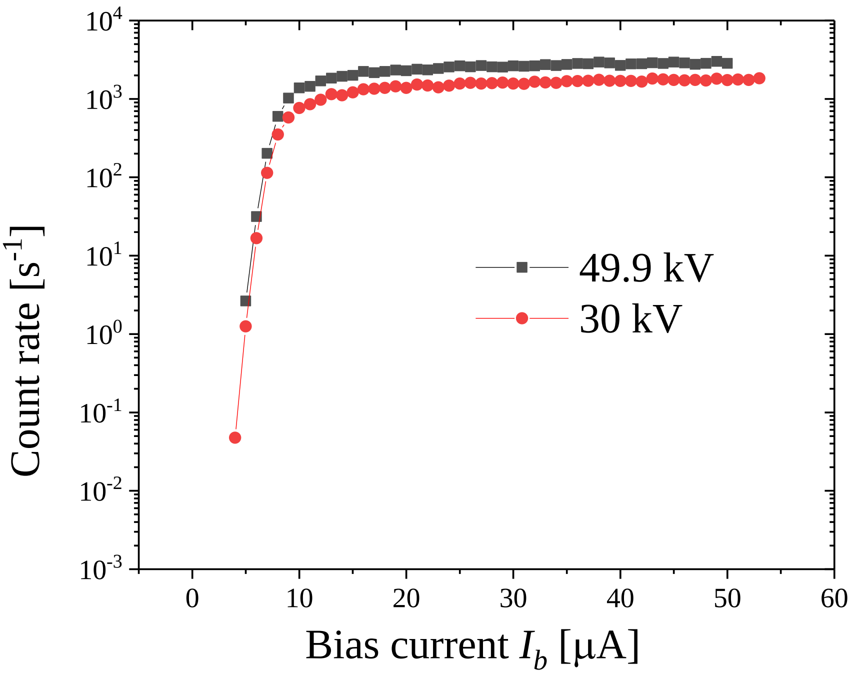

Fig. 6.11: Count rate as a function of the bias current at liquid helium boiling temperature.

To compare the detection performance at different temperatures, figure 6.12 shows the count rates as functions of the bias current, normalized by the critical current at each temperature, for V_A = 30 kV and 49.9 kV. The X-ray source current I_A is fixed at 1 mA throughout these experiments. Our detector starts to react to the X-ray photons under a bias current as low as I_b = 5 μA in the low temperature range, i.e., well below 1% of I_c at T = 1.8 K. For a typical optical SNSPD, detection events are collected at relatively high bias current, ~ 20% of I_c, and saturated count rates (i.e., with maximum internal detection efficiency) can be only realized below a relatively low temperature, of the order of ~ 0.5T_C [19, 301]. At high temperatures, however, no saturation can be observed. For our X-ray fetector, the range of saturated bias current I_{th} above which count rates stay constant, becomes larger with further decreasing temperature. With the decrease of the temperature, the saturation current I_{th} decreases from ~ 24% of I_c at 4.8 K to ~ 5% of I_C at 1.8 K. Unlike these optical detectors, our X-ray detector is able to work even at T = 4.8 K, just below its critical temperature, with I_{th} as low as 25% of its critical current (see Fig. 6.12).

The maximum count rate at V_A = 50 kV and I_A = 1 mA is approximately 3100 s^{-1}. Taking the detector area into consideration, the saturated counts-per-second-per-square-millimeters (CPSPSM) is 2.7 $\times 10^6$ cps at all temperatures, even at 4.8 K ($\approx$ 0.96T_c). The CPSPSM of our Nb and TaN based X-SNSPDs at the same acceleration voltage and source current are 2 $\times 10^5$

cps at $0.2T_C$ and 2.1×10^6 cps at $0.28T_c$ (see Table 6.1), respectively. Therefore the WSi based X-SNSPDs has indeed an improved detection performance as compared to granular Nb-based superconducting devices.

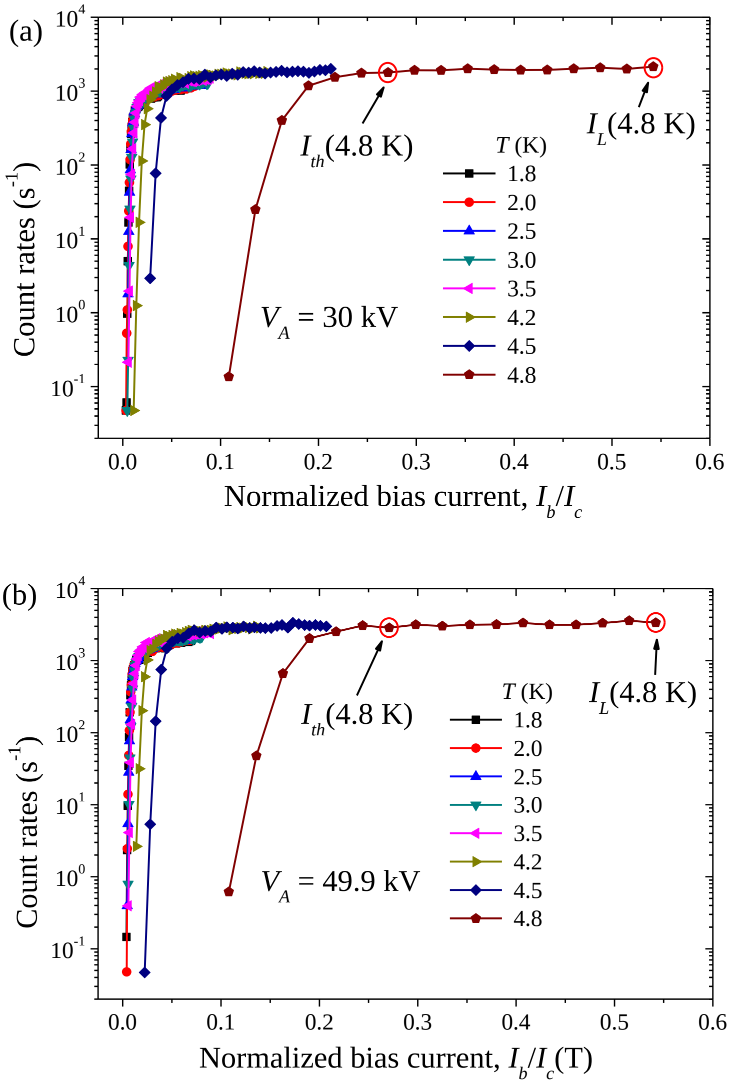

Fig. 6.12: Count rate as functions of the reduced bias current (normalized by the critical current at each temperature) with acceleration voltages of (a) 30 kV and (b) 49.9 kV. The definitions of the threshold current I_{th} and the latching current I_L at T = 4.8 K are marked in the figure with circles.

6.5 Hotspot size in WSi X-SNSPDs

For the 100 nm thick WSi used for X-SNSPDs, the 2D quasiparticle diffusion model is not applicable any more. As a result, the hotspot size can be estimated from the threshold current I_{th}. From Eq. 3.14, the hotspot size can be defined as,

$$D = w(1 - \frac{I_{th}}{I_c}). \tag{6.2}$$

This expression is based on the assumption that the hypothetic hotspot size is much larger than the film thickness, and the hotspot within the nanowire can therefore be viewed as a cylinder. The critical current at each temperature can be obtained from Fig. 6.8 (b), while the threshold current can be extracted from Fig. 6.12. For $V_A = 50$ kV and $I_A = 1$ mA, the calculated hotspot diameters are ~ 700 nm at 4.8 K and ~ 874 nm at 1.8 K. Note that due to the ultrahigh photon energy, thses estimated hotspot diameters here are significantly larger than the determined hotspot diameter induced by the visible photons in two dimensional $W_{0.85}Si_{0.15}$ thin films. For comparison, in Nb and TaN based X-SNSPDs, the calculated hotspot size is ~ 420 nm at 1.75 K and ~ 540 nm at 1.85 K, respectively [187,188]. Thus, the WSi materials are indeed more sensitive to photons with the same energy than Nb and TaN. In order to improve the signal to noise ratio, we could in principle even further increase the nanowire width. Taking the X-ray photon flux into consideration, the system detection efficiency of the WSi detector is estimated to be 7.5%.

6.6 Latching effects

As it is shown in Fig. 6.12, the bias current dependence of the count rate terminates at a relatively low bias current (when compared with the I_c) at all temperatures. This termination of detection performance is attributed to the latching effect.

For a current-biased superconducting nanowire single photon detector, a hotspot is created after the photon absorption and the bias current is shunted into the readout circuit. Then the superconductivity within the hotspot starts to recover with a time scale of τ_r. The recovery time of the bias current τ_I, however, is limited by the kinetic inductance and the load impedance R_L [43,176,177,302],

$$\tau_I = L_k/R_L. \tag{6.3}$$

The kinetic inductance is determined by the device geometry and the materials properties,

$$L_k = \mu_0 \frac{\lambda_{eff} l}{w}. \tag{6.4}$$

Here $\lambda_{eff} = 2\lambda^2/d$ is the effective magnetic penetration depth, with l, w and d are the length, width and thickness of the nanowire, respectively. Taking the device geometry and the material parameters into account, we can obtain a kinetic inductance L_k~9.7 nH. As a consequence, we expect that the redistributed bias current recovers in the detector within a time scale τ_I~0.2 ns, which is nearly an order of magnitude faster than the recovery time of superconductivity. When the bias current shunts back to the nanowire, there is therefore still a finite resistance in the nanowire, which continuously creates Joule heat Q_J in the wire wccording to $Q_\mathrm{J}(t) = I_b^2(t)R_n(t)$. At low bias currents, this heating effect is negligible and the sample stage can quickly cool the detector into the superconducting state. With increasing the bias current, a dynamic equilibrium $Q_\mathrm{J}(t) =$ cooling power is reached, and the detector will then latch into a thermal equilibrium state, which makes the detector not sensitive to the incident photons any more. This state of SNSPDs is called a latching state [303,304].

The current which characterizes the latching effect can be defined as the bias current I_L where the count rate terminates (see in Fig. 6.12). Figure 6. 13 shows the temperature dependence of I_L. This state corresponds to a dynamic thermal equilibrium, therefore I_L is independent of the X-ray photon flux, but only depends on the cooling power, namely the sample stage temperature.

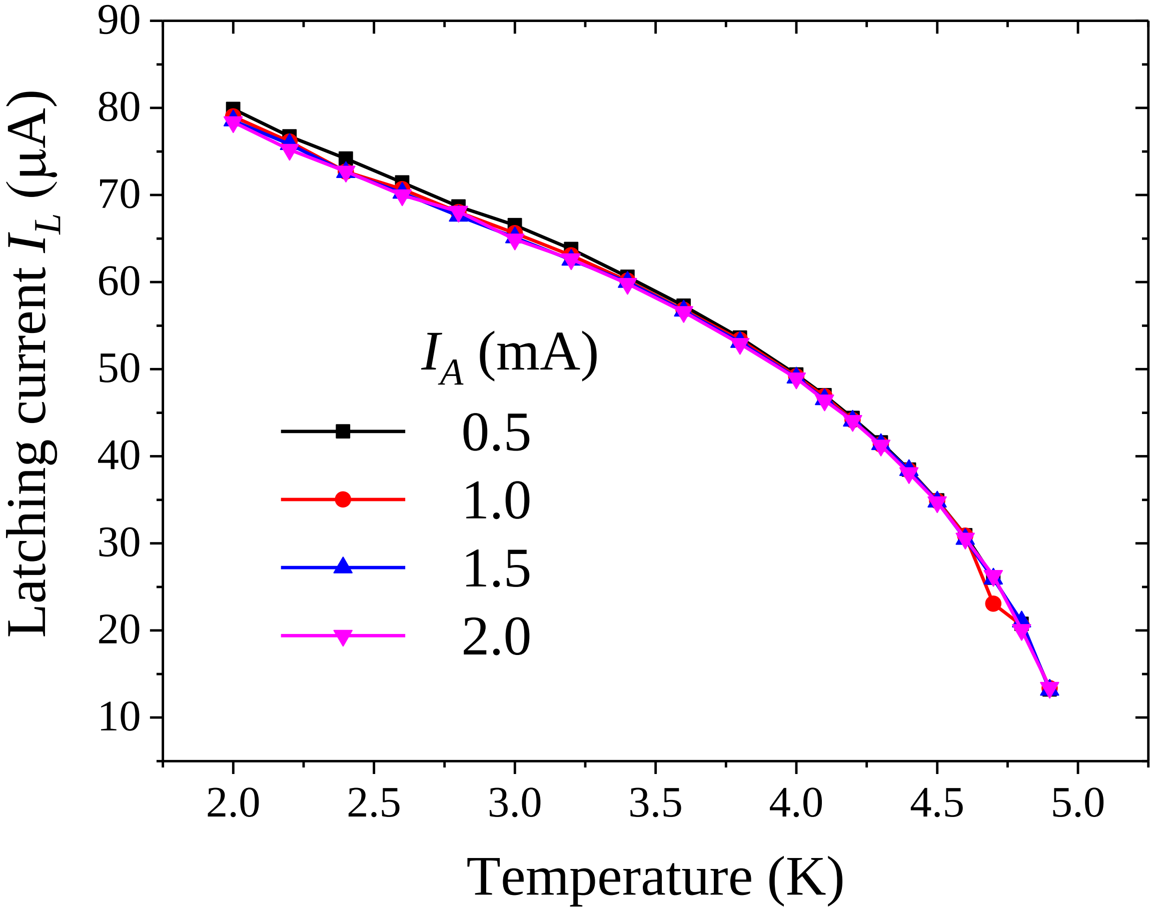

Fig. 6.13: The latching current I_L as a function of temperature under different X-ray source currents I_A.

6.7 Dark counts

A dark count event describes a false signal, which is not caused by the absorption of a photon. A high dark count rate significantly suppresses the signal-to-noise ratio of detector. Currently, there are several proposed mechanisms for dark count events [212]: (a) the background radiation from the shielding; (b) the stray photons that couple into the cryostat; (c) the vortex crossing effect in a current biased nanowire; (d) the vortex-antivortex depairing effect; (e) the thermally activated or quantum phase slip processes.

With respect to the dark counts of our X-ray detector, our oscilloscope did not collect any dark count events within 1 min at the highest temperature and the highest applied bias current (99% of the critical current I_C at T = 4.8 K), and therefore the dark count rate for our detector is lower than ~ 10^{-2} s^{-1}. This is not surprising since the device geometry is unfavorable with respect to all the known dark event mechanisms [212]. For dark counts induced by the phase-slip , either by quantum phase slips or thermally activated phase slips, the dark count rate is significant only when the cross section of the nanowire wd is as small as $\xi^2(\xi = 6.7$ nm is the coherence length) which is not the case here. Moreover, the characteristic unbinding energy of a vortex-antivortex pair is proportional to the film thickness d, and therefore the dark counts coming from possible unbinding of vortex-antivortex pairs are intrinsically suppressed due to the relatively large thickness $d \gg \xi$ in our case [227]. Finally, the dark counts from vortices overcoming the entry energy barrier are suppressed since the energy barrier for the vortex entry also scales with the film thickness [212,227].

Due to the device geometry of our X-detectors, blackbody radiation and stray optical photons are not able to trigger the detector. Moreover, our detector was shielded with a 77 K steel box and a 2 K gold plated box. Thus, the influence of ambient radiation on the detector was negligible.

6.8 Signal amplitude distribution

Generally speaking, SNSPDs are not able to discriminate the incident photon energy since after the photon absorption, all the bias current is shunted into the readout. As a result, the signal pulse amplitude is independent of the bias condition and the photon energy. However, our recently developed Nb-based X-SNSPD has shown a possible energy resolution [187]. In a current biased superconducting stripe, intuitively, the quasiparticle number is related to the photon energy, which in turn relates the X-ray photon energy to the signal amplitude.

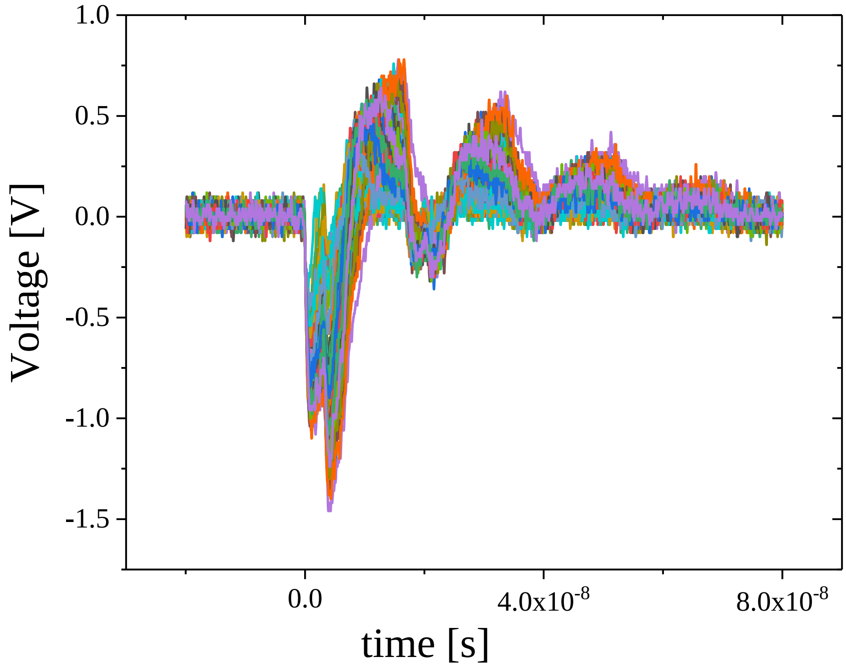

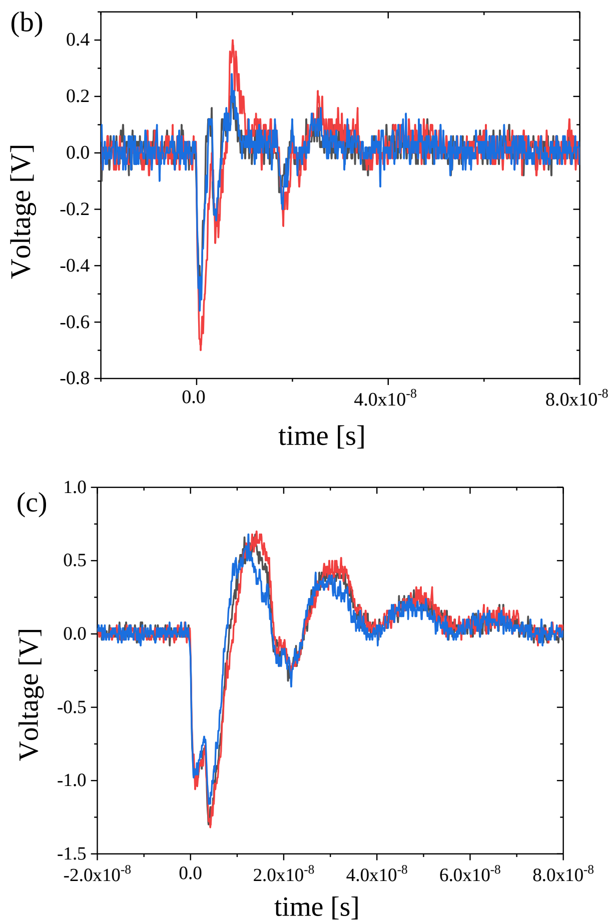

Fig. 6.14: (a) Signal pulses collected by an oscilloscope at 2 K with a bias current of 70 μA. (b) Signals with small amplitudes. (c) Signals with large amplitudes.

Figure 6.14 shows the signal pulses detected by our WSi detector, which are collected by the oscilloscope at 2 K with a bias current of 70 μA. These signal pulses can be categorized into two kinds: the signals with small amplitude (Fig. 6.14 (b)), and the signals with larger amplitude (Fig. 6.14 (c)). In order to find a relationship between the signal amplitude and the characteristic X-ray photon energy from the tungsten target, the pulse amplitudes are analyzed. We have collected 20000 pulses, whose amplitudes range from 0 to -2 V. Figure 6.15 illustrates the histogram of the pulse height distribution with $V_A = 30$ kV and $I_A = 1$ mA at $T = 2$ K.

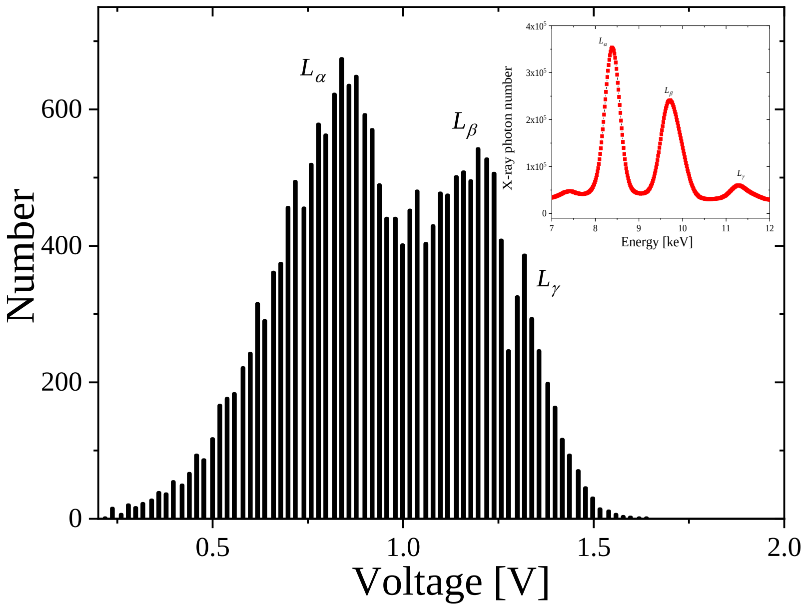

Fig. 6.15: Histogram of the pulse amplitude distribution with $I_b = 70$ µA at $T = 2$ K. Inset: measured characteristic spectrum of the W source.

There are three clear characteristic peaks in the histogram. The X-ray source with the tungsten target, the $L_\alpha = 8.4$ keV line holds the highest photon flux; the $L_\beta \sim 9.7$ keV peak has the medium flux; while the $L_\gamma = 11.29$ keV line is the weakest. The perfect correspondence between the signal amplitude and the photon energy demonstrates a possible energy resolution of the WSi X-SNSPD.

At a higher bias current, the X-ray photons with smaller energy are also able to transfer all the bias current into the readout. As a result, most of the pulse amplitudes approach to $I_b R_L G$ (where G is the amplification factor), and the energy resolution disappears, as it is shown in Fig. 6.16.

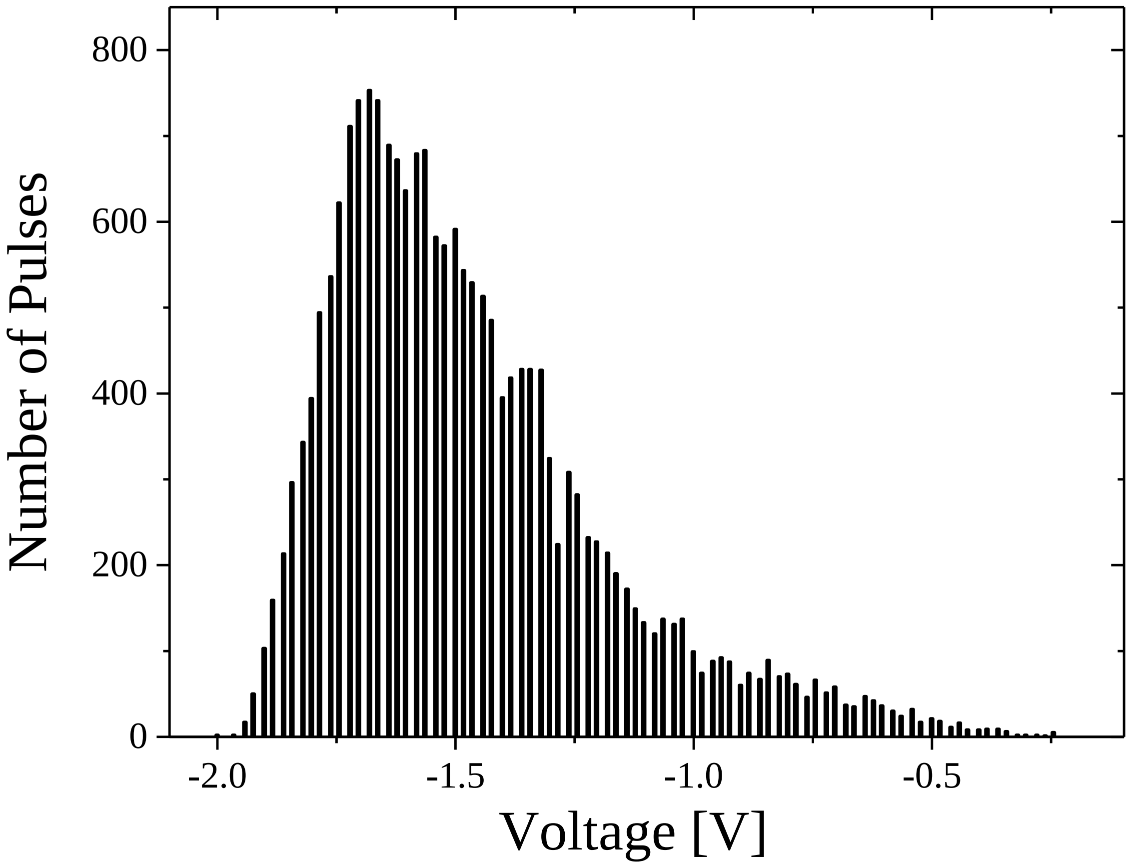

Fig. 6.16: Histogram of the pulse amplitude distribution with $I_b = 100$ µA at $T = 2$ K.

The shape of the signal pulse, however, is strongly influenced by our readout line, which has a strong reflection. Therefore, the pulse amplitude distribution is affected by the reflected pulse, leading to a distortion of the original signal pulse.

6.9 Conclusion

In conclusion, we successfully fabricated X-SNSPDs based on amorphous WSi, which show a great potential for an application as fast single X-ray photon detectors. The WSi X-SNSPDs can be operated with optimum internal detection efficiency just below the critical temperature, even above the boiling temperature of liquid helium. The detector reacts to incident photons at ultralow bias currents of less than 1% of the critical current at low temperatures, with a wide saturation range of constant count rate. Dark counts in our detector are negligible up to the highest investigated bias currents (99% of I_c) and operating temperature (4.8 K). Moreover, our detector also shows a certain energy resolution to the tungsten based X-ray source, which may need to be improved in the future.

Table 6.1: Comparison between $W_{0.8}Si_{0.2}$ and previous Nb and TaN detectors

Sample	T_c (K)	w (nm)	size (μm^2)	CPSPSM (cps)	rise time (ps)	hotspot (nm)	I_L/I_c	I_{th}/I_c
Nb	8.40	360-410	131×55	0.2	250	420	5.5% @1.75K	——
TaN-A	6.70	275-340	35×33	2.1	750	540	52% @1.85K	8% @1.85K
TaN-B	7.00	1800-1900	66×119	1.3	910	——	32% @1.85K	——
$W_{0.8}Si_{0.2}$	4.97	920	41.6×28	2.7	400	874	54% @4.8K	5% @1.8K

7 Superconductor to insulator transition (SIT) in quasi 2D WSi

7.1 SITs driven by quantum and thermal fluctuations

Once the temperature is driving below the critical temperature T_c of superconductors, the superconducting state is phenomenologically characterized by dissipationless electric currents and the Meissner effect [105]. This state, however, can be destroyed by external parameters, such as the magnetic field, pressure, or the disorder level, which can lead to a transition from the superconducting to insulating, or a metallic state [306].

For SITs at finite temperatures, the critical behavior within the critical region is mediated by thermal fluctuations [306]. Once the temperature is lowed close to zero temperature, such SITs between two quantum ground states are governed by quantum fluctuations, leading to a continuous quantum phase transition (QPT) [307]. Such zero-temperature QPTs between different quantum states are expected to occur when a control parameter in the Hamiltonian crosses a certain critical value [306]. Near QPTs, physical quantities for an equilibrium system can be classified into distinct universality classes determined only by the general properties of the system, such as space dimensionality, range and dynamics of the interactions, and symmetry, independently of the microscopic details [305-310]. The zero-temperature superconductor-to-insulator QPT driven by the applied magnetic field in two dimensions is a well-documented manifestation for such a QPT.

An experimental characteristic of such transitions is the scaling behavior of physical quantities [305-307]. When the system enters the critical region close to the phase transition, the measured physical quantities show a power-law dependence on the rescaled spatial and time coordinates, e.g., the correlation length ξ (depending on the proximity to the phase transition point, $\xi \sim |x - x_c|^{-\nu}$) and and correlation time τ ($\tau \propto \xi^z \propto |x - x_c|^{-z\nu}$) [105, 305-310]. These two scaling parameters ξ and τ, which both diverge at the transition point, are determined by the microscopic parameters in the Hamiltonian describing the system. The correlation length exponent ν and dynamical critical exponent z, however, are determined only by the universality class, which depends on the general properties of the system, such as the space dimensionality d, presence of disorder, and the symmetry of the order parameter manifold [305-312]. For a magnetic-field driven SIT, the sheet resistance can be rescaled as $R_s(B,T) \propto |B - B_c|^{2-d} F(|B - B_c| T^{-1/z\nu})$, with an arbitrary but for the system universal scaling function $F(x)$ with $F(0) = 1$. In the 2D ($d = 2$) limit, ξ drops out, R_S at the critical point becomes universal (R_Q), and $R_s(B,T) = R_Q F(|B - B_c|T^{-1/z\nu})$, where $R_Q = h/4e^2$ is the quantum resistance for Cooper pairs [105].

The superconducting state is characterized by an order parameter, in terms of amplitude (related to energy gap Δ or Cooper-pair density n_s), and phase ϕ. As a result, a SIT can be grouped into two distinct classes, with fermionic and with bosonic descriptions. The fermionic scenario describes the SIT as a result of the amplitude fluctuations, in which a SIT is driven by the breaking of Cooper pairs and the localization of electrons, forming a Fermi insulator [313-318]. On the contrary, the SIT in the bosonic description is driven by fluctuations of the phase, in which the superconducting and the insulating states with different symmetry are separated by a QCP [309,310,319]. On the superconducting side of such a transition, the Cooper pairs are mobile. Magnetic vortices are localized and can be bound into vortex-antivortex pairs [308]. On the insulating side, the vortices are mobile but the Cooper pairs are localized, forming a Bose-insulating state [309,310,320,321]. A number of SIT experiments suggest that the localization of Cooper pairs leads to a quantum-percolation induced superconductor-to-Bose-insulator transition, with a product of the correlation length and dynamical exponents $z\nu \sim 4/3$ near the quantum critical point (QCP) [306,308,311,312,322-324]. However, a superconductor-to-Fermi-insulator transition has also been found in some experiments, with $z\nu \sim 2/3$ [317,325-327]. Although many SIT experiments driven by different control parameters have been reported for a variety of materials and with varying $z\nu$ products, the nature of the non-superconducting ground state at zero temperature and the reason for the difference in the respective $z\nu$ values are still unclear [306,328].

7.2 Zero temperature superconductor to insulator QPT

Detailed transport measurements on 5 nm thick $W_{0.75}Si_{0.25}$ bridges in different magnetic fields down to 0.34 K were performed in a PPMS system with a helium-3 refrigerator option. These bridges have a T_c of ~ 3.95 K in zero field. With increasing magnetic field B, the superconductivity is gradually weakened, and the bridges are finally driven into an insulating state at B = 9 T, as it is shown in Fig. 7.1.

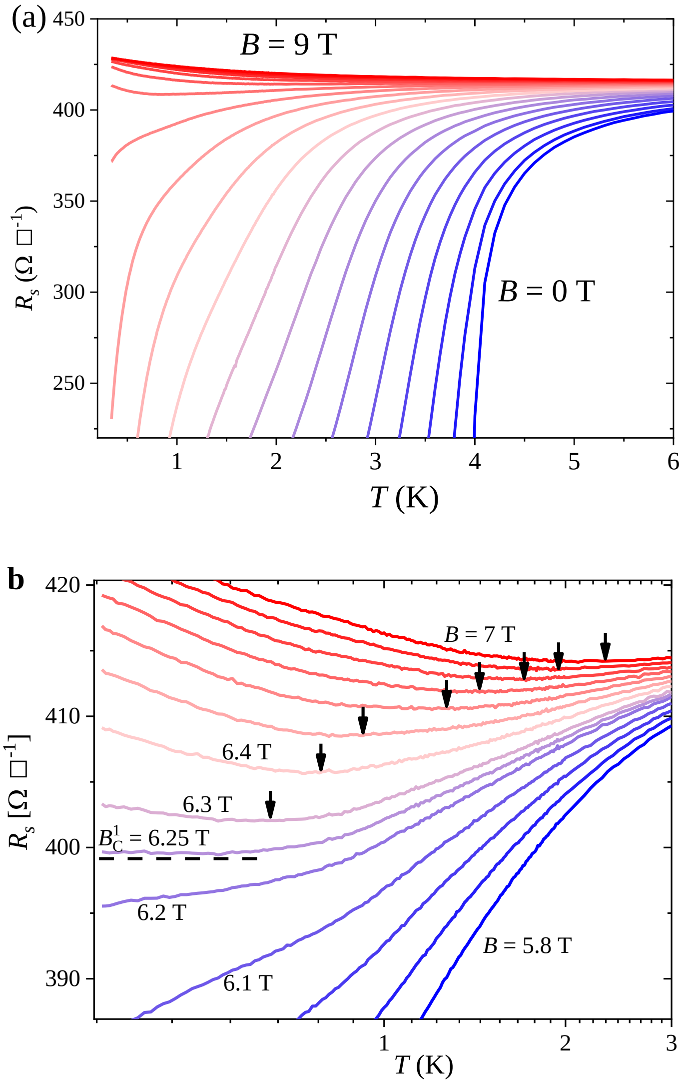

Figure 7.1: Magnetic-field driven superconductor to insulator transition. (a) Sheet resistance R_s as a function of temperature for different magnetic fields from 0 to 9 T in steps of 0.5 T. (b) Detailed $R_s(T)$ data in steps of 0.1 T showing the characteristic magnetic field B_c^1, for which R_s is constant from T~0.6 K down to the zero-temperature limit. The minima in the $R_s(T)$ data,

which define the boundary between the Bose insulating state and the normal phase, are marked with arrows.

Although the T_c is greatly suppressed by the increasing field, a zero temperature superconducting state is still expected at relatively low field. At a critical field $B_c^1 = 6.25$ T, however, the sheet resistance R_s is independent of temperature in the zero-temperature limit, which is a hallmark of a QPT, and the superconducting state is driven into an insulating state, as it is shown in Fig. 7.1 (b).

Figure 7.2(a) shows the magnetoresistance R_s data for temperatures ranging from 0.34 to 0.54 K. The $R_s(B)$ curves clearly exhibit a crossing point at a critical magnetic field ($B_c^1 = 6.25\ \mathrm{T}, R_c^1 = 399.7\ \Omega$). It corresponds to the separatrix with a constant $R_s(T)$ in the zero-temperature limit, thereby defining the QCP in Fig. 7.1(b). This critical point separates the insulating state from the superconducting state, in that $\mathrm{d}R_s/\mathrm{d}T$ changes its sign from superconducting behavior to insulating behavior at different sides of B_c^1. In the critical regime, the $R_s(B,T)$ data should collapse onto a single curve by scaling the abscissa as $|B - B_c^1|t$, where $t = T^{-1/z\nu}$ [306,328]. Here we set t at the lowest investigated temperature as $t(0.34\ \mathrm{K}) = 1$, and all the other data are then collapsed onto $R_s(B, T = 0.34\ \mathrm{K})$ by adjusting t for each temperature T, as it is shown in Fig. 7.2(b). As a result, the critical exponent $z\nu$ can be retrieved by a power-law fit of $t(T)$, which yields $z\nu = 1.33 \sim 4/3$ with high precision on both sides of the SIT (Fig. 7.2(b), inset).

Alternatively, a critical exponent $z\nu \sim 4/3$ can also be obtained from scaling other parameters, such as $T_c(B)$. By carefully checking the $T_c(B)$ dependence in the zero-temperature limit, the QCP ($B_c^1, T = 0$) is very close to the extrapolated end point of the $T_c(B)$ curve (which will be discussed later in chapter 7.5), which is consistent with theoretical expectations [105]. According to general scaling arguments [105,327], the thermodynamic superconducting transition temperature $T_c(B)$ scales in the vicinity of the QCP according to $T_c(B) \propto |B - B_c^1|^{z\nu}$, which we indeed observe with $z\nu \sim 4/3$, as it is shown in Fig. 7.3. We note that this behavior of $T_c(B)$ in the zero temperature limit deviates from the standard BCS expectations, which has also been observed in thin gallium films [328].

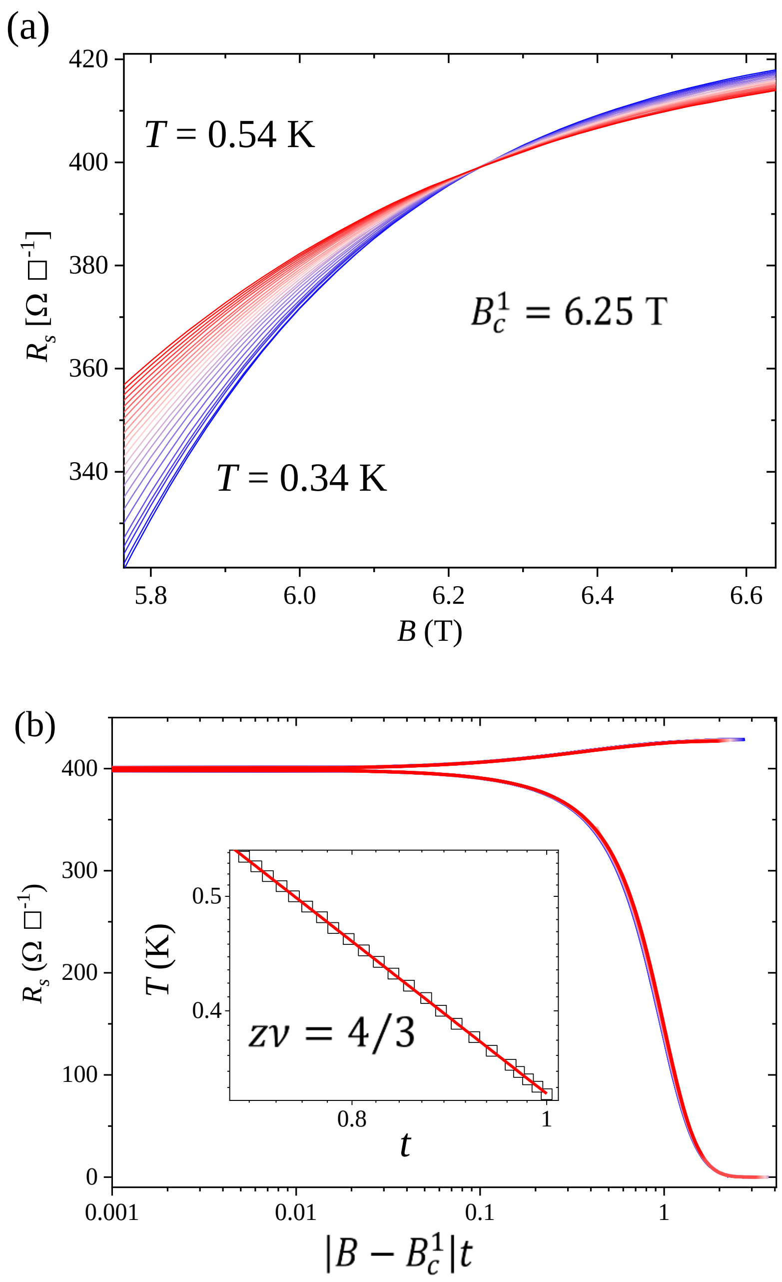

Figure 7.2: Scaling analysis at B_c^1. (a), Sheet resistance R_s as a function of magnetic field B for different temperatures from 0.34 to 0.54 K. The crossing point is at $B_c^1 = 6.25$ T, $R_c^1 = 399.7$ Ω/□. (b), Scaling-analysis plot of R_S as a function of $|B - B_c^1|t$. Inset: temperature dependence of the scaling parameter t, with a power-law fit according to $z\nu = 4/3$ (solid line).

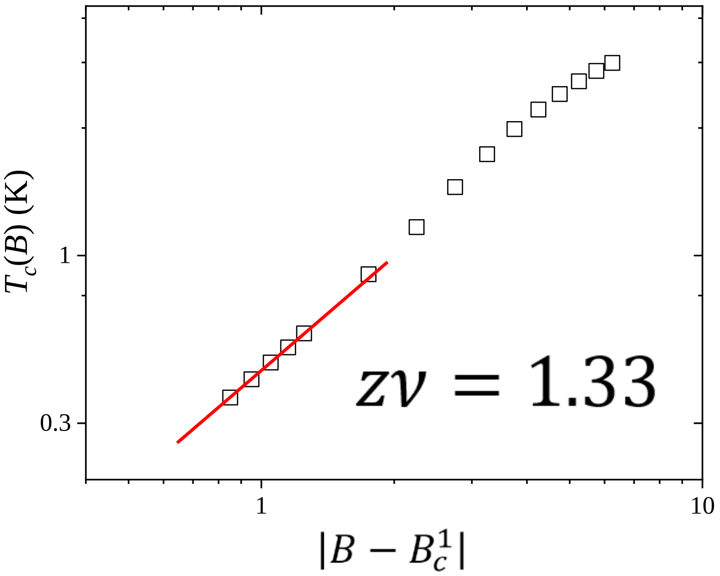

Figure 7.3: Determination of the $z\nu$ by scaling the $T_c(B)$. The $T_c(B)$ data are derived from the $R_s(T)$ curves with a $R_n/2$ standard.

7.3 Critical point near $T_c(0)$

Above the QCP B_c^1, superconducting fluctuations still persist in the system at finite temperatures (Fig. 7.1(a)), but the system is a zero-temperature insulator. At finite temperatures, the $R_s(T)$ data show a minimum, separating the fluctuation dominated region ($\mathrm{d}R_s(T)/\mathrm{d}T > 0$) from the insulating region ($\mathrm{d}R_s(T)/\mathrm{d}T < 0$), thereby defining a phase boundary between the Bose-insulating and the fluctuation dominated normal state (see chapter 7.5). Such finite temperature superconducting fluctuations beyond the superconductor to insulator QPTs have also been observed in amorphous InO$_x$ systems [311], liquid helium-quenched gallium films [330], and quench-condensed ultrathin beryllium films [323]. The superconducting fluctuations above B_c^1 are gradually weakened by increasing the magnetic field until a second critical field ($B_c^2 = 7.3$ T, $R_c^2 = 415.3\ \Omega$) is reached, beyond which the superconducting fluctuations disappear, as it is shown in Fig. 7.4. Inspecting the corresponding $R_s(B,T)$ data in the temperature range from 3 to 5 K (Fig. 7.5(a)) reveals another crossing point at B_c^2, which we interpret as the critical value for Cooper-pair breaking, *i.e.*, the transition to a Fermi insulating state. The scaling analysis in the critical regime of B_c^2, analogous to that we applied at B_c^1, shows an excellent collapse of the $R_s(B,T)$ curves (Fig. 7.5(b)), leading to $z\nu = 0.67 \sim 2/3$ (Fig. 7.5(b), inset).

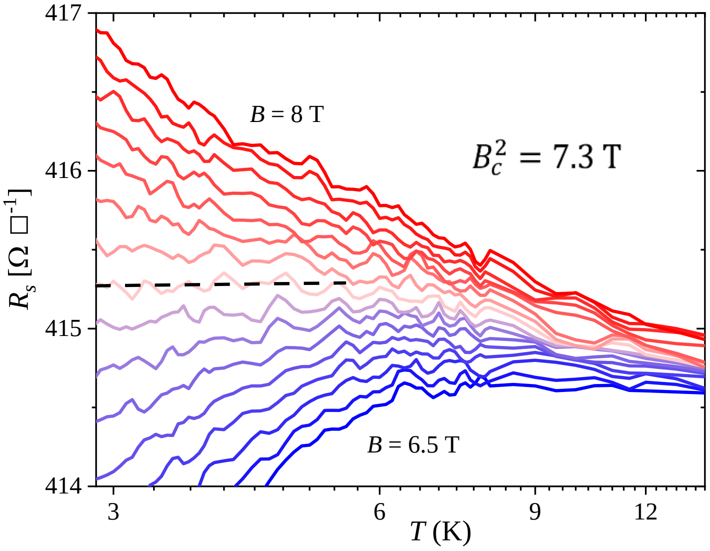

Figure 7.4: Corresponding $R_S(T)$ data for $B > B_c^1$, showing the characteristic magnetic field B_c^2 separating the Bose-insulating state with pronounced superconducting fluctuations, from the Fermi-insulating state.

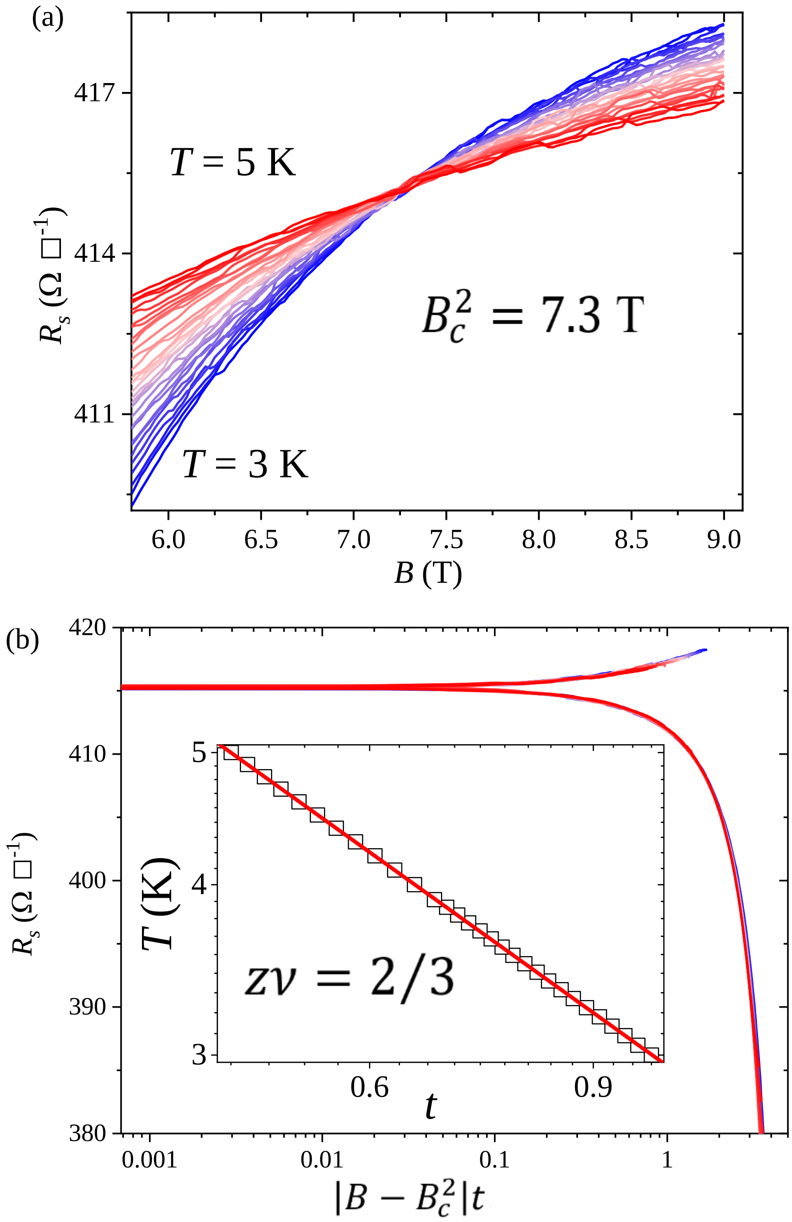

Figure 7.5 Scaling analysis at B_c^2. (a) Sheet resistance R_S as a function of magnetic field B for different temperatures between 3 to 5 K, with a distinct crossing point at ($B_c^2 = 7.3$ T, $R_c^2 = 415.3\ \Omega/\square$). (b) Scaling-analysis plot of R_s as a function of $|B - B_c^2|t$. Inset: temperature dependence of the scaling parameter t, with $z\nu = 2/3$.

7.4 Continuous phase transitions between B_c^1 and B_c^2

For fields $B_c^1 < B < B_c^2$, superconducting fluctuations appear at finite temperatures with $\partial R_S/\partial T > 0$, and the system turns out to be an insulator in the zero-temperature limit with $\partial R_S/\partial T < 0$. The insulating state at low temperatures and the superconducting fluctuating state near $T_c(0)$ are separated by a minimum on the $R_s(T)$ curve, and a critical region formed between these two states. By carefully checking the $R_s(T)$ curves between B_c^1 and B_c^2 in steps of 0.1 T, a critical region where R_s is independent of temperature is identified, and a scaling analysis is performed within this critical region. Figure 7.6 shows a group of representative data at $B = 6.4$ T.

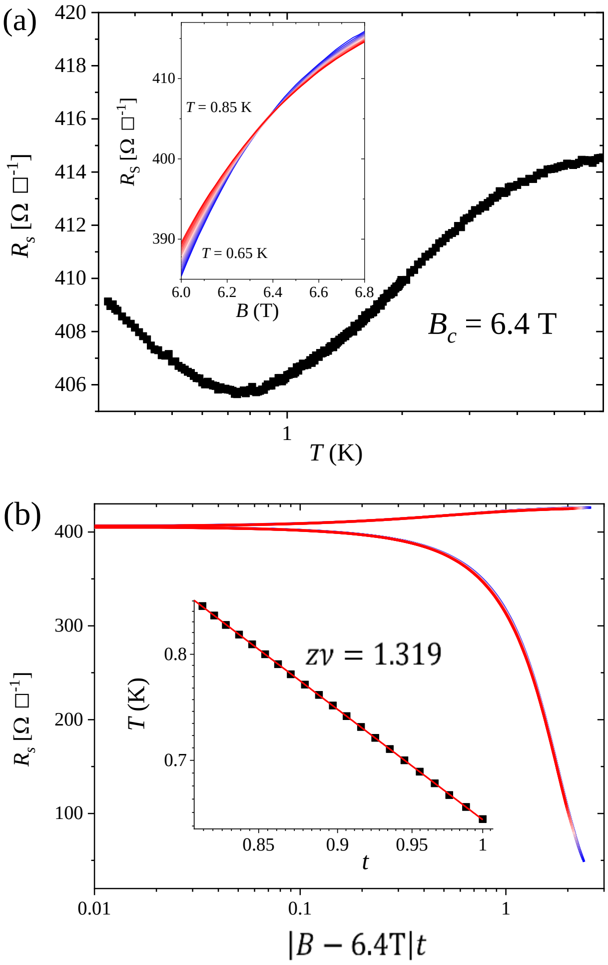

Figure 7.6: A finite temperature critical region at 6.4 T. (a) Critical region defined by the $R_s(T)$. Inset: Critical region defined by the $R_s(B)$. (b) Scaling analysis at 6.4 T and scaling-analysis plot of R_s as a function of $|B - 6.4\mathrm{T}|t$. Inset: temperature dependence of the scaling parameter t, with $z\nu = 1.319$.

Fig. 7.7 shows the field dependence of the critical resistance R_c and that of the resulting product νz. With the increasing field, the critical resistance $R_c(B)$ increases gradually from 399.7 $\Omega/\square$ at B_c^1 to 415.3 $\Omega/\square$ at B_c^2. The critical exponents νz decrease from 4/3 to 2/3.

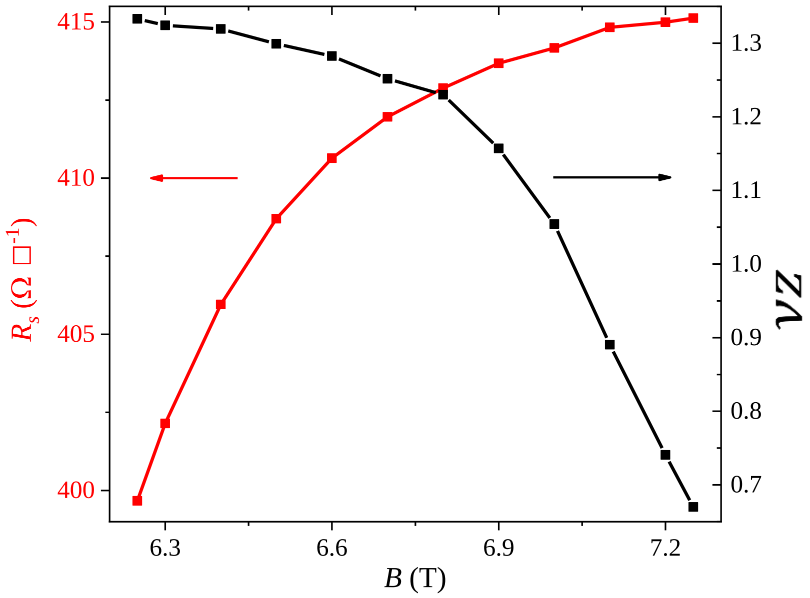

Figure 7.7: Continuous phase transitions between B_c^1 and B_c^2. Magnetic field dependence of the critical resistance R_c and the corresponding critical exponents $z\nu$.

7.5 Phase diagram of the SITs in 2D a-$W_{0.75}Si_{0.25}$

It is natural to interpret our observations in the following way. The perfect scaling behavior down to zero temperature at B_c^1 is clearly consistent with the bosonic description, where Cooper pairs exist on both sides of the superconductor-to-insulator QPT which is driven by quantum phase fluctuations [105,306,308-310,328]. The zero-temperature insulating state is characterized by the loss of global phase coherence. However, superconducting amplitude fluctuations still exist on the insulating side above B_c^1 [331,332]. The physical picture on the insulating side involves localized Cooper pairs and freely moving vortices, forming a bosonic insulating state [306,309,310]. The product $z\nu = 4/3$ is the simplest and most direct manifestation of such a superconductor-to-Bose insulator QPT since it is only depends on the universality class of system. By assuming $z = 1$, $\nu \sim 4/3 > 1$ corresponds to the $T \rightarrow 0$ SIT in 2D disordered systems, as observed in some conventional amorphous superconductors [312,333], two-dimensional electron gases at oxide interfaces [328], ultrathin high-T_c superconductors [308,324], or more recently, in graphene–metal hybrids [334]. The critical sheet resistance $R_c \approx 400\ \Omega$ measured in our amorphous WiSi film at B_c^1 is one order of magnitude smaller than $R_Q \approx 6\ \mathrm{k}\Omega$, however. We note that certain deviations of experimental R_c from the ideal theoretical value R_Q are not uncommon, and can be ascribed to the contribution of a Fermionic channel to the total resistance [312].

Above B_c^1 on the insulating side, the sizeable superconducting fluctuations must be attributed to localized Cooper pairs in superconducting islands. In disordered or even amorphous superconductors which can be rendered into an inhomogeneous state by order-parameter amplitude fluctuations, such superconducting islands can appear in the system in high magnetic fields [306,331,332]. At B_c^2, the localized Cooper pairs are completely destroyed, and a $z\nu \sim 2/3$ transition to Fermi-insulator occurs. Such transitions with $z\nu \sim 2/3$ and driven by a perpendicular magnetic field have also been observed in other conventional 2D films, such as a-NbSi [326], a-bismuth [336], or in $La_{2-x}Sr_xCuO_4$ films [324]. A comparison of our a-WSi with a-NbSi, a-bismuth, and $La_{2-x}Sr_xCuO_4$ (H_1^* in Ref. 324), reveals a very similar behavior with respect to the critical field B_c^2, in which the critical regions are actually located near $T_c(0)$. Other SITs with $z\nu \sim 2/3$ have been found in electrostatically tuned superconducting $LaTiO_3/SrTiO_3$ or $LaAlO_3/SrTiO_3$ interfaces [327,328]. At the $LaTiO_3/SrTiO_3$ interfaces, the global superconductivity is supposed to be determined by the presence of superconducting islands coupled by non-superconducting metallic regions, and the magnetic field driven SIT with $z\nu \sim 2/3$ corresponds to the vanishing of Cooper pairs within the islands [328]. At the electrical field stimulated LaAlO3/SrTiO3 superconducting interfaces, the charge density driven superconductor to Fermi insulator transition with $z\nu \sim 2/3$ at large negative electrical field can be ascribed to the depletion of carriers and breaking of Cooper pairs [327].

The scenarios in which SITs with $z\nu \sim 2/3$ correspond to a phase transition involved with pair breaking are further supported by the magnetic field tuned SITs with varying current bias in 2D beryllium films [323]. At negligible current bias, an SIT with $z\nu \sim 4/3$ is observed, while with a dc current near the zero-field depairing critical currents, the $z\nu$ is driven from $\sim 4/3$ to $\sim 2/3$.

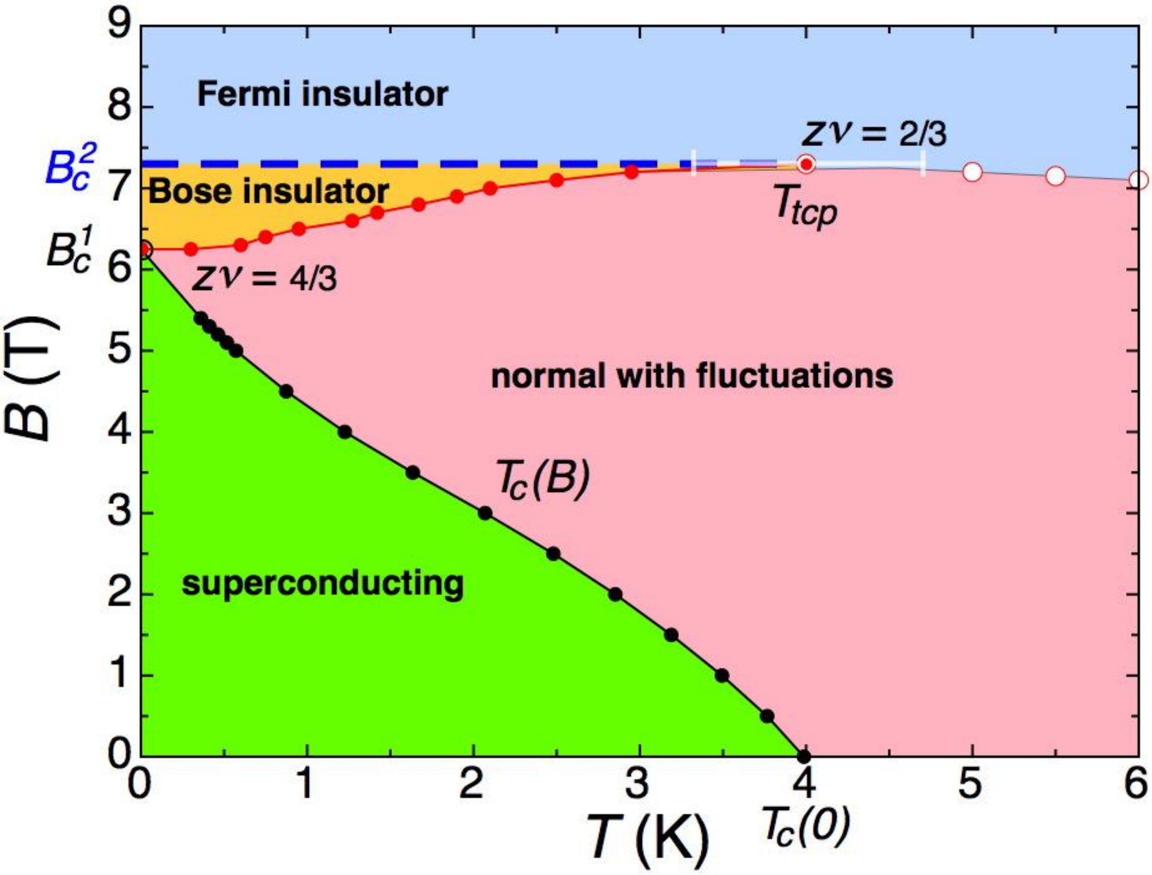

Figure 7.8: Sketch of the superconductor to insulator transition in B-T phase diagram. The boundary between the Bose insulating state and the fluctuation-dominated normal state (filled red cirlces) is determined by the minimum of the $R_s(T)$ curves at different fields between B_c^1 and B_c^2. The separation between the Fermi insulating state and the fluctuation-dominated

normal state (open circles) is defined by the maximum of the $R_s(T)$ curves beyond $T_c(0)$. The tricritical point at T_{tcp} is approximately located at $T_c(0)$, but with a large error margin.

The phase transitions among these distinct states in our WSi films are visualized in the schematic phase diagram in Fig. 7.8. At low field, the superconducting state and the fluctuation-dominated normal region are separated by the $T_c(B)$ line, which we experimentally determined by a $R_n/2$ standard. This $T_c(B)$ line terminates at the QCP B_c^1 in the zero-temperature limit as $T_c(B) \propto |B - B_c^1|^{z\nu}$. At zero temperature, the superconducting and the Bose insulating quantum ground state are separated by the B_c^1. Above B_c^1 and at elevated temperatures, finite temperature transitions between the fluctuation-dominated normal and the Bose insulating states are observed. They end at the second critical field B_c^2 and at a tricritical point around $T_{\text{tcp}} \approx T_c(0) \approx 3.95$ K. At temperatures above T_{tcp}, the fluctuation-dominated state directly crosses over into the Fermi insulating state. At low temperatures, the localized Cooper pairs within the superconducting islands in the Bose insulating state are subsequently destroyed with increasing field, and a Bose insulator to Fermi insulator transition occurs. By carefully comparing the response of the $R_s(B)$ data to the magnetic field near B_c^1 and B_c^2, we state that the crossover between Bose insulating (strong field dependence) and Fermi insulating state (weak field dependence) must correspond to a virtually horizontal line terminating at the tricritical point at T_{tcp} (Fig. 7.8), which characterizes the field B_c^2 as the depairing field of the Cooper pairs.

To investigate the crossover regime between the Bose insulating and the Fermi insulating states down to $T = 0$, we assume that increasing the magnetic field in the Bose insulating state beyond B_c^1 gradually breaks the Cooper pairs within the superconducting islands, resulting in a strong field dependence of $R_s(B)$. By contrast, $R_s(B)$ in the Fermi insulator with localized electrons should exhibit only a weak field dependence, in which $R_s(B)$ is dominated by weak localization effects [244,271-273]. Although the crossover from a strong to a weak field dependence of $R_s(B)$ in Fig. 7.9(a) is obvious, it is difficult to assign a well-defined value of the corresponding crossover field. We therefore consider the second derivative, $\partial^2 R_s/\partial B^2$ (see Fig. 7.9(b)) and state that this quantity is essentially constant above $B_c^2 \approx 7.3$ T for all temperatures considered, while the field variation becomes apparent for $B \lesssim B_c^2$, which appears to be temperature independent. We therefore conclude that the separation between the

Bose and the Fermi insulator in the phase diagram of Fig. 7.8 corresponds to a virtually horizontal line with $B = B_c^2$.

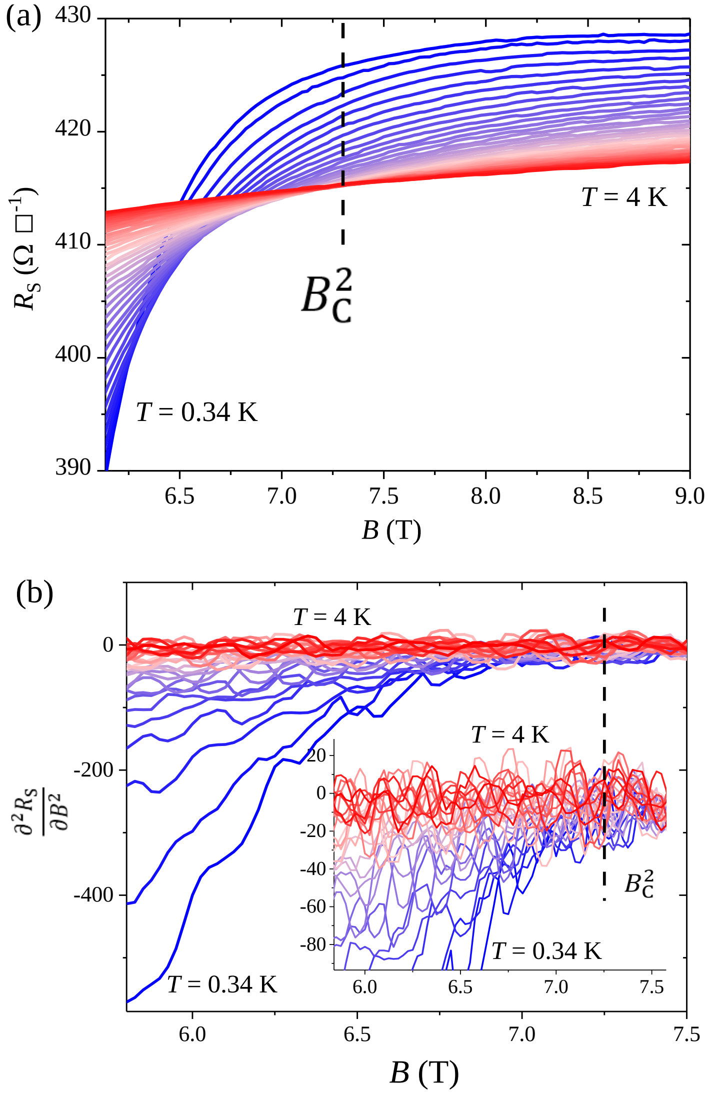

Figure 7.9: (a) Crossover region around B_c^2 between the Bose insulating state and the Fermi insulating state. (b) The second derivative of R_s on B near B_c^2.

8 Conclusions and Outlook

8.1 Hotspot dynamics

We have performed a detailed investigation on amorphous WSi superconductors for the SNSPDs fabrication. From these measurements, we have extracted the material parameters in the superconducting and the normal states. Compared with NbN, the WSi materials have a larger normal-state electron diffusivity, a larger magnetic penetration depth, and a larger superconducting coherence length. The most striking characteristic is that the quasiparticle thermalization time in WSi is much longer than that of NbN, which is most probably due to the amorphous nature of WSi. Moreover, the experimentally determined recovery time of superconductivity in WSi is also one order of magnitude higher than that of NbN.

In the two-stage diffusion model, the formation of the hotspot is controlled by three processes: (1) an initial thermalization of the hot electron which absorbs the incident photon, (2) a subsequent diffusion of the broken Cooper pairs or quasiparticles, and (3) recombination of the non-equilibrium quasiparticles. The hotspot size can therefore be defined by the moment when the amount of the quasiparticles reaches its maximum. Based on our definition, a hotspot diameter of 105 nm is estimated for the 5 nm thick $W_{0.85}Si_{0.15}$ film near the transition temperature, which is perfectly consistent with recent experiments on optical WSi SNSPDs. Moreover, using this definition, we find that the hospot size in a NbN film is only around 25 nm, which also agrees quantitatively with the recent reports. Our definition and interpretation successfully unifies the formation and the evolution of the hotspot both in NbN- and WSi-SNSPDs.

Although we have improved our understanding of the hotspot dynamics in SNSPDs, the detection mechanism in SNSPDs is difficult to examine experimentally and particularly the role of vortices during the single photon detection in SNSPDs needs to be further investigated.

8.2 X-SNSPDs

We successfully fabricated a superconducting single X-ray photon detector based on $W_{0.8}Si_{0.2}$, which is able to be operated up to 4.8 K, just below its critical temperature. The detector starts to react to X-ray photons at very low bias currents, less than 1% of I_c at T = 1.8 K, and it shows a saturated count rate dependence on bias current at all temperatures, indicating a robust optimum internal quantum efficiency . Dark counts are negligible up to the highest bias current (99% of I_c) and operating temperature (4.8 K). Moreover, the WSi X-SNSPD shows a possible energy resolution at an intermediate bias current.

Compared with the previous superconducting single X-ray photon detectors, the WSi X-SNSPD shows an improved detection performance in terms of detection efficiency, dark noise, operating temperature and energy resolving ability. The operating temperature, however, is still too low when compared with the semiconductor detectors. Investigations on high temperature superconductors (such as yttrium barium copper oxide or bismuth strontium calcium copper oxide) for the detector fabrication will be a promissing next step in the future.

8.3 SITs

By studying the magnetoresistance in a perpendicular field configuration, we observed a clear superconductor to insulator phase transition in the 2D WSi films, mediated by quantum fluctuations and by thermal fluctuations. In the zero-temperature limit, a quantum critical region at B_c^1 from ~ 0.6 K down to zero temperature is observed. The sheet resistance near this critical region is perfectly described by a scaling analysis, resulting in a critical exponent products $z\nu \sim 4/3$. This critical behavior and the scaling analysis are consistent with the Bosonic descriptions of SITs. Above the first critical field, superconducting fluctuations still persist in the system up to a second critical field B_c^2, above which the superconducting fluctuations completely disappear. The scaling analysis at B_c^2 indicate a $z\nu \sim 2/3$, which is consistent with the SITs induced by the Cooper pair breaking.

The insulating state between B_c^1 and B_c^2 is identified as a Bose insulator, in which the Cooper pairs are localized. As a result, superconducting fluctuations still exist at finite temperatures. These localized Cooper pairs are finally destroyed at the second critical field B_c^2, which in turn drives the system into a Fermi insulator.

Bibliography

[1] A. Einstein, on a heuristic point of view about the creation and conversion of light, Ann. Phys. (Leipz.) **17**, 132 (1905).

[2] R. H. Hadfield, single-photon detectors for optical quantum information applications, Nat. Photonics **3**, 696 (2009).

[3] M. Ramilli, A. Allevi, V. Chmill, M. Bondani, M. Caccia , and A. Andreoni, *Photon-number statistics with silicon photomultipliers*, J. Opt. Soc. Am. B **27**, 852 (2010).

[4] N. Kanaya, *HPD for linear colliders for the JLC calorimeter group*, Nucl. Instrum. Methods Phys. Res. A **442**, 295 (2000).

[5] P. Buzhan, B. Dolgoshein, L. Filatov, A. Ilyin, V. Kantzerov, V. Kaplin, A. Karakash, F. Kayumov, S. Klemin, E. Popova, and S. Smirnov, *Silicon photomultiplier and its possible applications*, Nucl. Instrum. Methods Phys. Res. A **504**, 48 (2003).

[6] S. Korpar, S. Korpara, R. Dolenec, K. Hara, T. Iijima, P. Križan, Y. Mazuka, R. Pestotnik, A. Stanovnik, and M. Yamaoka, *Silicon photomultiplier as a detector of Cherenkov photons*, Nucl. Instrum. Methods Phys. Res. A **595**, 161 (2008).

[7] S. Moehrs, A. Del Guerra, D. J. Herbert, and M. A. Mandelkern, *A detector head design for small-animal PET with silicon photomultipliers (SiPM)*, Phys. Med. Biol. **51**, 1113 (2006).

[8] E. Grigoriev, A. Akindinov, M. Breitenmoser, S. Buono, E. Charbon, C. Niclass, I. Desforges, and R. Rocca, *Silicon photomultipliers and their bio-medical applications*, Nucl. Instrum. Methods Phys. Res. A **571**, 130 (2007).

[9] D. Fukuda, G. Fujii, T. Numata, A. Yoshizawa, H. Tsuchida, H. Fujino, H. Ishii, T. Itatani, S. Inoue, and T. Zama, *Photon number resolving detection with high speed and high quantum efficiency*, Metrologia **46**, S288 (2009).

[10] D. Kedar and S. Arnon, Subsea ultraviolet solar-blind broadband free-space optics communication, Opt. Eng. **48**, 046001 (2009).

[11] S. Arnon and D. Kedar, *Non-line-of-sight underwater optical wireless communication network*, J. Opt. Soc. Am. A Opt. Image Sci. Vis. **26**, 530 (2009).

[12] B. E. Kardyna, Z. L. Yuan, and A. J. Shields, *An avalanche-photodiode-based photon-number-resolving detector*, Nat. Photonics **2**, 425 (2008).

[13] S. Pellegrini, R.E. Warburton, L. J. J. Tan, Jo Shien Ng, A. B. Krysa, K. Groom, J. P. R. David, S. Cova, M.J. Robertson, and G.S. Buller, *Design and performance of an InGaAs-InP single-photon avalanche diode detector*, IEEE J Quantum Electronics **42**, 397 (2006).

[14] M. Liu, X. Bai, C. Hu, X. Guo, J. C. Campbell, Z. Pan, and M. M. Tashima, *Low dark count rate and high single-photon detection efficiency avalanche photodiode in Geiger-mode operation*, IEEE Photonics Technology Letters **19**, 378 (2007).

[15] R. Sidhu, H. Chen, N. Duan, G. V. Karve, J. C. Campbell and A.L. Holmes, Jr., *GaAsSb resonant-cavity enhanced avalanche photodiode operating at 1.06 µm*. Electron. Lett. **40**, 1296 (2004).

[16] G. N. Gol'tsman, O. Okunev, G. Chulkova, A. Lipatov, A. Semenov, K. Smirnov, B. Voronov, A. Dzardanov, C. Williams, and Roman Sobolewski, *Picosecond superconducting single-photon optical detector*, App. Phys. Lett. **79**, 705 (2001).

[17] S. Somani, S. Kasapi, K. Wilsher, W. Lo, R. Sobolewski, and G. N. Gol'tsman, *New photon detector for device analysis: Superconducting single-photon detector based on a hot electron effect*, J. Vac. Sci. Technol. B **19**(**6**), 2766 (2001).

[18] J. Zhang, W. Slysz, A. Verevkin, O. Okunev, G. Chulkova, A. Korneev, A. Lipatov, G. N. Gol'tsman, and R. Sobolewski, *Response Time Characterization of NbN Superconducting Single-Photon Detectors*, IEEE Trans. Appl. Supercond. **13**, 180 (2003).

[19] F. Marsili, V. B. Verma, J. A. Stern, S. Harrington, A. E. Lita, T. Gerrits, I. Vayshenker, B. Baek, M. D. Shaw, R. P. Mirin, and S. W. Nam, *Detecting single infrared photons with 93% system efficiency*, Nat. Photonics **7**, 210 (2013).

[20] F. Marsili, F. Bellei, F. Najafi, A. E. Dane, E. A. Dauler, R. J. Molnar, and K. K. Berggren, *Efficient single photon detection from 500 nanometer to 5 micron wavelength*. Nano Lett. **12**, 4799 (2012)

[21] L. Zhang, L. Kang, J. Chen, Y. Zhong, Q. Zhao, T. Jia, C. Cao, B. Jin, W. Xu, G. Sun, and P. Wu, *Ultra-low dark count rate and high system efficiency single-photon detectors with 50 nm-wide superconducting wires*, Appl. Phys. B 102, 867 (2011).

[22] H. Shibata, K. Shimizu, H. Takesue, and Y. Tokura, Superconducting Nanowire Single-Photon Detector with Ultralow Dark Count Rate Using Cold Optical Filters, Appl. Phys. Express **6**, 072801 (2013).

[23] F. Najafi, J. Mower, N. C. Harris, F. Bellei, A. Dane, C. Lee, X. Hu, P. Kharel, F. Marsili, S. Assefa, K. K. Berggren, and D. Englund, *On-chip detection of non-classical light by scalable integration of single-photon detectors*, Nat. Commun. **6**, 5873 (2015).

[24] V. B. Verma, B. Korzh, F. Bussie`res, R. D. Horansky, S. D. Dyer, A. E. Lita, I. Vayshenker, F. Marsili, M. D. Shaw, H. Zbinden, R. P. Mirin, and S. W. Nam, *High-efficiency superconducting nanowire single-photon detectors fabricated from MoSi thin-films*, Opt. Express **23**, 33792 (2015).

[25] O. Kahl, S. Ferrari, V. Kovalyuk, G. N. Goltsman, A. Korneev, and W. H. Pernice, Waveguide integrated superconducting single-photon detectors with high internal quantum efficiency at telecom wavelengths, Sci. Rep. **5**, 10941 (2015).

[26] B. S. Robinson, A. J. Kerman, E. A. Dauler, R. O. Barron, D. O. Caplan, M. L. Stevens, J. J. Carney, S. A. Hamilton, J. K. W. Yang, and K. K. Berggren, *781 Mbit/s photon-counting optical communications using a superconducting nanowire detector*, Opt. Lett. **31**, 444 (2006).

[27] S. Chen, D. Liu, W. Zhang, L. You, Y. He, X. Yang, G. Wu, M. Ren, H. Zeng, Z. Wang, X. Xie, and M. Jiang, *Time-of-flight laser ranging and imaging at 1550 nm using low-jitter superconducting nanowire single-photon detection system*, Appl. Opt. **52**(14), 3241–3245 (2013)

[28] K. Takemoto, Y. Nambu, T. Miyazawa, Y. Sakuma, T. Yamamoto, S. Yorozu, and Y. Arakawa, Quantum key distribution over 120 km using ultrahigh purity single-photon source and superconducting single-photon detectors, Sci. Rep. **5**, 14383 (2015).

[29] K. De Greve, L. Yu, P. L. McMahon, J. S. Pelc, C. M. Natarajan, N. Y. Kim, E. Abe, S. Maier, C. Schneider, M. Kamp, S. Ho ̈fling, R. H. Hadfield, A. Forchel, M. M. Fejer, and Y. Yamamoto, *Quantum-dot spin–photon entanglement via frequency downconversion to telecom wavelength*, Nature (London) **491**, 421 (2012).

[30] Y. Tang, H. Yin, S. Chen, Y. Liu, W. Zhang, X. Jiang, L. Zhang, J. Wang, L. You, J. Guan, D. Yang, Z. Wang, H. Liang, Z. Zhang, N. Zhou, X. Ma, T. Chen, Q. Zhang, and Jian-Wei Pan, *Measurement-Device-Independent Quantum Key Distribution over 200 km*, Phys. Rev. Lett. **113**, 190501 (2015).

[31] N. C. Harris, D. Grassani, A. Simbula, M. Pant, M. Galli, T. Baehr-Jones, M. Hochberg, D. Englund, D. Bajoni, and C. Galland, *Integrated Source of Spectrally Filtered Correlated Photons for Large-Scale Quantum Photonic Systems*, Phys. Rev. X **4**, 041047 (2014).

[32] Y.Tang, H. Yin, Q. Zhao, H. Liu, X. Sun, M. Huang, W. Zhang, S. Chen, L. Zhang, L. You, Z. Wang, Y. Liu, C. Lu, X. Jiang, X. Ma, Q. Zhang, T. Chen, and Jian-Wei Pan, *Measurement-Device-Independent Quantum Key Distribution over Untrustful Metropolitan Network*, Phys. Rev. X **6**, 011024 (2016).

[33] S. I. Cherednichenko, P. Yagoubov, K. S. Il’in, G. N. Gol’tsman, and E. M. Gershenzon, *Large bandwidth of NbN phonon-cooled hot-electron bolometer mixers on sapphire substrates*, in Proceedings of the Eighth International Symposium on Space Terahertz Technology (Harvard University, Cambridge, MA, 1997), pp. 245–252.

[34] A. D. Semenov, G. N. Gol’tsman, A. A. Korneev, *Quantum detection by current carrying superconducting film*, Phys. C (Amsterdam) **351**, 349 (2001).

[35] A. Verevkin, J. Zhang, R. Sobolewski, A. Lipatov, O. Okunev, G. Chulkova, A. Korneev, K. Smirnov, G. N. Gol’tsman, and A. Semenov, *Detection efficiency of large-active-area NbN single-photon superconducting detectors in the ultraviolet to near-infrared range*, Appl. Phys. Lett. **80**, 4687 (2002).

[36] G. N. Gol’tsman, K. Smirnov, P. Kouminov, B. Voronov, N. Kaurova, V. Drakinsky, J. Zhang, A. Verevkin, and R. Sobolewski, *Fabrication of Nanostructured Superconducting Single-Photon Detectors*, IEEE Trans. Appl. Supercond. **13**, 192 (2003).

[37] J. Zhang, W. Słysz, A. Pearlman, A. Verevkin, Roman Sobolewski, O. Okunev, G. Chulkova, and G. N. Gol’tsman, *Time delay of resistive-state formation in superconducting stripes excited by single optical photons*, Phys. Rev. B **67**, 132508 (2003).

[38] R. Sobolewski, A. Verevkin, G. N. Gol’tsman, A. Lipatov, and K. Wilsher, *Ultrafast Superconducting Single-Photon Optical Detectors and Their Applications*, IEEE Trans. Appl. Supercond. **13**, 1151 (2003).

[39] J. Yang, E. Dauler, A. Ferri, A. Pearlman, A. Verevkin, G. Gol’tsmann, B. Voronov, R. Sobolewski, W. Keicher, and K. Berggren, *Fabrication Development for Nanowire GHz-Counting-Rate Single-Photon Detectors*, IEEE Trans. Appl. Supercond. **15**, 626 (2005).

[40] A. Pearlman, A. Cross, W. Słysz, J. Zhang, A. Verevkin, M. Currie, A. Korneev, P. Kouminov, K. Smirnov, B. Voronov, G. Gol’tsman, and R. Sobolewski, *Gigahertz Counting Rates of NbN Single-Photon Detectors for Quantum Communications*, IEEE Trans. Appl. Supercond. **15**, 579 (2005).

[41] J. Kitaygorsky, J. Zhang, A. Verevkin, A. Sergeev, A. Korneev, V. Matvienko, P. Kouminov, K. Smirnov, B. Voronov, G. Gol’tsman, and R. Sobolewski, *Origin of Dark Counts in Nanostructured NbN Single-Photon Detectors*, IEEE Trans. Appl. Supercond. **15**, 545 (2005).

[42] A. Semenov, A. Engel, H. W. Hübers, K. Il’in, and M. Siegel, Spectral cut-off in the efficiency of the resistive state formation caused by absorption of a single-photon in current-carrying superconducting nano-strips, Eur. Phys. J. B **47**, 495 (2005).

[43] A. J. Kerman, E. A. Dauler, W. E. Keicher, J. K. W. Yang, K. K. Berggren, G. Gol’tsman, and B. Voronov, *Kinetic-inductance-limited reset time of superconducting nanowire photon counters*, Appl. Phys. Lett. **88**, 111116 (2006).

[44] F. Tafuri, J. R. Kirtley, D. Born, D. Stornaiuolo, P. G. Medaglia, P. Orgiani, G. Balestrino, and V. G. Kogan, *Dissipation in ultra-thin current-carrying superconducting bridges; evidence for quantum tunneling of Pearl vortices*, Europhys. Lett. **73**, 948 (2006).

[45] A. Korneev, V. Matvienko, O. Minaeva, I. Milostnaya, I. Rubtsova, G. Chulkova, K. Smirnov, V. Voronov, G. Gol’tsman, W. Slysz, A. Pearlman, A. Verevkin, and R. Sobolewski, Quantum Efficiency and Noise-Equivalent Power of Nanostructured, NbN, *Single-Photon Detectors in the Wavelength Range from Visible to Infrared*, IEEE Trans. Appl. Supercond. **15**, 571 (2005).

[46] A. Korneev, O. Minaeva, I. Rubtsova, I. Milostnaya, G. Chulkova, B. Voronov, K. Smirnov, V. Seleznev, G. Gol'tsman, A. Pearlman, W. Slysz, A. Cross, P. Alvarez, A. Verevkin, R. Sobolewski, *Superconducting single-photon ultrathin NbN film detector*, Quantum Electron. **35**, 698 (2005)

[47] W. Sysz, M. Wgrzecki, J. Bar, P. Grabiec, M. Górska, V. Zwiller, C. Latta, P. Bohi, I. Milostnaya, O. Minaeva, A. Antipov, O. Okunev, A. Korneev, K. Smirnov, B. Voronov, N. Kaurova, G. Gol’tsman, A. Pearlman, A. Cross, I. Komissarov, A. Verevkin, and R. Sobolewski, *Fiber-coupled single-photon detectors based on NbN superconducting nanostructures for practical quantum cryptography and photon-correlation studies*, Appl. Phys. Lett. **88**, 261113 (2006)

[48] A. Korneev, P. Kouminov, V. Matvienko, G. Chulkova, K. Smirnov, B. Voronov, G. N. Golt’sman, M. Currie, W. Lo, K. Wilsher, J. Zhang, W. Slysz, A. Pearlman, A. Verevkin, and R. Sobolewski, *Sensitivity and gigahertz counting performance of NbN superconducting single-photon detectors*, Appl. Phys. Lett. **84**, 5338 (2004).

[49] K. M. Rosfjord, J. K. W. Yang, E. A. Dauler, A. J. Kerman, V. Anant, B. M. Voronov, G. N. Gol’tsman, and K. K. Berggren, *Nanowire Single-photon detector with an integrated optical cavity and anti-reflection coating*, Opt. Express **14**, 527 (2006).

[50] I. Milostnaya, A. Korneev, I. Rubtsova, V. Seleznev, O. Minaeva, G. Chulkova, O. Okunev, B. Voronov, K. Smirnov, G. Gol’tsman, W. Slysz, M. Wegrzecki, M. Guziewicz, J. Bar, M. Gorska, A. Pearlman, J. Kitaygorsky, A. Cross, and R. Sobolewski, *Superconducting single-photon detectors designed for operation at 1.55-μm telecommunication wavelength*, Journal of Physics: Conference Series **43**, 1334 (2006).

[51] A. J. Kerman, E. A. Dauler, J. K. W. Yang, K. M. Rosfjord, V. Anant, K. K. Berggren, G. N. Gol’tsman, and B. M. Voronov, *Constriction-limited detection efficiency of superconducting nanowire single-photon detectors*, Appl. Phys. Lett. **90**, 101110 (2007).

[52] R. H. Hadfield, P. A. Dalgarno, J. A. O’Connor1, E. Ramsay, R. J. Warburton, E. J. Gansen, B. Baek, M. J. Stevens, R. P. Mirin, and S. W. Nam, *Submicrometer photoresponse mapping of nanowire superconducting single-photon detectors*, Appl. Phys. Lett. **91**, 241108 (2007).

[53] E. Dauler, B. Robinson, A. Kerman, J. Yang, E. Rosfjord, V. Anant, B. Voronov, G. Gol’tsman, and K. Berggren, *Multi-Element Superconducting Nanowire Single-Photon Detector*, IEEE Trans. Appl. Supercond. **17**, 279 (2007).

[54] F. Mattioli, R. Leoni, A. Gaggero, M. G. Castellano, P. Carelli, F. Marsili, and A. Fiore, *Electrical characterization of superconducting single-photon detectors*, J. Appl. Phys. **101**, 054302 (2007).

[55] A. D. Semenov, P. Haas, B. Günther, H.-W. Hübers, K. Il’in, M. Siegel, A. Kirste, J. Beyer, D. Drung, T. Schurig, and A. Smirnov, Supercond. *An energy-resolving superconducting nanowire photon counter*, Sci. Technol. **20**, 919 (2007).

[56] K. Smirnov, A. Korneev, O. Minaeva, A. Divochiy, M. Tarkhov, S. Ryabchun, V. Seleznev, N. Kaurova, B. Voronov, G. Gol’tsman, and S. Polonsky, *Ultrathin NbN film superconducting single-photon detector array*, J. Phys.: Conf. Ser. **61**, 1081 (2007).

[57] G. Gol’tsman, A. Korneev, M. Tarkhov, V. Seleznev, A. Divochiy, O. Minaeva, N. Kaurova, B. Voronov, O. Okunev, G. Chulkova, I. Milostnaya, K. Smirnov, *Middle-Infrared ultrafast superconducting single photon detector, Middle-infrared ultrafast superconducting single photon detector*, In *Infrared and Millimeter Waves, 2007 and the 2007 15th International Conference on Terahertz Electronics. IRMMW-THz. Joint 32nd International Conference on*, pp. 115-116. IEEE, (2007).

[58] G. Gol’tsman, O. Minaeva, A. Korneev, M. Tarkhov, I. Rubtsova, A. Divochiy, I. Milostnaya, G. Chulkova, N. Kaurova, B. Voronov, D. Pan, J. Kitaygorsky, A. Cross, A. Pearlman, I. Komissarov, W. Slysz, M. Wegrzecki, P. Grabiec, and Roman Sobolewski,

Middle-Infrared to Visible-Light Ultrafast Superconducting Single-Photon Detectors, IEEE Trans. Appl. Supercond. **17**, 246 (2007).

[59] J. A. Stern and W. H. Farr, Fabrication and Characterization of Superconducting NbN Nanowire Single Photon Detectors, IEEE Trans. Appl. Supercond. **17**, 306 (2007).

[60] V. Anant, A. J. Kerman, E. A. Dauler, J. K. W. Yang, K. M. Rosfjord, and K. K. Berggren, *Optical properties of superconducting nanowire single-photon detectors*, Opt. Express **16**, 10750 (2008).

[61] B. Baek, J. A. Stern, and S. W. Nam, Superconducting nanowire single-photon detector in an optical cavity for front-side illumination, Appl. Phys. Lett. **95**, 191110 (2009).

[62] X. Hu, C. W. Holzwarth, D. Masciarelli, E. A. Dauler, and, K. K. Berggren, *Efficiently Coupling Light to Superconducting Nanowire Single-Photon Detectors*, IEEE Trans. Appl. Supercond. **19**, 336 (2009).

[63] S. Miki, M. Fujiwara, M. Sasaki, and Z. Wang, *Development of SNSPD System With Gifford-McMahon Cryocooler*, IEEE Trans. Appl. Supercond. **19**, 332 (2009).

[64] X. L. Hu, T. Zhong, J. E. White, E. A. Dauler, F. Najafi, C. H. Herder, F. N. C. Wong, and K. K. Berggren, *Fiber-coupled nanowire photon counter at 1550 nm with 24% system detection efficiency*, Opt. Lett. **34**, 3607 (2009).

[65] E.F.C. Driessen, F.R. Braakman, E.M. Reiger, S.N. Dorenbos, V. Zwiller, and M.J.A. de Dood, *Impedance model for the polarization-dependent optical absorption of superconducting single-photon detectors*, Eur. Phys. J. Appl. Phys. **47**, 10701 (2009).

[66] Z. Yan, M. K. Akhlaghi, J. L. Orgiazzi and A. H. Majedi, Optoelectronic characterization of a fiber-coupled NbN superconducting nanowire single photon detector, J. Mod. Opt. **56**, 380 (2009).

[67] J.-L. F.-X. Orgiazzi and A. H. Majedi, Robust Packaging Technique and Characterization of Fiber-Pigtailed Superconducting NbN Nanowire Single Photon Detectors, IEEE Trans. Appl. Supercond. **19**, 341 (2009).

[68] Z. Wang, S. Miki, and M. Fujiwara, Superconducting Nanowire Single-Photon Detectors for Quantum Information and Communications, IEEE J. Sel. Top. Quantum Electron. **15**, 1741 (2009).

[69] G. Goltsman, A. Korneev, A. Divochiy, O. Minaeva, M. Tarkhov, N. Kaurova, V. Seleznev, B. Voronov, O. Okunev, A. Antipov, K. Smirnov, Yu. Vachtomin, I. Milostnaya and G. Chulkova, *Ultrafast superconducting single-photon detector,* J. Mod. Opt. **56**, 1670 (2009).

[70] M. G. Tanner, C. M. Natarajan, V. K. Pottapenjara, J. A. O'Connor, R. J. Warburton, R. H. Hadfield, B. Baek, S. Nam, S. N. Dorenbos, E. Bermúdez Ureña, T. Zijlstra, T. M. Klapwijk, and V. Zwiller, *Enhanced telecom wavelength single-photon detection with NbTiN superconducting nanowires on oxidized silicon*, Appl. Phys. Lett. **96**, 221109 (2010).

[71] D. Bitauld, F. Marsili, A. Gaggero, F. Mattioli, R. Leoni, S. Jahanmirinejad, F. Lévy, and A. Fiore, *Nanoscale Optical Detector with Single-Photon and Multiphoton Sensitivity*, Nano Lett. **10**, 2977 (2010).

[72] M. Rosticher, F. R. Ladan, J. P. Maneval, S. N. Dorenbos, T. Zijlstra, T. M. Klapwijk, V. Zwiller, A. Lupascu, and G. Nogues, *A high efficiency superconducting nanowire single electron detector*, Appl. Phys. Lett. **97**, 183106 (2010).

[73] S. Miki, T. Yamashita, M. Fujiwara, M. Sasaki, and Z. Wang, *Multichannel SNSPD system with high detection efficiency at telecommunication wavelength*, Opt. Lett. **35**, 2133 (2010).

[74] A. Gaggero, S. J. Nejad, F. Marsili, F. Mattioli, R. Leoni, D. Bitauld, D. Sahin, G. Hamhuis, R. Nötzel, R. Sanjines, and A. Fiore, *Nanowire superconducting single-photon detectors on GaAs for integrated quantum photonic applications*, Appl. Phys. Lett. **97**, 151108 (2010).

[75] S. Miki, T. Yamashita, M. Fujiwara, M. Sasaki, and Z. Wang, Characterization of coupling efficiency and absorption coefficient for fiber-coupled SNSPD with an optical cavity, IEEE Trans. Appl. Supercond. **21**, 332 (2011).

[76] B. Baek, A. E. Lita, V. Verma, and S. W. Nam, Superconducting a-W_xSi_{1-x} nanowire single-photon detector with saturated internal quantum efficiency from visible to 1850 nm, Appl. Phys. Lett. 98, 251105 (2011).

[77] S. N. Dorenbos, P. Forn-Diaz, T. Fuse, A. H. Verbruggen, T. Zijlstra, T. M. Klapwijk, and V. Zwiller, *Low gap superconducting single photon detectors for infrared sensitivity*, Appl. Phys. Lett. **98**, 251102 (2011).

[78] Y. Korneeva, I. Florya, A. Semenov, A. Korneev, and G. Goltsman, *New Generation of Nanowire NbN Superconducting Single-Photon Detector for Mid-Infrared*, IEEE Trans. Appl. Supercond. **21**, 323 (2011).

[79] M. Csete, Á. Sipos, F. Najafi, X. Hu, K.K. Berggren, Numerical method to optimize the polar-azimuthal orientation of infrared superconducting-nanowire singlephoton detectors, Appl. Opt. **50**, 5949 (2011).

[80] T. Yamashita, S. Miki, W. Qiu, M. Fujiwara, M. Sasaki, and Z. Wang, *Performances of Fiber-Coupled Superconducting Nanowire Single-Photon Detectors Measured at Ultralow Temperature*, IEEE Trans. Appl. Supercond. **21**, 336 (2011).

[81] J. P. Sprengers, A. Gaggero, D. Sahin, S. Jahanmirinejad, G. Frucci, F. Mattioli, R. Leoni, J. Beetz, M. Lermer, M. Kamp, S. Höfling, R. Sanjines, and A. Fiore, *Waveguide superconducting single-photon detectors for integrated quantum photonic circuits*, Appl. Phys. Lett. **99**, 181110 (2011).

[82] V. B. Verma, F. Marsili, S. Harrington, A. E. Lita, R. P. Mirin, and S. W. Nam, *A three-dimensional, polarization-insensitive superconducting nanowire avalanche photodetector*, Appl. Phys. Lett. **101**, 251114 (2011).

[83] X. L. Hu, E. A. Dauler, R. J. Molnar, and K. K. Berggren, *Superconducting nanowire single-photon detectors integrated with optical nano-antennae*, Opt. Express **19**, 17 (2011).

[84] G. Bachar, I. Baskin, O. Shtempluck, and E. Buks, Superconducting nanowire single photon detectors on-fiber, Appl. Phys. Lett. **101**, 262601 (2011).

[85] F. Marsili, F. Bellei, F. Najafi, A. E. Dane, E. A. Dauler, R. J. Molnar, and K. K. Berggren, *Efficient Single Photon Detection from 500 nm to 5 μm Wavelength*, Nano Lett. **12**, 4799 (2012).

[86] M. Csete, A. Sipos, A. Szalai, F. Najafi, G. Szabo, and K. K. Berggren, *Improvement of infrared single-photon detectors absorptance by integrated plasmonic structures*, Sci. Rep. **3**, 2406 (2013).

[87] A. Engel, A. Aeschbacher, K. Inderbitzin, A. Schilling, K. Il'in, M. Hofherr, M. Siegel, A. Semenov, and H.-W. Hubers, *Tantalum nitride superconducting single-photon detectors with low cut-off energy*, Appl. Phys. Lett. **100**, 062601 (2011).

[88] D. Henrich, L. Rehm, S. Dörner, M. Hofherr, K. Il'in, A. Semenov, and M. Siegel, *Detection Efficiency of a Spiral-Nanowire Superconducting Single-Photon Detector*, IEEE Trans. Appl. Supercond. **23**, 2200405 (2013).

[89] M. K. Akhlaghi, H. Atikian, J. F. Young, M. Loncar, and A. H. Majedi, *Efficient Single Photon Absorption by Optimized Superconducting Nanowire Geometries*, 2013 13th International Conference on Numerical Simulation of Optoelectronic Devices (NUSOD), (2013).

[90] C. Schuck, W. H. P. Pernice, and H. X. Tang, NbTiN superconducting nanowire detectors for visible and telecom wavelengths single photon counting on Si_3N_4 photonic circuits, Appl. Phys. Lett. **102**, 051101 (2013)

[91] A. Korneev, Y. Korneeva, N. Manova, P. Larionov, A. Divochiy, A. Semenov, G. Chulkova, Y. Vachtomin, K. Smirnov, and G. Goltsman, Recent Nanowire Superconducting Single-Photon Detector Optimization for Practical Applications, IEEE Trans. Appl. Supercond. **23**, 2201204 (2013).

[92] S. Miki, T. Yamashita, H. Terai and Z. Wang, High performance fiber-coupled NbTiN superconducting nanowire single photon detectors with Gifford-McMahon cryocooler, Opt. Express **21**, 10208 (2013).

[93] S. Subashchandran, R. Okamoto, L. Zhang, A. Tanaka, M. Okano, L. Kang, J. Chen, P. Wu, and S. Takeuchi, *Investigation of the Performance of an Ultralow-Dark-Count Superconducting Nanowire Single-Photon Detector*, Jpn. J. Appl. Phys. **52**, 102801 (2013).

[94] T. Yamashita, S. Miki, H. Terai, and Z. Wang, Low-filling-factor superconducting single photon detector with high system detection efficiency, Opt. Express **21**, 27177 (2013).

[95] H. Myoren, S. Taguchi, K. Ohshima, T. Wakatsuki, T. Taino, L. Parlato, and G. P. Pepe, *Performance of Superconducting Single-Photon Detectors Using NbN/NiCu Nanowires*, IEEE Trans. Appl. Supercond. **23**, 2201304 (2013).

[96] R. Cheng, H. Yin, J. Liu, T. Li, H. Cai, Z. Xu, and W. Chen, Photon-Number-Resolving Detector Based on Superconducting Serial Nanowires, IEEE Trans. Appl. Supercond. **23**, 2200309 (2013).

[97] G. Li, S. Wang, X. Chen, and W. Lu, High efficiency and rapid response superconducting NbN nanowire single photon detector based on asymmetric split ring metamaterial, Appl. Phys. Lett. **104**, 231104 (2014).

[98] A. Jafari Salim, A. Eftekharian, and A. Hamed Majedi, High quantum efficiency and low dark count rate in multi-layer superconducting nanowire single-photon detectors, J. Appl. Phys. **115**, 054514 (2014).

[99] X. Yang, H. Li, W. Zhang, L. You, L. Zhang, X. Liu, Z. Wang, W. Peng, X. Xie, and M. Jiang, *Superconducting nanowire single photon detector with on-chip bandpass filter*, Opt. Express **22**, 16267 (2014).

[100] H. Li, L. Zhang, L. You, X. Yang, W. Zhang, X. Liu, S. Chen, Z. Wang, and X. Xie, *Large-sensitive-area superconducting nanowire single-photon detector at 850 nm with high detection efficiency*, Opt. Express **23**, 17301 (2015).

[101] D. Liu, S. Miki, T. Yamashita, L. You, Z. Wang, and H. Terai, Multimode fiber-coupled superconducting nanowire single-photon detector with 70% system efficiency at visible wavelength, Opt. Express **22**, 21167 (2014).

[102] W. J. Zhang, H. Li, L. X. You, Y. H. He, L. Zhang, X.Y. Liu, X. Y. Yang, J. J. Wu, Q. Guo, S. J. Chen, Z. Wang, and X. M. Xie, *Superconducting nanowire single-photon detectors at a wavelength of 940 nm*, AIP Advances **5**, 067129 (2015).

[103] S. Ferrari, O. Kahl, V. Kovalyuk, G. N. Goltsman, A. Korneev, and W. H. P. Pernice, *Waveguide-integrated single- and multi-photon detection at telecom wavelengths using superconducting nanowires*, Appl. Phys. Lett. **106**, 151101 (2014).

[104] X. Zhang, A. Engel, Q. Wang, A. Schilling, A. Semenov, M. Sidorova, H.-W. Hübers, I. Charaev, K. Ilin, and M. Siegel, *Characteristics of superconducting tungsten silicide* W_xSi_{1-x} *for single photon detection*, Phys. Rev. B **94**, 174509 (2016).

[105] V. F. Gantmakher and V. T. Dolgopolov, *Superconductor-insulator quantum phase transition*, Physics Uspekhi **53**, 1 (2010).

[106] L. E. Toth, Transition Metal Carbides and Nitrides Ch. 7 (Academic Press, 1971).

[107] R. E. de Lamaestre, P. Odier, E. Bellet-Amalric, P. Cavalier, S. Pouget, and J.-C. Villegier, *High Quality Ultrathin NbN Layers On Sapphire for Superconducting Single Photon Detectors*, J. Phys.: Conf. Ser. **97**, 012046 (2008).

[108] S. Miki, M. Fujiwara, M. Sasaki, B. Baek, A. J. Miller, R. H. Hadfield, S. W. Nam, and Z. Wang, *Large sensitive-area NbN nanowire superconducting single-photon detectors fabricated on single-crystal MgO substrates*, Appl. Phys. Lett. **92**, 061116 (2008).

[109] S. Miki, M. Fujiwara, M. Sasaki, and Z. Wang, *NbN Superconducting Single-Photon Detectors Prepared on Single-Crystal MgO Substrates*, IEEE Trans. Appl. Supercond. **17**, 285 (2007).

[110] F. Marsili, D. Bitauld, A. Fiore, A. Gaggero, F. Mattioli, R. Leoni, M. Benkahoul, F. Levy, High efficiency NbN nanowire superconducting single photon detectors fabricated on MgO substrates from a low temperature process, Opt. Express **16**, 3191 (2008).

[111] D. Bitaulda, F. Marsilia,b, A. Fiorea, A. Gaggeroc, F. Mattiolic, R. Leonic, M. Benkahoulb and F. Levy, *NbN nanowire superconducting single photon detectors fabricated on MgO substrates*, J. Mod. Opt. **56**, 395 (2009).

[112] K. Iizuka, K. Matsumaru, T. Suzuki, H. Hirose, K. Suzuki, and H. Okamoto, Arsenic-free GaAs substrate preparation and direct growth of GaAs/AlGaAs multiple quantum well without buffer layer, J. Cryst. Growth **150**, 13 (1995).

[113] F. Marsili, A. Gaggero, L. H. Li, A. Surrente, R. Leoni, F. Levy, and A. Fiore, *High quality superconducting NbN thin films on GaAs*, Supercond. Sci. Technol. **22**, 095013 (2009).

[114] G. Reithmaier, J. Senf, S. Lichtmannecker, T. Reichert, F. Flassig, A. Voss, R. Gross, and J. J. Finley, *Optimisation of NbN thin films on GaAs substrates for in-situ single photon detection in structured photonic devices*, J. Appl. Phys. **113**, 143507 (2013).

[115] D. Sahin, A. Gaggero, J.-W. Weber, I. Agafonov, M. A. Verheijen, F. Mattioli, J. Beetz, M. Kamp, S. Hofling, M. C. M. van de Sanden, R. Leoni, and A. Fiore, *Waveguide Nanowire Superconducting Single-Photon Detectors Fabricated on GaAs and the Study of Their Optical Properties*, IEEE Trans. Appl. Supercond. **21**, 3800210 (2015).

[116] J. Zhang, X. Su, L. Zhang, L. Zheng, X. Wang and L. You, Improvement of the superconducting properties of NbN thin film on single-crystal silicon substrate by using a TiN buffer layer, Supercond. Sci. Technol. **26**, 045010 (2013).

[117] M. G. Tanner, L. S. E. Alvarez, W. Jiang, R. J. Warburton, Z. H. Barber, and R. H. Hadfield, *A superconducting nanowire single photon detector on lithium niobate*, Nanotechnology **23**, 505201 (2012).

[118] S. N. Dorenbos, E. M. Reiger, U. Perinetti, V. Zwiller, T. Zijlstra, and T. M. Klapwijk, *Low noise superconducting single photon detectors on silicon*, Appl. Phys. Lett. **93**, 131101 (2008).

[119] N. N. Iosad, B. D. Jackson, S. N. Polyakov, P. N. Dmitriev, and T. M. Klapwijk, Reactive magnetron sputter-deposition of NbN and (Nb, Ti)N films related to sputtering source characterization and optimization, J. Vac. Sci. Technol. A **19**, 1840 (2001).

[120] S. Miki, M. Takeda, M. Fujiwara1, M. Sasaki1, A. Otomo, and Z. Wang, *Superconducting NbTiN Nanowire Single Photon Detectors with Low Kinetic Inductance*, Appl. Phys. Express **2**, 075002 (2009).

[121] C. N. Lau, N. Markovic, M. Bockrath, A. Bezryadin, and M. Tinkham, *Quantum phase slips in superconducting nanowires*, Phys. Rev. Lett. **87**, 217003 (2001).

[122] J. M. Graybeal, P. M. Mankiewich, R. C. Dynes, and M. R. Beasley, *Apparent Destruction of Superconductivity in the Disordered One-Dimensional Limit*, Phys. Rev. Lett. **59**, 2697 (1987).

[123] V. B. Verma, B. Korzh, F. Bussières, R. D. Horansky, A. E. Lita, F. Marsili, M. D. Shaw, H. Zbinden, R. P. Mirin, and S. W. Nam, *High-efficiency WSi superconducting nanowire single-photon detectors operating at 2.5 K*, Appl. Phys. Lett. **105**, 122601 (2014).

[124] V. B. Verma, A. E. Lita, M. R. Vissers, F. Marsili, D. P. Pappas, R. P. Mirin, and S. W. Nam, *Superconducting nanowire single photon detectors fabricated from an amorphous Mo0.75Ge0.25 thin film*, Appl. Phys. Lett. **105**, 022602 (2014).

[125] Y. P. Korneeva, M. Y. Mikhailov, Y. P. Pershin, N. N. Manova, A. V. Divochiy, Y. B. Vakhtomin, A. A. Korneev, K. V. Smirnov, A. G. Sivakov, A. Y. Devizenko, and G. N. Goltsman, *Superconducting single-photon detector made of MoSi film*, Supercond. Sci. Technol. **27**, 095012 (2014).

[126] M. Caloz, B. Korzh, N. Timoney, M. Weiss, S. Gariglio, R. J. Warburton, C. Schönenberger, J. Renema, H. Zbinden, and F. Bussières, *Optically probing the detection mechanism in a molybdenum silicide superconducting nanowire single-photon detector*, Appl. Phys. Lett. **110**, 083106 (2017)

[127] A. J. Annunziata, D. F. Santavicca, J. D. Chudow, L. Frunzio, M. J. Rooks, A. Frydman, and D. E. Prober, *Niobium Superconducting Nanowire Single-Photon Detectors*, IEEE Trans. Appl. Supercond. **19**, 327 (2009).

[128] E. Monticone, C. Portesi, S. Borini, E. Taralli, and M. Rajteri, *Superconducting MgB_2 Nanostructures Fabricated by Electron Beam Lithography*, IEEE Trans. Appl. Supercond. **17**, 222 (2007).

[129] H. Shibata, T. Maruyama, T. Akazaki, H. Takesue, T. Honjo, Y. Tokura, *Photon detection and fabrication of MgB_2 nanowire*, Physica C **468**, 1992 (2008).

[130] H. Shibata, M. Asahi, T. Maruyama, T. Akazaki, H. Takesue, T. Honjo, and Y. Tokura, *Optical Response and Fabrication of MgB_2 Nanowire Detectors*, IEEE Trans. Appl. Supercond. **19**, 358 (2009).

[131] H. Shibata, H. Takesue, T. Honjo, T. Akazaki, and Y. Tokura, *Single-photon detection using magnesium diboride superconducting nanowires*, Appl. Phys. Lett. **97**, 212504 (2010).

[132] F. Marsili, D. P. Cunnane, R. M. Briggs, A. D. Beyer, M. D. Shaw, B. S. Karasik, M. A. Wolak, N. Acharya, and X. X. Xi, *Superconducting nanowire detectors based on MgB_2*, 2015 Conference on Lasers and Electro-Optics (CLEO).

[133] K. Taguchi and J. S. Iwanczyk, Vision 20/20: Single photon counting x-ray detectors in medical imaging, Med. Phys. **40**, 100901 (2013).

[134] X. Wang, D. Meier, K. Taguchi, D. J. Wagenaar, B. E. Patt, and E. C. Frey, *Material separation in x-ray CT with energy resolved photon-counting detectors*, Med. Phys. **38**, 1534 (2011).

[135] H. N. Chapman, A. Barty, M. J. Bogan, S. Boutet, M. Frank, S. P. HauRiege, S. Marchesini, B. W. Woods, S. Bajt, W. H. Benner, R. A. London, E. Plönjes, M. Kuhlmann, R. Treusch, S. Düsterer, T. Tschentscher, J. R. Schneider, E. Spiller, T. Möller, C. Bostedt, M. Hoener, D. A. Shapiro, K. O. Hodgson, D. van der Spoel, F. Burmeister, M. Bergh, C. Caleman, G. Huldt, M. M. Seibert, F. R. N. C. Maia, R. W. Lee, A. Szöke, N. Timneanu, and J. Hajdu, *Femtosecond diffractive imaging with a soft-X-ray free-electron laser*, Nat. Phys. **2**, 839 (2006).

[136] Q. Yang, W. Cong, Y. Xi, and G, Wang, Spectral x-ray CT image reconstruction with a combination of energy-integrating and photon-counting detectors, PLoS ONE **11**, e0155374 (2016).

[137] R. K. Swank, *Absorption and noise in x-ray phosphors*, J. Appl. Phys. **44**, 4199 (1973).

[138] K. Taguchi, S. Srivastava, H. Kudo, and W. C. Barber, *Enabling photon counting clinical x-ray CT*, 2009 IEEE NSS/MIC, 3581 (2010).

[139] W. C. Barber, E. Nygard, J. S. Iwanczyk, M. Zhang, E. C. Frey, B. M. W. Tsui, J. C. Wessel, N. Malakhov, G. Wawrzyniak, N. E. Hartsough, T. Gandhi, and K. Taguchi, *Characterization of a novel photon counting detector for clinical CT: count rate, energy resolution, and noise performance*, Proc. of SPIE **7258**, 725824 (2009).

[140] A. Rack, S. Zabler, B. R. Müller, H. Riesemeier, G. Weidemann, A. Lange, J. Goebbels, M. Hentschel, and W. Görner, *High resolution synchrotron-based radiography and tomography using hard X-rays at the BAMline (BESSY II),* Nucl. Instr. and Meth. A **586**, 327 (2008).

[141] A. Rack, T. Weitkamp, S. Bauer Trabelsi, P. Modregger, A. Cecilia, T. dos Santos Rolo, T. Rack, D. Haas, R. Simon, R. Heldele, M. Schulz, B. Mayzel, A.N. Danilewsky, T. Waterstradt, W. Diete, H. Riesemeier, B.R. Müller, and T. Baumbach, *The micro-imaging station of the TopoTomo beamline at the ANKA synchrotron light source*, Nucl. Instr. and Meth. B **267**, 1978 (2009).

[142] J. C. Labiche, O. Mathon, S. Pascarelli, M. A. Newton, G. G. Ferre, C. Curfs, G. Vaughan, A. Homs, and D. F. Carreiras, Invited article: The fast readout low noise camera as a versatile x-ray detector for time resolved dispersive extended x-ray absorption fine structure and diffraction, Rev. Sci. Instrum. **78**, 091301 (2007).

[143] I. Kantor, J. - C. Labiche, E. Collet, L. Siron, J. - J. Thevenin, C. Ponchut, J. Borrel, T. Mairs, C. Marini, C. Strohm, O. Mathon, and S. Pascarelli, *A new detector for sub-millisecond EXAFS spectroscopy at the European Synchrotron Radiation Facility*, J. Synchrotron Rad. **21**, 1240 (2014).

[144] J. Iwanczyk, W. M. Szymczyk, and M. Traczyk, *X-ray fluoroscence escape peaks in gamma-ray spectra detected by CdTe detectors*, Nucl. Instrum. Methods Phys. Res. **165**, 289 (1979).

[145] V. B. Cajipe, R. F. Calderwood, M. Clajus, S. Hayakawa, R. Jayaraman, T. O. Tumer, B. Grattan, and O. Yossifor, *Multi-energy x-ray imaging with linear CZT pixel arrays and integrated electronics*, Nuclear Science Symposium Conference Record **7**, 4548 (2004).

[146] M. Aslund, B. Cederstrom, M. Lundqvist, and M. Danielsson, Physical characterization of a scanning photon counting digital mammography system based on Si-strip detectors, Med. Phys. **34**, 1918 (2007).

[147] E. Beuville, R. Cahn, B. Cederstrom, M. Danielsson, A. Hall, B. Hasegawa, L. Luo, M. Lundqvist, D. Nygren, E. Oltman, and J. Walton, *High resolution x-ray imaging using a silicon strip detector*, IEEE Trans. Nucl. Sci. **45**, 3059 (1998).

[148] G. Zentai, L. D. Partain, R. Pavlyuchkova, C. H. Proano, M. M. Schieber, and J. Thomas, *Dark current, sensitivity, and image lag comparison of mercuric iodide and lead iodide x-ray imagers*, Proc. SPIE **5541**, 171 (2004).

[149] N. E. Hartsough, J. S. Iwanczyk, E. Nygard, N. Malakhov, W. C. Barber, and T. Gandhi, *Polycrystalline mercuric iodide films on CMOS readout arrays*, IEEE Trans. Nucl. Sci. **56**, 1810 (2009).

[150] G. Bertuccio, C. Canali, and F. Nava, *Energy resolution in GaAs X-and γ-ray detectors*, Nucl. Instrum. Methods Phys. Res. A **410**, 29 (1998).

[151] 1A. Owens, M. Bavdaz, S. Kraft, A. Peacock, H. Andersson, S. Nennonen, M. Gagliardi, T. Gagliardi, F. Scholtz, and G. Ulm, *X-ray response of epitaxial GaAs,* J. Appl. Phys. **85**, 7522 (1999).

[152] J. S. Iwanczyk, E. Nygard, O. Meirav, J. Arenson, W. C. Barber, N. E. Hartsough, N. Malakhov, and J. C. Wessel, *Photon counting energy dispersive detector arrays for x-ray imaging*, IEEE Trans. Nucl. Sci. 56, 535 (2009).

[153] J. P. Schlomka, E. Roessl, R. Dorscheid, S. Dill, G. Martens, T. Istel, C. Baumer, C. Herrmann, R. Steadman, G. Zeitler, A. Livne, and R. Proksa, *Experimental feasibility of multi-energy photon-counting Kedge imaging in pre-clinical computed tomography*, Phys. Med. Biol. **53**, 4031 (2008).

[154] S. Feuerlein, E. Roessl, R. Proksa, G. Martens, O. Klass, M. Jeltsch, V. Rasche, H.-J. Brambs, M. H. K. Hoffmann, and J.-P. Schlomka, *Multienergy photon-counting K-edge imaging: Potential for improved luminal depiction in vascular imaging*, Radiology **249**, 1010 (2008).

[155] Y. Tomita, Y. Shirayanagi, S. Matsui, T. Aoki, and Y. Hatanaka, *X-ray color scanner with multiple energy discrimination capability*, Proc. SPIE **5922**, 59220A (2005).

[156] R. Ballabriga, M. Campbell, E. H. M. Heijne, X. Llopart, and L. Tlustos, The medipix3 prototype, a pixel readout chip working in single photon counting mode with improved spectrometric performance, IEEE Trans. Nucl. Sci. **54**, 1824 (2007).

[157] E. Kraft, P. Fischer, M. Karagounis, M. Koch, H. Krueger, I. Peric, N. Wermes, C. Herrmann, A. Nascetti, M. Overdick, and W. Ruetten, *Counting and integrating readout for direct conversion x-ray imaging: Concept, realization and first prototype measurements*, IEEE Trans. Nucl. Sci. **54**, 383 (2007).

[158] R. Steadman, C. Herrmann, O. Mulhens, D. G. Maeding, J. Colley, T. Firlit, R. Luhta, M. Chappo, B. Harwood, and D. Kosty, *ChromAIX: A high-rate energy-resolving photon-counting ASIC for spectral computed tomography*, Proc. SPIE **7622**, 762220 (2010).

[159] F. Rupcich and T. Gilat-Schmidt, Experimental study of optimal energy weighting in energy-resolved CT using a CZT detector, Proc. SPIE **8668**, 86681X (2013).

[160] C. Xu, M. Danielsson, S. Karlsson, C. Svensson, and H. Bornefalk, Performance characterization of a silicon strip detector for spectral computed tomography utilizing a laser testing system, Proc SPIE **7961**, 79610S (2011).

[161] E. Fredenberg, M. Hemmendorff, B. Cederstrom, M. Aslund, and M. Danielsson, Contrast-enhanced spectral mammography with a photon-counting detector, Med. Phys. **37**, 2017 (2010).

[162] E. Fredenberg, M. Lundqvist, B. Cederström, M. Åslund, and M. Danielsson, *Energy resolution of a photon-counting silicon strip detector*, Nucl. Instrum. Methods Phys. Res. A **613**, 156 (2010).

[163] C. Xu, M. Danielsson, S. Karlsson, C. Svensson, and H. Bornefalk, *Preliminary evaluation of a silicon strip detector for photon-counting spectral CT*, Nucl. Instrum. Methods Phys. Res. A **677**, 45 (2012).

[164] S. Kappler, T. Hannemann, E. Kraft, B. Kreisler, D. Niederloehner, K. Stierstorfer, and T. Flohr, *First results from a hybrid prototype CT scanner for exploring benefits of quantum-counting in clinical CT*, Proc. SPIE **8313**, 83130X (2012).

[165] E. N. Gimenez, R. Ballabriga, M. Campbell, I. Horswell, X. Llopart, J. Marchal, K. J. S. Sawhney, N. Tartoni, and D. Turecek, *Characterization of medipix3 with synchrotron radiation*, IEEE Trans. Nucl. Sci. **58**, 323 (2011).

[166] C. Xu, H. Chen, M. Persson, S. Karlsson, M. Danielsson, C. Svensson, and H. Bornefalk, *Energy resolution of a segmented silicon strip detector for photon-counting spectral CT*, Nucl. Instrum. Methods Phys. Res. A **715**, 11 (2013).

[167] C. Xu, M. Danielsson, and H. Bornefalk, Evaluation of energy loss and charge sharing in cadmium telluride detectors for photon-counting computed tomography, IEEE Trans. Nucl. Sci. **58**, 614 (2011).

[168] C. Xu, M. Persson, C. Han, S. Karlsson, M. Danielsson, C. Svensson, and H. Bornefalk, *Evaluation of a second-generation ultra-fast energyresolved ASIC for photon-counting spectral CT*, IEEE Trans. Nucl. Sci. 60, 437 (2013).

[169] A. Lempicki, C. Brecher, P. Szupryczynski, H. Lingertat, V. V. Nagarkar, S. V. Tipnis and S. R. Miller, *A new lutetia-based ceramic scintillator for X-ray imaging*, Nucl. Instrum. Methods A **488**, 579 (2002).

[170] M. Nikl, *Scintillation detectors for x-rays*, Meas. Sci. Technol. **17**, R37 (2006).

[171] A. Gabutti, R. G. Wagner, K. E. Gray, R. T. Kampwirth, and R. H. Ono, *Superconducting detector for minimum ionizing particles*, Nucl. Instrum. Methods Phys. Res. A, Accel. Spectrom. Detect. Assoc. Equip. **A278**, 425 (1989).

[172] A. Gabutti, K. E. Gray, R. G. Wagner, and R. H. Ono, *Granular aluminum superconducting detector for 6 keV X-rays and 2.2 MeV beta sources*, Nucl. Instrum. Methods Phys. Res. A **289**, 274 (1990).

[173] A. Gabutti, K. E. Gray, G. M. Pugh, and R. Tiberio, *Improved beta detection efficiency with granular aluminum superconducting strips*, Nucl. Instrum. Methods A **306**, 220 (1991).

[174] A. Gabutti, K. E. Gray, G. M. Pugh, and R. Tiberio, *A fast, self-recovering superconducting strip particle detector made with granular tungsten*, Nucl. Instrum. Methods A **312**, 475 (1992).

[175] K. Suzuki, S. Miki, Z. Wang, Y. Kobayashi, S. Shiki, and M. Ohkubo, *Superconducting NbN Thin-Film Nanowire Detectors for Time-of-Flight Mass Spectrometry*, J. Low Temp. Phys. **151**, 766 (2008).

[176] K. Suzuki, S. Miki, S. Shiki, Z. Wang, and M. Ohkubo, Time Resolution Improvement of Superconducting NbN Stripline Detectors for Time-of-Flight Mass Spectrometry, Appl. Phys. Express **1**, 031702 (2008).

[177] N. Zen, A. Casaburi, S. Shiki, K. Suzuki, M. Ejrnaes, R. Cristiano, and M. Ohkubo, *1 mm ultrafast superconducting stripline molecule detector*, Appl. Phys. Lett. **95**, 172508 (2009).

[178] A. Casaburi, N. Zen, K. Suzuki, M. Ejrnaes, S. Pagano, R. Cristiano, and M. Ohkubo, *Subnanosecond time response of large-area superconducting stripline detectors for keV molecular ions*, Appl. Phys. Lett. **94**, 212502 (2009).

[179] N. Zen, Y. Chen, K. Suzuki, M. Ohkubo, S. Miki, and Z. Wang, *Development of Superconducting Strip Line Detectors (SSLDs) for Time-of-Flight Mass Spectrometers (TOF-MS)*, IEEE Trans. Appl. Supercond. **19**, 354 (2009).

[180] B. V. Estey, J. A. Beall, G. C. Hilton, K. D. Irwin, D. R. Schmidt, J. N. Ullom, and R. E. Schwall, *Time-of-Flight Mass Spectrometry With Latching Nb Meander Detectors*, IEEE Trans. Appl. Supercond. **19**, 382 (2009).

[181] M. Marksteiner, A. Divochiy, M. Sclafani, P. Haslinger, H. Ulbricht, A. Korneev, A. Semenov, G. Gol'tsman and M. Arndt, *A superconducting NbN detector for neutral nanoparticles*, Nanotechnology **20**, 455501 (2009).

[182] K. Suzuki, S. Shiki, M. Ukibe, M. Koike, S. Miki1, Z. Wang, and M. Ohkubo, *Hot-Spot Detection Model in Superconducting Nano-Stripline Detector for keV Ions*, Appl. Phys. Express **4**, 083101 (2011).

[183] A. Casaburi, M. Ejrnaes, N. Zen, M. Ohkubo, S. Pagano, and R. Cristiano, *Thicker, more efficient superconducting strip-line detectors for high throughput macromolecules analysis*, Appl. Phys. Lett. **98**, 023702 (2011).

[184] A. Casaburi, E. Esposito, M. Ejrnaes, K. Suzuki, M. Ohkubo, S. Pagano, and R. Cristiano, *A 2×2 mm^2 superconducting strip-line detector for high-performance time-of-flight mass spectrometry*, Supercond. Sci. Technol. **25**, 115004 (2012).

[185] R. Cristiano, M. Ejrnaes, A. Casaburi, N. Zen and M. Ohkubo, *Superconducting nano-strip particle detectors*, Supercond. Sci. Technol. **28**, 124004 (2015).

[186] D. Perez de Lara, M. Ejrnaes, A. Casaburi, M. Lisitskiy, R. Cristiano, S. Pagano, A. Gaggero, R. Leoni, G. Golt'sman, and B. Voronov, *Feasibility Investigation of NbN Nanowires as Detector in Time-of-Flight Mass Spectrometers for Macromolecules of Interest in Biology (Proteins)*, J. Low Temp. Phys. **151**, 771 (2008).

[187] K. Inderbitzin, A. Engel, A. Schilling, K. Il'in, and M. Siegel, *An ultra-fast superconducting Nb nanowire single-photon detector for soft x-rays*, Appl. Phys. Lett. **101**, 162601 (2012).

[188] K. Inderbitzin, A. Engel, and A. Schilling, *Soft X-Ray Single-Photon Detection With Superconducting Tantalum Nitride and Niobium Nanowires*, IEEE Trans. Appl. Supercond. **23**, 2200505 (2013).

[189] X. Zhang, Q. Wang, and A. Schilling, *Superconducting single X-ray photon detector based on $W_{0.8}Si_{0.2}$*, AIP Advances **6**, 115104 (2016).

[190] Jiaguo Zhang, X-ray Radiation Damage Studies and Design of a Silicon Pixel Sensor for Science at the XFEL. PhD thesis, Universität Hamburg, 2013.

[191] A. Casaburi, Superconducting Strip-Lines for Mass Spectrometry: Development and Characterization of Innovative SC Detectors for Unprecedented Performances in Time-Of-Flight Mass Spectrometry (Saarbruchen: Lambert Academic), (2010).

[192] R. Gaudio, K. P. M. op't Hoog, Z. Zhou, D. Sahin, and A. Fiore, *Inhomogeneous critical current in nanowire superconducting single-photon detectors*, Appl. Phys. Lett. **105**, 222602 (2014).

[193] L. J. Van der Pauw, A method of measuring specific resistivity and Hall Effect of a disc of arbitrary shape, Philips Technical Review. **20**, 220 (1958).

[194] Q. Meng, X. Sun, Y. Sun, B. Sun, and F. Li, *Mapping Technique for Measurement of Sheet Resistance Distribution*, Chinese Journal of Semiconductors **18**, 701 (1997).

[195] M. Suzuki, N. Kobayashi, K. Mukai, and S. Kondo, Characterization of Silane-Reduced Tungsten Films Grown by CVD as a Function of Si Content, J. Electrochem. Soc. **137**, 3213 (1990).

[196] J.W. Gibson and R.A. Hein, *Superconductivity of tungsten*, Phys. Rev. Lett. **12**, 688 (1964).

[197] T. Cecil, A. Miceli, O. Quaranta, C. Liu, D. Rosenmann, S. McHugh, and B. Mazin, *Tungsten silicide films for microwave kinetic inductance detectors,* Appl. Phys. Lett. **101**, 032601 (2012).

[198] M. Osofsky, R. Soulen, J. Claassen, G. Trotter, H. Kim, and J. Horwitz, *New insight into enhanced superconductivity in metals near the metal-insulator transition,* Phys. Rev. Lett. **87**, 197004 (2001).

[199] K. Nishimoto, *Tungsten Silicide Films for Superconducting Resonators*, http://www.nnin.org/sites/default/files/2013_reu_ra/2013nninRA_Nishimoto.pdf

[200] O. Quaranta, T. W. Cecil, and A. Miceli, *Tungsten Silicide Alloys for Microwave Kinetic Inductance Detectors*, IEEE Trans. Appl. Supercond. **23**, 2400104 (2013).

[201] Shibata, Hiroyuki, Tatsushi Akazaki, and Yasuhiro Tokura, Appl. Phys. Express 6, 023101 (2013).

[202] Y. Korneeva, M. Sidorova, A. Semenov, S. Krasnosvobodtsev, K. Mitsen, A. Korneev, G. Chulkova, and G. Goltsman, *Comparison of Hot Spot Formation in NbN and MoN Thin Superconducting Films After Photon Absorption*, IEEE Trans. Appl. Supercond. **26**, 2200404 (2016).

[203] C. Mack, Fundamental Principles of Optical Lithography: The Science of Microfabrication, John Wiley & Sons, New Jersey, United States of America, 2007.

[204] D. Mailly, *Nanofabrication Techniques*, Eur. Phys. J. **172**, 333 (2009).

[205] L. G. Aslamazov and A. I. Larkin, The influence of fluctuation pairing of electrons on the conductivity of normal metal, Phys. Letters **26A**, 238 (1968).

[206] W. J. Skocpol and M. Tinkham, *Fluctuations near superconducting phase transitions*, Rep. Prog. Phys. **38**, 1049 (1975).

[207] R. S. Thompson, Microwave, Flux Flow, and Fluctuation Resistance of Dirty Type-II Superconductors, Phys. Rev. B **1**, 327 (1970).

[208] A. Semenov, B. Günther, U. Böttger, H.-W. Hübers, H. Bartolf, A. Engel, A. Schilling, K. Ilin, M. Siegel, R. Schneider, D. Gerthsen, and N. A. Gippius, *Optical and transport properties of ultrathin NbN films and nanostructures*, Phys. Rev. B **80**, 054510 (2009).

[209] E. Helfand and N. R. Werthamer, Temperature and Purity Dependence of the Superconducting Critical Field, H_{c2}. II, Phys. Rev. **147**, 288 (1966).

[210] W. Buckel and R. Kleiner, *Supraleitung - Grundlagen und Anwendungen*. WileyVCH, Weinheim, 6th ed., 2004

[211] J. M. Gordon, and A. M. Goldman, Electron inelastic scattering in aluminum films and wires at temperatures near the superconducting transition, Phys. Rev. B **34**, 1500 (1986).

[212] H. Bartolf, A. Engel, A. Schilling, K. Il'in, M. Siegel, H.-W. Hübers, and A. Semenov, *Current-assisted thermally activated flux liberation in ultrathin nanopatterned NbN superconducting meander structures*, Phys. Rev. B **81**, 024502 (2010).

[213] A. Einstein, On the theory of the Brownian movement, *Ann. d. Phys.* **19**, 371 (1906).

[214] M. Smoluchowski, Zur kinetischen Theorie der Brownschen Molekularbewegung und der Suspensionen, *Ann. d. Phys.* **21**, 756 (1906).

[215] W. Meissner and R. Ochsenfeld, *Ein neuer Effekt bei Eintritt der Supraleitfähigkeit*, Naturwissenschaften **21**, 787 (1933).

[216] F. London and H. London, The electromagnetic equations of the supraconductor, *Proc. Roy. Soc. (London)* **A149**, 71, (1935).

[217] M. Tinkham, *Introduction to superconductivity*. McGraw-Hill, New York NY, 2nd ed., (1996).

[218] J. Bardeen, L. N. Cooper, and J. R. Schrieffer, Theory of superconductivity, *Phys. Rev.* **108**, 1175 (1957).

[219] F. Marsili, F. Najafi, E. Dauler, F. Bellei, X. Hu, M. Csete, R. J. Molnar, and K. K. Berggren, Single-photon detectors based on ultranarrow superconducting nanowires, *Nano Letters* 11, 2048 (2011).

[220] H. Bartolf, Fabrication and characterization of superconducting nanowire highspeed single-photon detectors. PhD thesis, University of Zürich, (2009).

[221] K. Inderbitzin, Superconducting Nanowires for Soft X-Ray Single-Photon Detection. PhD thesis, University of Zürich, (2013).

[222] A. Engel, J. J. Renema, K. Il'in, and A. Semenov, *Detection mechanism of superconducting nanowire single-photon detectors*, Supercond. Sci. Technol. **28**, 114003 (2015).

[223] J. J. Renema, R. Gaudio, Q. Wang, Z. Zhou, A. Gaggero, F. Mattioli, R. Leoni, D. Sahin, M. J. A. de Dood, A. Fiore, and M. P. van Exter, *Experimental Test of Theories of the Detection Mechanism in a Nanowire Superconducting Single Photon Detector*, Phys. Rev. Lett. **112**, 117604 (2014).

[224] L. N. Bulaevskii, Matthias J. Graf, and V. G. Kogan, Vortex-assisted photon counts and their magnetic field dependence in single-photon superconducting detectors, Phys. Rev. B **85**, 014505 (2012).

[225] A. Engel, H. Bartolf, A. Schilling, A. Semenov, H.-W. Hübers, K. Il'in and M. Siegel, *Magnetic vortices in superconducting photon detectors*, J. Mod. Opt. **56**, 352 (2009).

[226] A. Engel and A. Schilling, Numerical analysis of detection-mechanism models of superconducting nanowire single-photon detector, J. Appl. Phys. **114**, 214501 (2013).

[227] L. N. Bulaevskii, M. J. Graf, C. D. Batista, and V. G. Kogan, *Vortex-induced dissipation in narrow current-biased thin-film superconducting strips*, Phys. Rev. B **83**, 144526 (2011).

[228] D. Yu. Vodolazov, Yu. P. Korneeva, A. V. Semenov, A. A. Korneev, and G. N. Goltsman, Vortex-assisted mechanism of photon counting in a superconducting nanowire single-photon detector revealed by external magnetic field, Phys. Rev. B **92**, 104503 (2015)

[229] A. N. Zotova and D. Y. Vodolazov, Photon detection by current-carrying superconducting film: A time-dependent Ginzburg-Landau approach, Phys. Rev. B **85**, 024509 (2015)

[230] A. D. Semenov, R. S. Nebosis, Yu. P. Gousev, M. A. Heusinger, and K. F. Renk, Phys. Rev. B 52, 581 (1995).

[231] A. D. Semenov, R. S. Nebosis, Yu. P. Gousev, M. A. Heusinger, and K. F. Renk, Analysis of the nonequilibrium photoresponse of superconducting films to pulsed radiation by use of a two-temperature model, Phys. Rev. B **52**, 581 (1995)

[232] S. D. Brorson, A. Kazeroonian, J. S. Moodera, D. W. Face, T. K. Cheng, E. P. Ippen, M. S. Dresselhaus, and G. Dresselhaus, *Femtosecond room-temperature measurement of the electron-phonon coupling constant* γ *in metallic superconductors*, Phys. Rev. Lett. **64**, 2172 (1990).

[233] V. G. Kogan, Pearl's vortex near the film edge, Phys. Rev. B **49**, 15874 (1994); **75**, 069902(E) (2007).

[234] J. Pearl, Current distribution in superconducting films carrying quantized fluxoids, Appl. Phys. Lett. **5**, 65 (1964).

[235] E. Abrahams, P. W. Anderson, D. C. Licciardello, and T. V. Ramakrishnan, *Scaling Theory of Localization: Absence of Quantum Diffusion in Two Dimensions*, Phys. Rev. Lett. **42**, 673 (1979).

[236] G. Bergmann, Weak localization in thin films: a time-of-flight experiment with conduction electrons, Phys. Rep. **107**, 1 (1984).

[237] P.W. Anderson, E. Abrahams and T.V. Ramakrishnan, *Possible Explanation of Nonlinear Conductivity in Thin-Film Metal Wires*, Phys. Rev. Lett. 43, 718 (1979).

[238] F. J. Wegner, The mobility edge problem: Continuous symmetry and a conjecture, Z. Physik **35**, 207 (1979).

[239] D. Vollhardt and P. Wölfle, Anderson Localization in d <~ 2 Dimensions: A Self-Consistent Diagrammatic Theory, Phys. Rev. Lett. **45**, 842 (1980).

[240] P. F. Maldague, Quantum diffusion and divergent fluctuations in disordered metals, Phys. Rev. B **23**, 1719 (1981).

[241] D. J. Thouless, *Maximum Metallic Resistance in Thin Wires*, Phys. Rev. Lett. **39**, 1167 (1977).

[242] M. Ya. Azbel, *Localization in Thin Wires*, Phys. Rev. Lett. **46**, 675 (1981).

[243] A. Levchenko, Magnetoconductivity of low-dimensional disordered conductors at the onset of the superconducting transition, Phys. Rev. B **79**, 212511 (2009).

[244] S. Hikami, A. I. Larkin, and Y. Nagaoka, Spin-Orbit Interaction and Magnetoresistance in the Two Dimensional Random System, Prog. Theor. Phys. **63**, 707 (1980).

[245] B. L. Altshuler and A. G. Aronov, *Electron-Electron Interaction in Disordered Systems*, edited by A. J. Efros and M. Pollak (Elsevier, Amsterdam, 1985), pp. 1–153.

[246] W. J. Hardy, H. Ji, H. Paik, D. G. Schlom, and D. Natelson, *Mesoscopic quantum effects in a bad metal, hydrogen-doped vanadium dioxide*, J. Phys.: Condens. Matter **29**, 185601 (2017).

[247] L. H. Tzarfati, R. Hevroni, A. Aharony, O. E. Wohlman, M. Karpovski, V. Shelukhin, V. Umansky, and A. Palevski, *Dephasing Measurements in InGaAs/AlInAs Heterostructures: Manifestations of Spin-Orbit and Zeeman Interactions*, J. Mod. Phys. **8**, 110 (2017).

[248] N. Hemsworth, V. Tayari, F. Telesio, S. Xiang, S. Roddaro, M. Caporali, A. Ienco, M. Serrano-Ruiz, M. Peruzzini, G. Gervais, T. Szkopek, and S. Heun, *Dephasing in strongly anisotropic black phosphorus*, Phys. Rev. B **94**, 245404 (2016).

[249] L. Fruchter, O. Schneegans, and Z. Z. Li, *Anisotropy and interaction effects of strongly strained SrIrO3 thin films*, J. Appl. Phys. **120**, 075307 (2016).

[250] P. Ngabonziza, M. P. Stehno, H. Myoren, V. A. Neumann, G. Koster, A. Brinkman, *Gate-Tunable Transport Properties of In Situ Capped Bi_2Te_3 Topological Insulator Thin Films*, Adv. Electron. Mater. **2**, 1600157 (2016).

[251] Amit K. Das, P. Misra, R. S. Ajimsha, M. P. Joshi, and L. M. Kukreja, Effects of electron interference on temperature dependent transport properties of two dimensional electron gas at MgZnO/ZnO interfaces, Appl. Phys. Lett. **107**, 102104 (2015).

[252] S. Bansal, S.C. Kashyap, D.K. Pandya, Metal-semiconductor transition and negative magneto-resistance in degenerate ultrathin tin oxide films, J. Alloy. Compd. **646**, 483 (2015).

[253] Vincent E. Sacksteder, IV, Kristin Bjorg Arnardottir, Stefan Kettemann, and Ivan A. Shelykh, *Topological effects on the magnetoconductivity in topological insulators*, Phys. Rev. B **90**, 235148 (2014).

[254] G. Herranz, G. Singh, N. Bergeal, A. Jouan, J. Lesueur, J. Gazquez, M. Varela, M. Scigaj, N. Dix, F. Sanchez, and J. Fontcuberta, *Engineering two-dimensional superconductivity and Rashba spin–orbit coupling in* $LaAlO_3/SrTiO_3$ *quantum wells by selective orbital occupancy*, Nat. Commun. **6**, 6028 (2015).

[255] U. Chandni, Erik A. Henriksen, and J. P. Eisenstein, Transport in indium-decorated graphene, Phys. Rev. B **91**, 245402 (2015).

[256] H. Ochoa, F. Finocchiaro, F. Guinea, and V. I. Fal'ko, Spin-valley relaxation and quantum transport regimes in two-dimensional transition-metal dichalcogenides, Phys. Rev. B **90**, 235429 (2014).

[257] Y. Shiomi, T. Ohtani, , S. Iguchi, T. Sasaki, Z. Qiu, H. Nakayama, K. Uchida, and E. Saito, *Interface-dependent magnetotransport properties for thin Pt films on ferrimagnetic* $Y_3Fe_5O_{12}$, Appl. Phys. Lett. **104**, 242406 (2014).

[258] D. Stornaiuolo, S. Gariglio, A. Fête, M. Gabay, D. Li, D. Massarotti, and J.-M. Triscone, *Weak localization and spin-orbit interaction in side-gate field effect devices at the* $LaAlO_3/SrTiO_3$ *interface*, Phys. Rev. B **90**, 235426 (2014).

[259] Y. Kim, R. M. Lutchyn, and C. Nayak, Origin and transport signatures of spin-orbit interactions in one- and two-dimensional $SrTiO_3$ -based heterostructures, Phys. Rev. B **87**, 245121 (2013).

[260] J. Lee, J. Park, J. H. Lee, J. S. Kim, and H. J. Lee, Gate-tuned differentiation of surface-conducting states in $Bi_{1.5}Sb_{0.5}Te_{1.7}Se_{1.3}$ topological-insulator thin crystals, Phys. Rev. B **86**, 245321 (2012).

[261] H. Fujiki, M. Yamada, B. Shinozaki, T. Kawaguti, F. Ichikawa, T. Fukami, and T. Aomine, Superconducting fluctuation, localization and electron–electron interaction corrections to the magnetoconductivity in three-dimensional aluminum films, Physica C: Superconductivity vol. 311, p. 58, (1999)

[262] A. I. Larkin and A. Varlamov, *Theory of fluctuations in superconductors* (Clarendon Press, Oxford, 2005).

[263] L. G. Aslamazov and A. I. Larkin, Vliyanie fluktuatsii na svoistva sverkhprovodnika pri temperaturakh vyshe kriticheskoi, Fizika tverd. tela, **10(4)**, 1104 (1968); [L.G. Aslamazov, A.I. Larkin, Effect of Fluctuations on the Properties of a Superconductor Above the Critical Temperature, Sov. Phys. Solid State, **10(4)**, 875 (1968)].

[264] K. Maki, The Critical Fluctuation of the Order Parameter in Type-II Superconductors, Prog. Theor. Phys. **39**, 897 (1968).

[265] A. I. Larkin, *Magnetosoprotivlenie dvumernykh sistem*, Pis’ma Zh. Eksp. Teor. Fiz. **31**, 239 (1980); [A. I. Larkin, *Reluctance of two-dimensional systems*, JETP Lett. **31**, 219 (1980)].

[266] B. L. Al’shtuler, A. G. Aronov, A. I. Larkin, and D. E. Khmel’nitskii, *Ob anomal’nom magnitosoprotivlenii v poluprovodnikakh*, Zh. Eksp. Teor. Fiz. **81**, 768 (1981); [B. L. Al’tshuler, A. G. Aronov, A. I. Larkin, and D. E. Khmel’nitskii, *Anomalous magnetoresistance in semiconductors*, Sov. Phys. JETP **54**, 411 (1981).]

[267] S. M. Girvin, M. Jonson, and P. A. Lee, Interaction effects in disordered Landau-level systems in two dimensions, Phys. Rev. B **26**, 1651(1982).

[268] G. Bergmann, Physical interpretation of weak localization: A time-of-flight experiment with conduction electrons, Phys. Rev. B **28**, 2914 (1983).

[269] G. Bergmann, Weak anti-localization—An experimental proof for the destructive interference of rotated spin 12, Solid State Commun. **42**, 815 (1982).

[270] G. Bergmann, Inelastic Life-Time of the Conduction Electrons in Some Noble Metal Films, Z. Phys. B: Condens. Matter **48**, 5 (1982).

[271] S. Sangiao, N. Marcano, J. Fan, L. Morellon, M. R. Ibarra, and J. M. de Teresa, *Quantitative analysis of the weak anti-localization effect in ultrathin bismuth films*, Europhys. Lett. **95**, 37002 (2011).

[272] S. Maekawa and H. Fukuyama, Magnetoresistance in Two-Dimensional Disordered Systems: Effects of Zeeman Splitting and Spin-Orbit Scattering, J. Phys. Soc. Jpn. **50**, 2561 (1981).

[273] R. Rosenbaum, Superconducting fluctuations and magnetoconductance measurements of thin films in parallel magnetic fields, Phys. Rev. B **32**, 2190 (1985).

[274] M. Franz, Superconductivity: Importance of fluctuations, Nature **3**, 686 (2007).

[275] A. Perali, P. Pieri, G. C. Strinati, and C. Castellani, *Pseudogap and spectral function from superconducting fluctuations to the bosonic limit*, Phys. Rev. B **66**, 024510 (2002).

[276] A. Glatz, A. A. Varlamov, and V. M. Vinokur, *Fluctuation spectroscopy of disordered two-dimensional superconductors*, Phys. Rev. B **84**, 104510 (2011).

[277] J. M. B. Lopes dos Santos and E. Abrahams, Superconducting fluctuation conductivity in a magnetic field in two dimensions, Phys. Rev. B **31**, 172 (1985).

[278] W. Brenig, M. A. Paalanen, A. F. Hebard, and Wölfle, *Magnetoconductance of thin-film superconductors near critical disorder*, Phys. Rev. B **33**, 1691 (1986).

[279] M. Yu. Reizer, Fluctuation conductivity above the superconducting transition: Regularization of the Maki-Thompson term, Phys. Rev. B **45**, 12949 (1992).

[280] K. Meiners-Hagen, and W. Gey, Maki-Thompson correction to magnetoresistance in three-dimensional disordered alloys, Phys. Rev. B **63**, 052507 (2001).

[281] M. H. Redi, Two-dimensional fluctuation-induced conductivity above the critical temperatures, Phys. Rev. B **16**, 2027 (1977).

[282] E. Abrahams, R. E. Prange, and M. J. Stephen, *Effect of a magnetic field on fluctuations above* T_c, Physica **55**, 230 (1971).

[283] K. D. Usadel, The influence of a static magnetic field on the fluctuation superconductivity, Z. Phys. **227**, 260 (1969).

[284] T. I. Baturina, S. V. Postolova, A. Yu. Mironov, A. Glatz, M. R. Baklanov, and V. M. Vinokur, Superconducting phase transitions in ultrathin TiN films, Europhys. Lett. **97**, 17012 (2012).

[285] A. Glatz, A. A. Varlamov, and V. M. Vinokur, *Quantum fluctuations and dynamic clustering of fluctuating Cooper pairs*, Europhys. Lett. **94**, 47005 (2011).

[286] A. Glatz, A. A. Varlamov, and V. M. Vinokur, *Fluctuation spectroscopy of disordered two-dimensional superconductors*, Phys. Rev. B **84**, 104510 (2011).

[287] M. Giannouri, E. Rocofyllou, C. Papastaikoudis, and W. Schilling, Weak-localization, Aslamazov-Larkin, and Maki-Thompson superconducting fluctuation effects in disordered $Zr_{1-x}Rh_x$ films above T_c, Phys. Rev. B **56**, 6148 (1997).

[288] W. L. McMillan, Transition Temperature of Strong-Coupled Superconductors, Phys. Rev. 167, 627 (1968).

[289] B. L. Al’tshuler, A. G. Aronov, and D. E. Khmelnitsky, Effects of electron-electron collisions with small energy transfers on quantum localisation, J. Phys. C **15**, 7367 (1982).

[290] B. I. Belevtsev, Yu. F. Komnik, and E. Yu. Beliayev, *Electron relaxation in disordered gold films*, Phys. Rev. B **58**, 8079 (1998).

[291] W. Brenig, M. C. Chang, E. Abrahams, and P. Wölfle, Inelastic scattering time above the superconductivity transition in two dimensions: Dependence on disorder and magnetic field, Phys. Rev. B **31**, 7001 (1985).

[292] M. Sidorova, A. Semenov, A. Korneev, G. Chulkova, Yu. Korneeva, M. Mikhailov, A. Devizenko, A. Kozorezov, and G. Goltsman, Electron-phonon relaxation time in ultrathin tungsten silicon film, arXiv:1607.07321.

[293] A. D. Semenov, M. A. Heusinger, K. F. Renk, E. Menschikov, A.V. Sergeev, A. I. Elantev, I. G. Goghidze, and G. N. Gol'tsman, *Influence of phonon trapping on the performance of NbN kinetic inductance detectors*, IEEE Trans. Appl. Supercond. **7**, 3083 (1997).

[294] F. Marsili, M. J. Stevens, A. Kozorezov, V. B. Verma, Colin Lambert, J. A. Stern, R. D. Horansky, S. Dyer, S. Duff, D. P. Pappas, A. E. Lita, M. D. Shaw, R. P. Mirin, and S. W. Nam, *Hotspot relaxation dynamics in a current-carrying superconductor*, Phys. Rev. B **93**, 094518 (2016).

[295] A. G. Kozorezov, C. Lambert, F. Marsili, M. J. Stevens, V. B. Verma, J. A. Stern, R. Horansky, S. Dyer, S. Duff, D. P. Pappas, A. Lita, M. D. Shaw, R. P. Mirin, and S. W. Nam, *Quasiparticle recombination in hotspots in superconducting current-carrying nanowires*, Phys. Rev. B **92**, 064504 (2015).

[296] C. M. Natarajan, M. G. Tanner, and R. H. Hadfield, *Superconducting nanowire single-photon detectors: physics and applications*, Supercond. Sci. Technol. **25**, 063001 (2012).

[297] J. J. Renema, R. Gaudio, Q. Wang, A. Gaggero, F. Mattioli, R. Leoni, M. P. van Exter, A. Fiore, and M. J. A. de Dood, *Probing the hotspot interaction length in NbN nanowire superconducting single photon detectors*, Appl. Phys. Lett. **110**, 233103 (2017).

[298] A. E. Grigorescu, M. C. van der Krogt, C. W. Hagen, and P. Kruit, *10 nm Lines and Spaces Written in HSQ, Using Electron Beam Lithography*, Microelectron. Eng. **84**, 822 (2007).

[299] Michael Hotz, Röntgenfluoreszenz zur Monochromatisierung für die Untersuchung von supraleitendenden Nanodraht Einzelphotonendetektoren, Master thesis, Universität Zürich, 2015.

[300] W. Skocpol, M. Beasley, and M. Thinkham, *Self-heating hotspots in superconducting thin-film microbridges*， J. Appl. Phys. **45**, 4054 (1974).

[301] T. Yamashita, S. Miki, W. Qiu, M. Fujiwara, M. Sasaki, and Z. Wang, Temperature Dependent Performances of Superconducting Nanowire Single-Photon Detectors in an Ultralow-Temperature Region, Appl. Phys. Express **3**, 102502 (2010).

[302] R. H. Hadfield, A. J. Miller, S. W. Nam, R. L. Kautz, and R. E. Schwall, *Low-frequency phase locking in high-inductance superconducting nanowires*, Appl. Phys. Lett. **87**, 203505 (2005).

[303] J. K. W. Yang, A. J. Kerman, E. A. Dauler, V. Anant, K. M. Rosfjord, and K. K. Berggren, *Modeling the Electrical and Thermal Response of Superconducting Nanowire Single-Photon Detectors*, IEEE Trans. Appl. Supercond. **17**, 581 (2007).

[304] A. J. Annunziata, O. Quaranta, A. Casaburi, L. Frunzio, M. Ejrnaes, M. J. Rooks, R. Cristiano, S. Pagano, A. Frydman, and D. E. Prober, *Reset dynamics and latching in niobium superconducting nanowire single-photon detectors*, J. Appl. Phys. **108**, 084507 (2010).

[305] A. M. Goldman & N. Markovic, *Superconductor-insulator transitions in the twodimensional limit*, Phys. Today **51**, 39 (1998).

[306] A. M. Goldman, *Superconductor–insulator transitions*. Int. J. Mod. Phys. B **24**, 4081 (2010).

[307] S. L. Sondhi, S. M. Girvin, J. P. Carini, and D. Shahar, *Continuous quantum phase transitions*, Rev. Mod. Phys. **69**, 315 (1997).

[308] A. T. Bollinger, G. Dubuis, J. Yoon, D. Pavuna, J. Misewich, and I. Božović, *Superconductor-insulator transition in* $La_{2-x}Sr_xCuO_4$ *at the pair quantum resistance,* Nature **472**, 458 (2011).

[309] M. P. A. Fisher, G. Grinstein, and S. M. Girvin, *Presence of quantum diffusion in two dimensions: Universal resistance at the superconductor-insulator transition*, Phys. Rev. Lett. **64**, 587 (1990).

[310] M. P. A. Fisher, *Quantum phase transitions in disordered two-dimensional superconductors*, Phys. Rev. Lett. **65**, 923 (1990).

[311] A. F. Hebard and M. A. Paalanen, *Magnetic-field-tuned superconductor-insulator transition in two-dimensional films*, Phys. Rev. Lett. **65**, 927-930 (1990).

[312] A. Yazdani, and A. Kapitulnik, *Superconducting-insulating transition in two dimensional a-MoGe thin films*, Phys. Rev. Lett. **74**, 3037–3040 (1995).

[313] A. M. Finkel’shtein, *Superconducting transition temperature in amorphous films*, JETP Lett. **45**, 46 (1987).

[314] J. M. Valles, Jr., R. C. Dynes, and J. P. Garno, *Electron tunneling determination of the order-parameter amplitude at the superconductor-insulator transition in 2D*, Phys. Rev. Lett. **69**, 3567 (1992).

[315] A. M. Finkel’stein, *Suppression of superconductivity in homogeneously disordered systems*, Physica B **197**, 636 – 648 (1994).

[316] S. Y. Hsu, J. A. Chervenak, and J. M. Valles, Jr., *Magnetic field enhanced order parameter amplitude fluctuations in ultrathin films near the superconductor-insulator transition*, Phys. Rev. Lett. **75**, 132 (1995).

[317] K. A. Parendo, K. H. Sarwa B. Tan, A. Bhattacharya, M. Eblen-Zayas, N. E. Staley, and A. M. Goldman, et al. *Electrostatic tuning of the superconductor-insulator transition in two dimensions*, Phys. Rev. Lett. **94**, 197004 (2005).

[318] P. Szabó, T. Samuely, V. Hašková, J. Kačmarčík, M. Žemlička, M. Grajcar, J. G. Rodrigo, and P. Samuely, *Fermionic scenario for the destruction of superconductivity in ultrathin MoC films evidenced by STM measurements*, Phys. Rev. B **93**, 014505 (2016).

[319] D. B. Haviland, Y. Liu, and A. M. Goldman, *Onset of superconductivity in the two-dimensional limit*, Phys. Rev. Lett. **62**, 2180 (1989).

[320] M. Ovadia, D. Kalok, B. Sacépé, and D. Shahar, *Duality symmetry and its breakdown in the vicinity of the superconductor-insulator transition*, Nature Physics **9**, 415 (2013).

[321] X. G. Wen and A. Zee, *Universal conductance at the superconductor-insulator transition*, Int. J. Mod. Phys. B **4**, 437 (1990).

[322] N. Mason and A. Kapitulnik, *Dissipation effects on the superconductor-insulator transition in 2D superconductors*, Phys. Rev. Lett. **82**, 5341 (1999).

[323] E. Bielejec and W. Wu, *Field-tuned superconductor-insulator transition with and without current bias*, Phys. Rev. Lett. **88**, 206802 (2002).

[324] X. Shi, P. V. Lin, T. Sasagawa, V. Dobrosavljević and D. Popović, *Two-stage magnetic-field-tuned superconductor–insulator transition in underdoped* $La_{2-x}Sr_xCuO_4$. Nat. Phys. **10**, 437 (2014).

[325] N. Markovic, C. Christiansen, and A. M. Goldman, *Thickness–magnetic field phase diagram at the superconductor-insulator transition in 2D*, Phys. Rev. Lett. **81**, 5217 (1998).

[326] H. Aubin, C. A. Marrache-Kikuchi, A. Pourret, K. Behnia, L. Bergé, L. Dumoulin, and J. Lesueur, *Magnetic-field-induced quantum superconductor-insulator transition in* $Nb_{0.15}Si_{0.85}$, Phys. Rev. B **73**, 094521 (2006).

[327] A. D. Caviglia, S. Gariglio, N. Reyren, D. Jaccard, T. Schneider, M. Gabay, S. Thiel, G. Hammerl, J. Mannhart, and J.-M. Triscone, Electric field control of the LaAlO3/SrTiO3 interface ground state, Nature **456**, 624-627 (2008).

[328] J. Biscaras, N. Bergeal, S. Hurand, C. Feuillet-Palma, A. Rastogi, R. C. Budhani, M. Grilli, S. Caprara, and J. Lesueur, *Multiple quantum criticality in a two-dimensional superconductor*, Nature materials **12**, 542 (2013).

[329] Y. Xing, H.-M. Zhang, H.-L. Fu, H. Liu, Y. Sun, J.-P. Peng, F. Wang, X. Lin, X.-C. Ma, Q.-K. Xue, J. Wang, and X. C. Xie, *Quantum Griffiths singularity of superconductor-metal transition in Ga thin films*, Science **350**, 542 (2015).

[330] C. Christiansen, L. M. Hernandez, and A. M. Goldman, *Evidence of collective charge behavior in the insulating state of ultrathin films of superconducting metals*, Phys. Rev. Lett. **88**, 037004 (2002).

[331] P. W. Phillips and D. Dalidovich, *The elusive Bose metal*, Science **302**, 243 (2003).

[332] P. W. Phillips, *Two-dimensional materials: not just a phase*, Nature Physics **12**, 206 (2016).

[333] M. A. Steiner, N. P. Breznay, and A. Kapitulnik, *Approach to a superconductor-to-Bose-insulator transition in disordered films*, Phys. Rev. B **77**, 212501 (2008).

[334] A. Allain, Z. Han, and V. Bouchiat, *Electrical control of the superconducting-to-insulating transition in graphene-metal hybrids*, Nature Mater. **11**, 590 (2012).

[335] Y. Dubi, Y. Meir and Y. Avishai, *Nature of the superconductor-insulator transition in disordered superconductors*, Nature **449**, 876 (2007).

[336] N. Marković, C. Christiansen, A. M. Mack, W. H. Huber, and A. M. Goldman, *Superconductor-insulator transition in two dimensions*. Phys. Rev. B **60**, 4320-4328 (1999).

Talks and Posters

- **Superconducting and normal state properties of a-WSi films**

  Zhang Xiaofu, Julia Lonsky, Andreas Engel, Andreas Schilling

  Swiss Physical Society - SPS Annual Meeting 2014,

  Fribourg, 30.6 - 2.7.2014

- **X-ray sensititve and energy-dispersive superconducting nanowire single-photon detectors**

  Xiaofu Zhang, Kevin Inderbitzin, Andreas Engel, Andreas Schilling

  Low Temperature Detectors 16 Conference

  Grenoble, 20.7 - 24.7.2015

- **X-ray sensititve and energy-dispersive superconducting nanowire single-photon detectors**

  Xiaofu Zhang, Kevin Inderbitzin, Andreas Engel, Andreas Schilling

  12th European Conference on Applied Superconductivity

  Lyon, 06.09 - 10.09.2015

- **Hotspot Dynamics of Superconducting Nanowire Single Photon Detectors**

  X. Zhang, A. Engel, Q. Wang, A. Schilling, A. Semenov, M. Sidorova, H.-W. Hübers, I. Charaev, K. Ilin, M. Siegel

  ASC 2016

  Denver, 04.09 - 09.09.2016

- **Hotspot Dynamics of Superconducting Nanowire Single Photon Detectors**

  X. Zhang, A. Engel, Q. Wang, A. Schilling, A. Semenov, M. Sidorova, H.-W. Hübers, I. Charaev, K. Ilin, M. Siegel

  Workshop on Nanowire Superconducting Single Photon Detectors

  Leiden, 28.11 - 01.12.2016

- **Superconducting nanowire single X-ray photon detector based on WSi**

Xiaofu Zhang, Qiang Wang, Andreas Schilling

Workshop on Nanowire Superconducting Single Photon Detectors

Leiden, 28.11 - 01.12.2016

Publication List

- **Detection mechanism in SNSPD: Numerical results of a conceptually simple, yet powerful detection model**

A. Engel, J. Lonsky, X. Zhang, and A. Schilling

IEEE Transactions on Applied Superconductivity **25**, 2200407 (2015)

- **Characteristics of superconducting tungsten silicide W_xSi_{1-x} for single photon detection**

X. Zhang, A. Engel, Q. Wang, A. Schilling, A. Semenov, M. Sidorova, H.-W. Hübers, I. Charaev, K. Ilin, M. Siegel

Phys Rev. B **94**, 174509 (2016)

- **Superconducting single X-ray photon detector based on $W_{0.8}Si_{0.2}$**

X. Zhang, Q. Wang, A. Schilling

AIP Advances **6** (11), 115104 (2016)

- **Sequential superconductor-Bose insulator-Fermi insulator quantum phase transitions in two-dimensional *a*-WSi**

Xiaofu Zhang and Andreas Schilling

To be submitted.

- **Superconducting fluctuation and characteristic time scale in amorphous WSi**

Xiaofu Zhang, Adriana E. Lita, Mariia Sidorova, Varun. B. Verma, Qiang Wang, Sae Woo Nam, Alexei Semenov, and Andreas Schilling

In Phys Rev. B, “under review”; **arXiv:1712.05019**

Curriculum Vitae

Personal Dates

Name:	Xiaofu Zhang
Date of birth:	15.06.1988
Birthplace:	Sichuan, China
Address:	Stettbacherrain 12, 8051 Zürich

Education

1993 – 2000	GuangHui Primary School
2000 – 2002	GuangHui Middle School
2002 – 2003	Nr. 52 Middle School in Urumqi (Huimin Middle School)
2003 – 2006	Nr. 8 High School in Urumqi
2006 – 2010	Beijing University of Chemical Technology
2010 – 2013	University of Chinese Academy of Science
2013 – 2017	Universität Zürich

Acknowledgements

First of all, I would like to gratefully thank to Prof. Dr. Andreas Schilling, for the opportunity to perform such a fascinating doctoral work in condensed matter physics. I would like to further thank him for maintaining an exciting research environment, for providing an active and very important mentorship, for important career advice, for sharing his research philosophy, and for countless communication advice. It was my great honor to participate in these amazing research topics.

Secondly, I would like to thank my supervisor Dr. Andreas Engel for his patience about my experiment and the research topic. Many thanks for the supervision of the understanding about the hotspot dynamics.

Many thanks to Prof. Dr. Christof Aegerter for his supervision and his suggestions as a member of my PhD committee.

I would like to thank Prof. Dr. Alexei Semenov from the DLR in Berlin-Adlershof for the measurements of the recovery of superconductivity. Thanks a lot for your patience and suggestions during my experiment. Many thanks to Prof. Dr. Heinz-Wilhelm Hübers and Mariia Sidorova for the discussing of the data analysis.

I thank Dr. Ilya Charaev for the low impedance microbridge preparation. Many thanks to Prof. Dr. Konstantin Ilin and Prof. Dr. Michael Siegel for their suggestions on my experiment and my paper.

Many thanks to Dr. Wang for sharing with me his research experience and the modifications to my papers. We had a lot of hot discussions about the detectors fabrication and understandings about the mechanisms of SNSPDs.

Special thanks to the precious researchers Dr. Holger Bartolf and Dr. Kevin Inderbitzin for your pioneering research about the nano fabrication technology in our group. My device fabrication techniques are based on your results.

I would like to thank to all my colleagues in our group, Dr. Olaf Bossen, Dr. Fabian von Rohr, Dr. Henrik Grundmann, Daniel Destraz, Alsu Gazizulina, Shangxiong Huangfu and Stefan Siegrist. You have paid a lot attentions in the maintenance about the equipment. Many thanks to the team of the mechanics workshop as well. Thanks for your attentions about my complicated designs and preparing the mechanics stuff for my research. I would also like to thank the supporting from the people from FIRST lab. Thanks for your help during the preparation of my detectors.

Thanks to Ruth Halter, Monika Röllin, Carmelina Genovese and Brigitte Freund for your administration associated with the traveling to conferences and experiments.

Finally, I would also like to thank my family, especially my wife Wang Haijiao. Thanks so much for supporting my work.